Active Control of Femtosatellite Swarms for Synthetic Aperture Radar

Jianlin Cao

A thesis submitted in fulfilment of the requirements for the degree of
Doctor of Philosophy

Submitted to
Department of Mechanical and Aerospace Engineering
University of Strathclyde

February 2020

This thesis is the result of the author's original research. It has been composed by the author and has not been previously submitted for examination which has led to the award of a degree.

Signed:

Date:

To my loving family and friends.
致我最亲爱的家人和朋友们。

Acknowledgements

Throughout the time of my PhD research, I have been fortunate enough to received an enormous amount of help and support. First, I would like to thank my supervisors, Prof. Colin McInnes and Prof. John Soraghan, who provided me with the chance to start this incredible journey of innovative research. Your guidance and expertise have played a key role in the completion of my research. It has been a privilege to be your student. Furthermore, I would like to express my gratitude to Dr. Carmine Clemente for his help and insight during my research and the preparation of this thesis. Your enthusiasm to push the boundaries of research has always been inspiring. Moreover, I would like to thank my colleagues and friends Callum, Jiaying, Christos, Domenico, Adriano, Alessio, Ilias, William, Pasquale, Jonathan, Yuhong and Tze Cherng for all their support and collaboration throughout these years. This research would not have been possible without the sponsorship of the University of Strathclyde, Glasgow, Scotland. Glasgow is a city of rich culture and I enjoyed the constantly changing weather. A special thanks to Ellen McGeough from Glasgow Royal Infirmary for providing the care and help during the harsh time of tuberculosis. Again, I want to thank my parents for their support and encouragement. I will never stop being grateful.

Abstract

Recent developments in electronics and technology have pushed miniaturised satellites to the femto-scale, which feature a low mass between 10 to 100 g. Although femtosatellites have been proven as a feasible concept, most designs are limited by sensor capacity and mission lifetime due to the lack of environmental protection and onboard propellent. In this thesis, a novel concept of using femtosatellites for Earth remote sensing missions has been proposed.

In particular, a novel femtosatellite concept based on the utilisation of solar radiation pressure is introduced together with an Earth remote sensing mission concept. The prototype femtosatellite design features a high area-to-mass ratio to maximise solar radiation pressure for orbit control. A flexible base material enables self-release when loaded with pre-applied tension to reduce the complexity of the carrier spacecraft release mechanism. Its flat-bubble design also provides basic thermal and radiation protection. In addition to an antenna for communication to the carrier spacecraft, the prototype design includes a separate antennae for radar applications, the design of which will vary depending on the mission requirement. A hardware design is also provided for such a femtosatellite concept and performance is evaluated for an Earth remote sensing mission. The mission concept utilises swarms of femtosatellites as receivers for enhanced radar mission. A 'dawn-dusk' Sun-synchronous orbit has been chosen to maximise solar radiation pressure for orbit control and power generation.

The orbital dynamics of the proposed femtosatellite concept is investigated and a novel

active orbit control strategy for relative motion control with solar radiation pressure is developed. This control strategy demonstrates the feasibility of using solar radiation pressure for swarm control, which can be modulated by using electrochromic panels, to achieve the active orbit control of individual femtosatellites. This will extend the femtosatellite swarm mission capability and lifetime. The femtosatellite swarm deployment evolution is also provided to demonstrate the active orbit control strategy.

The performance of the femtosatellite swarm Earth remote sensing mission is evaluated and characterised by the number of femtosatellites, the receiver signal-to-noise ratio and the accuracy of positioning. These research results demonstrate the feasibility of using swarms of femtosatellites for Earth remote sensing. In addition, by adapting the radar signal processing algorithm, on-orbit targets could be detected. This is demonstrated by imaging the international space station and mock space debris for space situational awareness applications.

Contents

List of Figures

List of Tables

Nomenclature

Acronyms

2-D	2 dimensional
AD	Atmospheric drag
ADCS	Attitude determination and control system
AIS	Automatic identification system
ASI	Italian space agency
au	Astronomical unit
C&DH	Command and data handling
CM	Centre of mass
CMG	Control moment gyroscope
COTS	Commercial off-the-shelf
DEM	Digital elevation measurement
DLR	German aerospace centre
EADS	European aeronautic defence and space company
EDT	Electrodynamic tether
FFT	Fast Fourier transform

HET Hall-effect thruster

IFFT Inverse fast Fourier transform

IMU Inertial measurement unit

ISAR Inverse synthetic aperture radar

ISS International space station

JAXA Japan aerospace exploration agency

JPL Jet propulsion laboratory

LEO Low Earth orbit

MCU Microcontroller

MEMS Micro-electro-mechanical system

MIMO Multi-input-multi-output

MISO Multi-input-single-output

NASA National aeronautics and space administration

NESZ Noise equivalent sigma zero

PCB Printed circuit board

RCD Reflectivity control devices

RCMC Range cell migration correction

RDA Range-Doppler algorithm

RF Radio frequency

SAR Synthetic aperture radar

SIMO Single-input-multi-output

SRP Solar radiation pressure

SSO Sun-synchronous orbit

VLBI Very long baseline interferometry

VLM Vaporizing liquid micro-thruster

Greek Symbols

α Spacecraft attitude angle

α_s Spacecraft surface solar absorptivity

β Bi-static angle

ε Thickness coefficient

ε_s Spacecraft infrared emissivity

η Sail efficiency

Δ_η Sail efficiency coefficient difference

Γ Spacecraft mean speed

λ Torque coefficient (Chapter 5)

λ Wavelength (Chapter 6)

μ_{Earth} Gravitational parameter of the Earth

ω_n Mean motion

Ω Ascending node angle

$\Delta\Omega$ Angular precession per orbit

ψ Incident angle

ρ Mean desity of the spacecraft (Chapter 4)

ρ Atmospheric density (Chapter 5)

ρ_r Resolution in the range direction

σ Stefan-Boltzmann constant

τ Slow time (Chapter 3)

τ Torque (Chapter 5)

τ Transmitting pulse width (Chapter 6)

τ_c Centre of slow time

Roman Symbols

A Spacecraft projected area

a Orbit semi-major axis

a_0 Solar sail characteristic acceleration

A_{AD} Projected area of the spacecraft for the atmospheric drag

$A_{carr,xy}$ Projected area of the carrier spacecraft in the x, y-plane

$A_{carr,xz}$ Projected area of the carrier spacecraft in the x, z-plane

A_e Surface area for absorption of the radiation from Earth

A_{LCD} Total area of electrochromic panels

A_r Surface area for heat radiation

A_s Surface area for absorption of the solar energy

A_{SRP} Cross-section area of the spacecraft for the solar radiation pressure

a_x External acceleration along the x-axis

a_y External acceleration along the y-axis

a_z	External acceleration along the z-axis
B_0	Bandwidth
c	speed of light
C_D	Drag coefficient
C_L	Lift coefficient
c_p	Heat capacity
e	Orbit eccentricity
f_0	Carrier frequency
F_{Drag}	Drag force
F_k	Attenuation factor
F_{Lift}	Lift force
ΔF_{SRP}	Differential torque
G_e	Thermal energy radiated by the Earth
G_r	Receiver antenna gain
G_r	Reflected solar flux from Earth surface
G_s	Direct solar flux
G_t	Transmitter antenna gain
I	Moment of inertia
i	Orbit inclination
J_2	Coefficient of the Earth oblateness
k	Scatterers' identifier (Chapter 2)

k	Torque coefficient (Chapter 5)
K_r	Range chirp pulse frequency
L	Charactristic length-scale (Chapter 4)
L	Lenth of spacecraft (Chapter 5)
L_{tot}	System loss
m	Mass of spacecraft
m_{carr}	Mass of the carrier spacecraft
MSE	Mean square error
n	Gaussian noise (Chapter 2)
n	Number of femtosatellite (Chapter 6)
NF	Receiver noise figure
P	Solar radition pressure
PRF	Pulse repeat frequency
P_t	Transmit power
Q_{int}	Internal heat generation rate
R	Range
r	Carrier spacecraft orbit radius
$R_{\oplus}$	Earth radius
R_{rx}	Range between the receiver and the target
R_{tx}	Range between the transmitter and the target
s_{rx}	Received signal

s_{tx}	Transmitted signal
T	Spacecraft surface temperature (Chapter 4)
T	Spacecraft orbit period (Chapter 5)
t	Fast time
T_0	Receiver temperature
T_r	Range chirp pulse duration
V_s	Radar velocity
v_{vel}	Relative velocity
Δv_y	Change in velocity
w_a	Antenna pattern
w_r	Transmit envelop
x	Coordinate along x-axis
y	Coordinate along y-axis
$a_{y,AD}$	AD acceleration along the y-axis
$a_{y,Carr}$	Carrier spacecraft acceleration along the y-axis
$a_{y,SRP}$	SRP acceleration along the y-axis
$a_{y,Total}$	Total acceleration along the y-axis
z	Coordinate along z-axis
$a_{z,AD}$	AD acceleration along the z-axis
$a_{z,Carr}$	Carrier spacecraft acceleration along the z-axis
$a_{z,SRP}$	SRP acceleration along the z-axis
$a_{z,Total}$	Total acceleration along the z-axis

Publications

Some aspects of the work reposted in this thesis have been presented and published.

Journal papers

Cao, J., Clemente, C., McInnes, C. R., and Soraghan, J. J. (2020). "Synthetic Aperture Radar Using Solar Radiation Pressure Enabled Femtosatellites". In: *IEEE Transactions on Aerospace and Electronic Systems*. Accepted for publication.

Persico, A. R., Clemente, C., Gaglione, D., Ilioudis, C. V., Cao, J., Pallotta, L., Maio, A. D., Proudler, I., and Soraghan, J. J. (2017). "On Model, Algorithms, and Experiment for Micro-Doppler-Based Recognition of Ballistic Targets". In: *IEEE Transactions on Aerospace and Electronic Systems* 53.3, pp. 1088–1108.

Conference papers

Cao, J., Clemente, C., Mcinnes, C., Soraghan, J., and Uttamchandani, D. (2015). "A Novel Concept for Earth Remote Sensing Using A Bi-static Femto-satellite Swarm in Sun Synchronous Orbit". In: *66th International Astronautical Congress, Jerusalem, Israel*.

Ilioudis, C., Cao, J., Theodorou, I., Striano, P., Coventry, W., Clemente, C., and Soraghan, J. (2019). “GNSS based passive radar for UAV monitoring”. In: *IEEE Radar Conference 2019*.

MacLeod, C., Cao, J., Pierce, S., Sullivan, J., Pipe, A., Dobie, G., and Summan, R. (2014). “Remotely deployable aerial inspection using tactile sensors”. In: *40TH Annual Review of Progress in Quantitative Nondestructive Evaluation*.

Persico, A., Clemente, C., Ilioudis, C., Gaglione, D., Cao, J., and Soraghan, J. (2015). “Micro-Doppler based recognition of ballistic targets using 2D gabor filters”. English. In: *2015 Sensor Signal Processing for Defence (SSPD)*.

Poster

Cao, J., Clemente, C., Mcinnes, C., Soraghan, J., and Uttamchandani, D. (2016). “Enabling Space Based Radar with Femtosatellites”. In: *SET for BRITAIN, London, UK*.

Chapter 1

Introduction

1.1 Preface

The development of technology in electronics, especially in miniaturisation, has enabled satellites to be reduced in both mass and volume while maintaining or improving their performance and mission capability. For example, the most popular small satellite platform is the CubeSat, described as 'the possible future platforms for scientific missions' (Sandau, 2010). Selva et al. have published a survey on the capabilities of CubeSat platforms for Earth observation applications, covering the technological capabilities and limitations of CubeSats as well as Earth science mission requirements (Selva et al., 2012). Villela et al. have published a statistical overview of CubeSat missions and predict that one thousand CubeSat will be launched by 2021 (Villela et al., 2019).

Another key benefit of small satellites is that multiple platforms can fly in formation or in a constellation to enrich their capability. Bandyopadhyay et al. notes that of 39 impending small satellite formation-flying missions, Earth science-related missions are the most popular, while

most multi-satellite missions are using constellations with more than 4 satellites (Bandyopadhyay et al., 2015).

One of the challenges of formation-flying is the requirement for continuous corrections to the orbital elements of the satellites. This increase in system complexity will increase the demands on small satellites. The FIRST (Formation-flying sub-Ionospheric Radio astronomy Science and Technology) Explorer mission has been proposed to demonstrate passive formation-flying with science applications (Bergman et al., 2009). This system includes 1 mother spacecraft and 6 daughter spacecraft. The mother spacecraft is responsible for transport of the daughter spacecraft to the desired orbit, collecting data from the daughter spacecraft and transmitting pre-processed data to Earth. On the daughter spacecraft, 2 variable area sails could be used for attitude control by taking the advantage of solar radiation pressure. The daughter spacecraft will passively self-stabilise and orientate itself towards the Sun. The use of solar radiation pressure for orbit control will be discussed later in this thesis.

Moreover, the TechSat 21 mission was proposed to demonstrate the possibility of a 'virtual satellite', which included 3 microsatellites in formation (Martin and Kilberg, 2001). This 'virtual satellite' creates a large sparse aperture system using X-band transmitter and receivers as payloads. Unfortunately, this project was cancelled due to cost overruns. A similar study was conducted by Engelen et al. for Nano-SAR (Engelen et al., 2012), a case study of synthetic aperture radar (SAR) for nanosatellites. This concept provides detailed specifications of the radar system and requirements to allow in-orbit demonstration of the system. Persico et al. further explore the feasibility of passive bi-static radar for space situational awareness on CubeSat platforms (Persico et al., 2019). Other example missions that are feasible for small satellites includes automatic identification systems (AIS) for ships (Wahl et al., 2005), radar calibration

(Martin, Fisher, et al., 2011) and disasters monitoring (Becena et al., 2012). Radar applications for swarms of femtosatellites will be investigated later in this thesis.

To further reduce small satellite mass and volume, Barnhart et al. have proposed a 'satellite-on-a-chip' design (Barnhart, Vladimirova, and Sweeting, 2005), a concept first noted by Joshi (Joshi, 1994). Their work covers mission analysis, payload and spacecraft configuration and subsystem design. They outline a realistic 'satellite-on-a-chip' design: "200 mm maximum diameter, less than 5 mm thick, less than 100 g mass, and l00 mW peak power". This design fits into the category of femtosatellite and becomes a guideline of further research. In addition to the design, they also noted that "a successful demonstration of this technology will open the door for distributed mission concepts". In recent years, several femtosatellite designs have been proposed: PCBSat (Barnhart, Vladimirova, and Sweeting, 2007b), WikiSat (Tristancho et al., 2011), Sprite (Manchester et al., 2013), RyeFemSat (Stuurman et al., 2010), Monarch (Adams et al., 2019) and a recent PCB-satellite concept (Hu et al., 2019). Those designs feature different architecture, payloads and missions, as will be discussed in Chapter 2.

1.2 Motivation

One of the key aims of the thesis is to investigate new design concepts for femtosatellite. The main goal for this new design is to increase mission capabilities while reducing size and mass by investigating the subsystems and existing femtosatellite designs. Also, this research is aimed at enabling a novel active orbit control strategy for femtosatellite swarms and then characterising the performance of such a swarm based on Earth remote sensing missions.

The objectives of the research presented in this thesis are: the development of a novel solar radiation pressure enabled femtosatellite concept for Earth remote sensing; the development of an Earth remote sensing mission to demonstrate the capability of femtosatellite swarms; the analysis of femtosatellite orbital dynamics in relative motion with external forces; the development of a control strategy for femtosatellites to achieve orbit control; the performance analysis of the femtosatellite swarm for Earth remote sensing using SAR. This thesis will therefore address the developments required to create a feasible femtosatellite swarm for a novel Earth remote sensing mission.

1.3 Original Contributions

The research conducted in this thesis has led to a number of original contributions in the fields of femtosatellite design, femtosatellite orbital dynamics, femtosatellite orbit control and femtosatellite swarm missions. The contributions are as follows:

A novel femtosatellite design based on the utilisation of solar radiation pressure is proposed. Compared to existing femtosatellite designs, this prototype design features a high area-to-mass ratio to maximise solar radiation pressure for orbit control. Also, a flexible base material is used to reduce mass and enables self-release when loaded with pre-applied tension to reduce the complexity of the carrier spacecraft release mechanism. The flat-bubble design provides basic thermal and radiation protection. In addition to an antenna for communication to the carrier spacecraft, the prototype design includes separate antennas for radar applications. Preliminary design specifications are provided.

A novel orbital dynamic analysis for the femtosatellite concept is investigated. In conjunction with the proposed design, the force model is exploited in order to analyse the suitable orbit altitude for Earth remote sensing missions. The suitability of Earth remote sensing missions is demonstrated through simulation analysis. Furthermore, a novel orbit control strategy for relative motion with external forces is demonstrated based on the femtosatellite orbital dynamics. Compared to previous concepts without an orbit control strategy, this control strategy demonstrates the feasibility of using solar radiation pressure, which can be modulated by using electrochromic panels, to achieve active attitude and orbit control on the femtosatellite. This will extend the femtosatellite swarm mission capability and lifetime. The results demonstrated that with a suitable orbit altitude and active orbit control strategy, femtosatellites are able to adapt to different initial release speeds and initial perturbations. A swarm of femtosatellites can be deployed in a controlled manner.

A novel femtosatellite swarm SAR mission concept based on the prototype and active orbit control strategy is presented. The mission concept utilises femtosatellites as receivers for radar. The performance of the femtosatellite swarm mission is analysed and characterised by investigating ground targets. Based on the characterisation, the quality of the generated radar image from a femtosatellite swarm could be estimated for different mission configurations. The research results demonstrate the feasibility of using swarms of femtosatellites for Earth remote sensing. In addition, the performance is also evaluated by focusing the SAR signal on in-orbit targets for space situational awareness purpose. These will further expand the mission capability of the femtosatellite swarm.

1.4 Thesis Organization

The remainder of the thesis is divided into 6 chapters organised as follows: Chapter 2 introduces the key concepts to be used, including the basic femtosatellite design, solar radiation pressure and relative motion. It begins with an introduction to standard spacecraft subsystems. Two femtosatellites, WikiSat and Sprite, are then compared as the foundation for the novel design which will be introduced in Chapter 4. Solar radiation pressure and relative motion are investigated to provide the theoretical basis for Chapter 5.

Chapter 3 introduces the concept of SAR as the example Earth remote sensing mission which is used in Chapter 6 to characterise the performance of femtosatellite swarms. The bistatic SAR concept is also introduced to enrich the mission capability. Then, a SAR signal model, radar system configuration and the range-Doppler algorithm for signal processing used in this thesis are provided. Spaceborne missions, TerraSAR-X, TanDEM-X, COSMO-SkyMed and Capella constellation, are considered to demonstrate the feasibility of the Earth remote sensing missions used in this thesis.

This thesis exploits the potential capability of a femtosatellite platform with limited mass, therefore, Chapter 4 is the first novel chapter which proposes a femtosatellite design to maximise the capability of the femtosatellite for the radar mission. The femtosatellite design will be developed and the radar mission concept will also be investigated to take advantage of such a design. The hardware design of the femtosatellite will be evaluated, based on the literature review in Chapter 2. This will provide the foundation for further investigation of the femtosatellite orbital dynamics and control.

Chapter 5 investigates the orbital dynamics and control of the femtosatellite concept proposed in Chapter 4. The force model, attitude control and translation control are discussed in detail to exploit the orbit manoeuvrability of the femtosatellite swarm. An active orbit control strategy is then provided to demonstrate the capability of femtosatellite orbit control with an example mission where a femtosatellite will be ejected at different speeds from a carrier spacecraft. Finally, the evolution of a swarm of femtosatellites released from the carrier spacecraft is provided. A swarm with active orbit control will be used to form a linear antenna array for radar applications.

Chapter 6 evaluates the performance of the proposed femtosatellite swarm for the Earth remote sensing SAR application. A modified SAR signal processing algorithm based on a range-Doppler algorithm will be provided to process the simulated SAR signal. The performance of such femtosatellite swarms are analysed and evaluated in different scenarios: the number of femtosatellites, received signal-to-noise ratio and positioning error. Other on-orbit targets will also be evaluated to demonstrate the capability of using a femtosatellite swarm for space situational awareness applications.

Chapter 7 concludes the thesis with a discussion of its limitations and future work.

Chapter 2

Femtosatellite Systems

2.1 Introduction

In this chapter, a review of the femtosatellite concept is provided. A brief review of femtosatellites is provided in Section 2.2. Key aspects of femtosatellite design are reviewed based on subsystems in Section 2.3. Existing femtosatellites are discussed with a focus on their hardware design and mission capabilities in Section 2.4. The physical background of solar radiation pressure control is presented in Section 2.5, followed by the simplified model used in this thesis. The technical details of relative motion is provided in Section 2.6, with the coordinate system used for analysis. The simplified linear equations of relative motion used are presented in analytical form. Finally, Sun-synchronous orbits used in this thesis are then explored in Section 2.7, to take full advantage of the prototype femtosatellite which will be discussed in Chapter 4.

2.2 Femtosatellite Development

Miniaturisation is a popular trend in almost every area which involves electronics. Many key parameters can benefit from it: efficiency, power consumption etc. Another benefit, for satellites, is the reduction of launch cost. For example, the standard cost of launching a payload into Low Earth Orbit (LEO) with 28.5° inclination using the Falcon 9 vehicle is approximately $ 2719 per kg (SpaceX, 2018). In terms of the satellite, satellites with a wet mass (including fuel) below 500 kg are considered "small satellites". Table 2.1 shows the standard satellite classification by wet mass.

TABLE 2.1: Satellite classification by wet mass (Janson, 2003)

Class	Mass
Large satellite	> 1000 kg
Medium satellite	500 - 1000 kg
Minisatellite	100 - 500 kg
Microsatellite	10 - 100 kg
Nanosatellite	1 - 10 kg
Picosatellite	0.1 - 1 kg
Femtosatellite	10 - 100 g

Femtosatellites are defined with a mass between 10 g and 100 g. Generally, all satellites with a mass less than 100 g are currently classified as femtosatellites. Therefore, the earliest and smallest femtosatellites are the needles in the West Ford Experiment, May 1963 (Morrow et al., 1964; Shapiro et al., 1964). In the experiment, a cloud of needles was used as an artificial

reflection layer for 8 GHz radio signals. In total, 480 million copper needles, as shown in Figure 2.1, which were 17.8 mm long and 0.0178 mm diameter, were launched and dispersed. After two months, the needles spread to a 30 km thick and 15 km wide cloud at 3,700 km altitude. There was then no further development of the femtosatellite concept due to the limitations of technology until recent years.

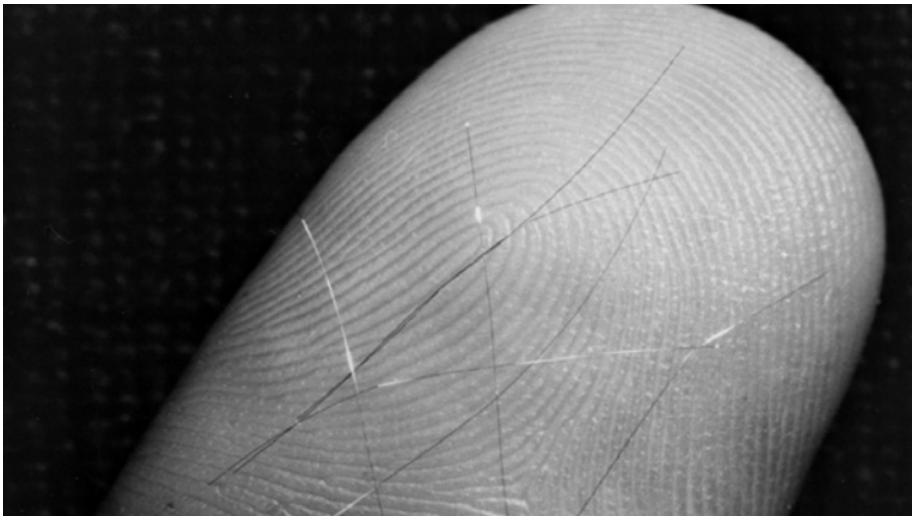

FIGURE 2.1: Needles from the West Ford Experiment (Morrow et al., 1964)

2.3 Femtosatellite Subsystems

In order to develop the concept of femtosatellites, more detailed design requirements need to be conducted. According to Larson et al., spacecraft can be divided into the following subsystems (Larson et al., 1999):

2.3.1 Command & Data Handling

The command and data handling (C&DH) subsystem is essential to the spacecraft. It processes commands and data for the spacecraft and the payload. The C&DH connects all active subsystems: collecting, processing and distributing information to or from those subsystems. For femtosatellites, C&DH, communications and the payload can be combined to maximise the integration of the design.

2.3.2 Communication

The communication subsystem provides a data link to the ground station or other spacecraft. This system is responsible for spacecraft status telemetry to monitor the condition of the spacecraft. Depending on their mission, the communication system may also receive commands and transmit data generated by the payload. Due to size and power limitations, the femtosatellites considered in this thesis will communicate with the carrier spacecraft instead of a ground station.

2.3.3 Attitude Determination & Control System

The attitude determination and control system (ADCS) is the subsystem that measures and controls the spacecraft's orientation. Similar to the propulsion subsystem, it is not required for the simplest free-floating femtosatellites. Another approach to maintain the spacecraft orientation is by using a specially designed geometry to enable passive ADCS (Martinelli et al., 2005). This is particularly attractive for femtosatellites.

In addition to using propulsion as an ADCS actuator, there are two more actuator solutions available for femtosatellites. Magnetorquers are electromagnetic coils that create a magnetic field to interact with the environmental ambient magnetic field. Magnetorquers do not require propellant and include no moving parts, and are therefore lightweight and reliable. Jove-Casulleras et al. and Hu et al. developed femtosatellite prototypes that feature magnetorquers as ADCS actuators (Jove-Casulleras et al., 2011; Hu et al., 2019). Reaction wheels are also widely used ADCS actuators for small satellites and can provides finer attitude control than magnetorquers. Reaction wheels can also be used for power storage (Peczalski et al., 2001). These have two major configurations: momentum wheels and control moment gyroscopes (CMG). Post et al. proposed a MicroElectroMechanical System (MEMS) CMG design for femtosatellite attitude control (Post et al., 2016).

2.3.4 Power

The power subsystem manages the generation, storage and distribution of electrical power. The most common source of power is solar energy using solar cells. The power generated can be stored in a battery, super capacitor or reaction wheels (Peczalski et al., 2001). For femtosatellites, three solutions have been proposed: 1) Solar cell and battery: this is proposed by Barnhart et al. for the PCBSat, and it is ideal for complex payloads and long lifetime missions (Barnhart, Vladimirova, and Sweeting, 2007b). 2) Battery only: this is proposed by Jove-Casulleras et al. for the WikiSat (Jove-Casulleras et al., 2011). The battery provides greater mission short-term capability. However, the lifetime is limited due to the lack of external power generation. 3) Solar cells and super capacitor: this is proposed by Manchester et al. for the Sprite femtosatellite (Manchester et al., 2013). The femtosatellites have a limited power supply during eclipses,

resulting in a limited capability. However, the disadvantage of a limited power supply can be circumvented by the novel mission concept which will introduced in Chapter 4.

2.3.5 Propulsion

The propulsion subsystem produces thrust to change the orbital elements of a satellite. It is not required for all spacecraft, however, it is key to enhancing the capability of a spacecraft. For conventional spacecraft, of order half of the mass can be used for propulsion depending on the orbit and mission. Conventional hot gas propulsion is not suitable for the femtosatellites due to mass and volume limitations. Therefore, miniaturised propulsion subsystems are required to enhance mission capability. Possible propulsion solutions which can be miniaturised for femtosatellites are listed below.

The vaporizing liquid micro-thruster (VLM) has been developed by the NASA Jet Propulsion Laboratory (JPL) as an attitude control thruster for micro-spacecraft (Mueller et al., 2003). It would be sufficient to be used for orbit control for smaller spacecraft, such as femtosatellites. The VLM is a resistojet concept built using MEMS technology that provides thrust by heating a fluid. Typically, the thruster vaporizes a non-reactive liquid such as water, to generate thrust. One of the benefits of using liquid propellant is to decrease the weight and size of the propellant tank compared to an equivalent gas storage system. The use of water as propellant is also safer for testing. An assembled thruster produced by NASA JPL is shown in Figure 2.2.

The VLM feeds liquid propellants with pressure via heater strips, which are then vaporized and expanded through a micro-nozzle to produce thrust. In order to minimise the size and limit power consumption, the VLM is T-shaped to provide thermal insulation, as shown in Figure 2.3. This includes 2 thin-film deposited gold heaters. These are spaced apart by a spacer-chip

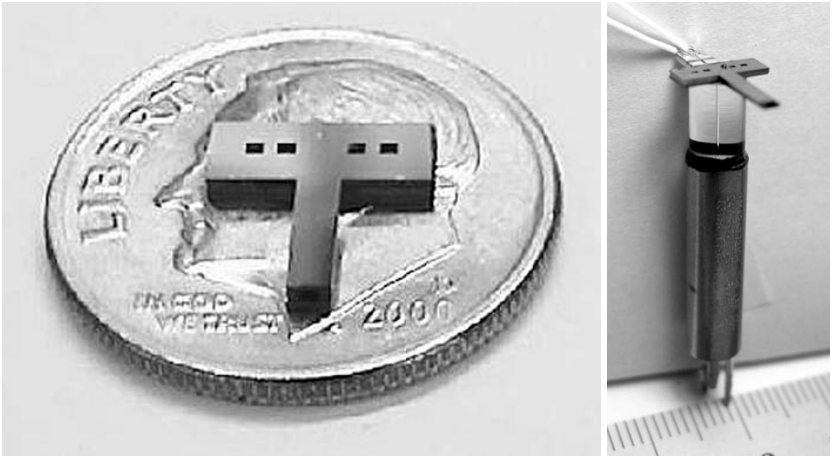

FIGURE 2.2: VLM thruster (Mueller et al., 2003)

and joined via a gold thermal compression bond. The specific impulse was measured to be of order 100 s.

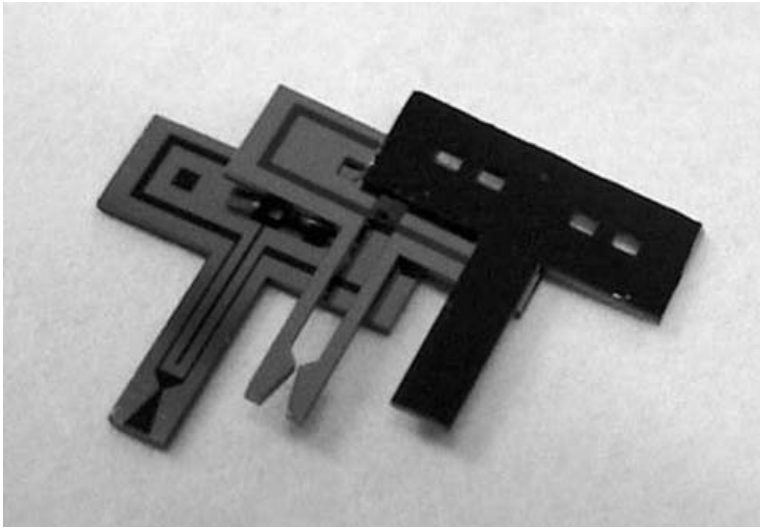

FIGURE 2.3: Triple chip assembly (Mueller et al., 2003)

The Hall-effect thruster (HET) is one type of electric propulsion. During operation, propellants are ionized and accelerated by an electric field to produce thrust. The HET features a high specific impulse between 1500 and 3000 s. Snyder et al. has investigated a novel HET than

can be powered by a solar array directly to increase the power over similar HET by an order-of-magnitude (Snyder et al., 2014). This technology has potential to be used as femtosatellite thrusters.

The electrodynamic tether (EDT) is one type of propellantless propulsion solution. It features a long conducting wire to convert between kinetic energy and electrical energy based on electromagnetic principles. An illustration of the EDT operating is shown in Figure 2.4.

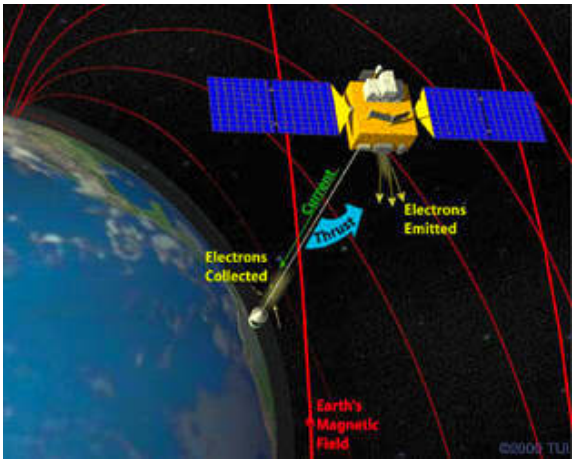

FIGURE 2.4: Principle of EDT (Bell et al., 2011)

Atchison et al. investigated the feasibility of using EDT on a millimetre-scale, fully integrated spacecraft-on-chip (Atchison et al., 2007). By exploiting the Earth's magnetic field, it can achieve a daily perturbation of 18 m from a Keplerian circular orbit at 350 km. Bell et al. proposed a novel approach for femtosatellites which utilises 2 tethered femtosatellites (Bell et al., 2011; Bell, 2014). The EDT is then able to generate sufficient thrust to overcome atmospheric drag in LEO. In addition, McTernan et al. demonstrated that EDT can also be configured for current collection to generate power (McTernan et al., 2012).

Solar sailing is a form of spacecraft propulsion using solar radiation pressure (SRP), generating acceleration from the momentum of solar photons. Solar sailing is also a propellantless

propulsion solution. Solar sailing requires a high area-to-mass ratio to take advantage of SRP. Compared to EDT, SRP can be used to generate thrust for both orbit control and attitude control. This is one of the promising solutions for femtosatellites. Further details will be discussed in Section 2.5.

Both EDT and SRP require no on-board propellant. Thus, their specific impulses are in principle infinite. Table 2.2 shows the comparison between the propulsion solutions discussed. It is clear that SRP is the most versatile and promising solution for femtosatellites since it is lightweight, and again, can be used for both orbit control and attitude control.

TABLE 2.2: Comparison of propulsion solutions for femtosatellites

	Specific Impulse (s)	Feasibility	Potential for attitude control
VLM	approximately 100	Mid	Mid
HET	1500 - 3000	Low	Low
EDT	∞	High	Low
SRP	∞	High	High

2.3.6 Thermal Control

The thermal subsystem protects the spacecraft and its other subsystems from extreme temperatures. The main external sources of heat for the spacecraft in the vacuum environment are radiation from the Sun and the Earth. Extreme temperatures will physically damage silicon devices and other components such as batteries. The thermal subsystem is crucial to femtosatellite space environment survivability. Devices on femtosatellites are generally exposed to the space environment since a structure is usually not considered, other than a single printed

circuit board. This will reduce the radiation tolerance of the femtosatellite. Compared to conventional spacecraft, the femtosatellite mission lifetime is much shorter. Therefore, radiation protection is not compulsory. Based on the mission requirements, metal spot shielding could be used to protect the core components.

2.4 Current Femtosatellites

In order to investigate the potential of the femtosatellite concept, standard spacecraft subsystems have been simplified and integrated. Many femtosatellite concepts, which aim for cost-effective applications, have emerged recently. The common theme is that they use a minimal design to accomplish mission objectives. Early designs include: PCBSat (Barnhart, Vladimirova, Sweeting, et al., 2007), SpaceChip (Barnhart, Vladimirova, and Sweeting, 2007a), RyeFemSat (Stuurman et al., 2010) and Monarch (Adams et al., 2019). Nicolai et al. reviews the latest devices, where WikiSat and Sprite are two of the most feasible femtosatellite prototypes (Niccolai et al., 2019).

2.4.1 WikiSat

WikiSat is a femtosatellite with a sub-20 g mass and dimensions of 141×30 mm (Fernandez-Murcia et al., 2011; Tristancho et al., 2011; Jove-Casulleras et al., 2011), developed to download images from low Earth orbit (LEO). Prototypes have been designed to be launched into a 250 km orbit with a lifetime of less than one month due to its large area-to-mass ratio.

The fourth version of WikiSat, shown in Figure 2.5, is built on a two-layer printed circuit board (PCB) with an ATmega168 AVR microcontroller running open source Arduino firmware.

FIGURE 2.5: WikiSat prototype (Fernandez-Murcia et al., 2011)

An InvenSense ITG-3200 3-axis gyroscope and an STMicroelectronics LIS331HH 3-axis accelerometer are used for the inertial measurement unit (IMU) to measure the device orientation and two pairs of magnetorquers maintain an Earth facing attitude. The onboard payload is a TCM8230MD camera to capture images at 640 $\times$ 480 pixel resolution. The images are downloaded to a ground station via a NRF24L01 2.4GHz low power transceiver and a synthetic aperture antenna made from 4 AT9520 multilayer chip antennas, which point the beam to the Earth electronically. WikiSat uses a coin battery to provide power instead of solar cells to maximise performance during its short orbit lifetime.

2.4.2 Sprite

The Sprite satellite, shown in Figure 2.6, is a simple proof of concept femtosatellite (Manchester et al., 2013), which is 35$\times$35 mm in size with a mass of 5 g, developed by Cornell University and crowdfunded via Kickstarter. The concept is to create a 'personal spacecraft', that could be owned and operated on a low budget. Sprites were launched into orbit above 300

km inside a 3U CubeSat called 'KickSat' on 18th April 2014. Unfortunately, the Sprites failed to deploy due to a clock reset and were lost during re-entry on 15th May 2014. On 18th March 2019, over 100 of Sprite femtosatellites successfully deployed from the 'KickSat-2' spacecraft (Coldewey, 2019).

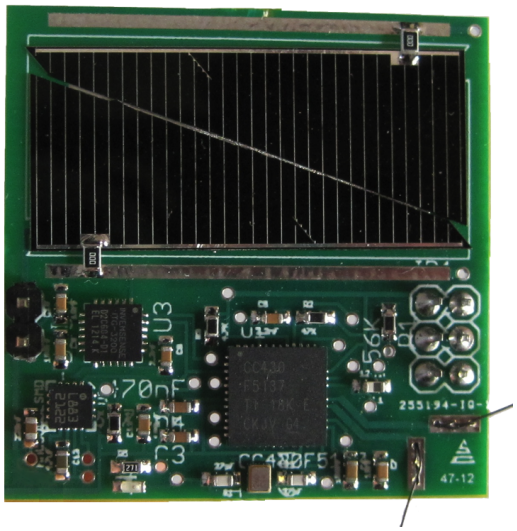

FIGURE 2.6: Sprite (Manchester et al., 2013)

Sprite is designed as a free floating satellite without attitude control. A Texas Instruments CC430F5137 microcontroller running Energia firmware is used as the onboard computer. The IMU includes an InvenSense ITG-3200 3-axis gyroscope and a Honeywell HMC5883L 3-axis compass. Sprite is designed to send a beacon signal to ground via a CC1101 radio at 437.240 MHz, which is integrated into the microcontroller. Two solar panels provide power for the microcontroller and communications. A comparison between WikiSat and Sprite is shown in Table 2.3.

WikiSat and Sprite are two examples of current femtosatellite concepts. They share a similar PCB design with integrated sub-systems. However, both designs have limited payload

TABLE 2.3: Comparison between WikiSat and Sprite

	WikiSat	Sprite
Size	141 × 30 mm	35 × 35 mm
Weight	7.6 g (without battery)	5 g
MCU	ATmega168	CC430F5137
Radio chip	NRF24L01	CC1101
Radio frequency	2.4 GHz	437.240 MHz
Attitude determination	Gyroscope Accelerometer	Gyroscope Compass
Attitude control	Magnetorquers	N/A
Power	Coin battery	Solar cell Super capacitor
Payload	Camera	N/A

capacity for applications when compared to CubeSats. A new design is proposed in Chapter 4 to improve the capabilities of the femtosatellite concept.

2.5 Solar Sailing

As discussed in Section 2.3, solar sailing is a promising technology for femtosatellites. It can be used for both propulsion and attitude control with no on-board propellant. The source of the acceleration for solar sailing is SRP, which is the momentum carried by photons from the Sun.

2.5.1 Solar Radiation Pressure Model

The magnitude of SRP is $4.56 \times 10^{-6} Nm^{-2}$ at a distance of one astronomical unit (au) from the Sun. The sail acceleration can be expressed as (McInnes, 2004):

$$a_0 = 2\eta P \frac{A_{SRP}}{m} \tag{2.1}$$

where a_0 is the solar sail characteristic acceleration, η is the efficiency, P is the solar radiation pressure, A_{SRP} is the cross-section area of the spacecraft for the solar radiation pressure and m is the mass of spacecraft. The sail reflectivity has been taken into consideration by adding a factor of 2, since reflected photons transport the same momentum as incoming photons.

Equation (2.1) shows that to improve the solar sail acceleration, a large cross-section and low mass are required. In addition, when the direction of incoming photons is not parallel to the normal to the spacecraft, the total force will split into incident force and reaction force components. Weis et al. introduced an active solar sail which features MEMS actuated mirrors to change the SRP incidence angle (Weis et al., 2014).

As shown in Equation (2.1), another key parameter for the total SRP force is the surface efficiency or material reflectivity coefficient. Two extreme scenarios are the ideal condition of a mirror when all incoming photons will be reflected, and a black absorbing surface when all incoming photons will be absorbed.

In practice, the change of reflectivity can be controlled via thin-film electrochromic coatings. Such devices can change their reflectivity based on an applied electric potential, also termed 'reflectivity control devices (RCD)'. The IKAROS spacecraft has demonstrated the use of RCD for attitude control (Tsuda et al., 2011; Ha et al., 2015). During this mission, the SRP

acceleration has been estimated (Yamaguchi et al., 2014) and very long baseline interferometry (VLBI) tracking used (Takeuchi et al., 2011).

Electrochromic coatings were investigated by Lucking et al. for orbit control of 'smart dust' devices (Lücking et al., 2012). In addition to basic orbit control, the possibility of using RCD for formation-flying was demonstrated by Mingotti et al. (Mingotti et al., 2014). Also, Williams et al. proposed a solution of using a solar wing instead of RCD for formation-flying (Williams et al., 2002). It can be concluded that SRP is widely used by low mass spacecraft for attitude and orbit control.

2.6 Relative Motion

The periodic motion between two objects in orbit within a relatively short distance is termed relative motion. It shares the same period as the period of the reference orbit around the Earth. A coordinate system is introduced in Figure 2.7 to describe such relative motion. The x-axis is the orbit radial direction, the y-axis is aligned with the velocity vector of the reference spacecraft and the z-axis completes the triad. The reference spacecraft is located at the origin (0,0,0) of this local frame of reference.

When all spacecraft are assumed to be in nearly circular orbits, the simplified linear equations of relative motion with external accelerations (a_x, a_y, a_z) can then be written in the form

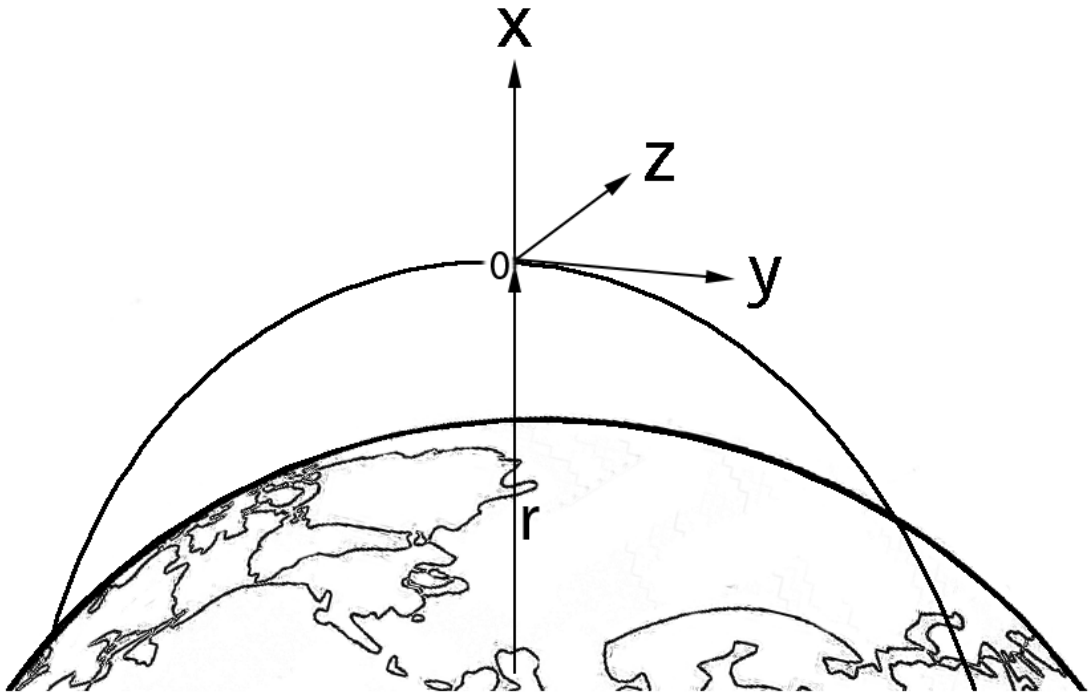

FIGURE 2.7: Coordinate system geometry for relative motion

of the Clohessy-Wiltshire or Hill's equation (Vallado, 2013):

$$\ddot{x} - 2\omega_n \dot{y} - 3\omega_n^2 x = a_x \tag{2.2a}$$

$$\ddot{y} + 2\omega_n \dot{x} = a_y \tag{2.2b}$$

$$\ddot{z} + \omega_n^2 z = a_z \tag{2.2c}$$

$$\omega_n = \sqrt{\frac{\mu_{Earth}}{r^3}} \tag{2.3}$$

where ω_n is the mean motion, μ_{Earth} is the gravitational parameter of the Earth, and r is the carrier spacecraft orbit radius.

This relative motion model will be used to describe the motion of spacecraft under constant external accelerations in Chapter 5 for the development of femtosatellite orbit control strategies.

2.7 Sun-Synchronous Orbit

The Sun-Synchronous Orbit (SSO) is one particular orbit for Earth remote sensing. SSO is enabled by the oblateness of the Earth. The oblateness will cause orbit plane precession (ascending node angle Ω), which can be expressed as (Macdonald and Badescu, 2014):

$$i = \cos^{-1}\left(-\frac{3}{2}\frac{\Delta\Omega}{J_2}\frac{a^{7/2}(1-e^2)^2}{R_\oplus^2\sqrt{\mu_{Earth}}}\right) \tag{2.4}$$

where i is the orbit inclination, $\Delta\Omega$ is the angular precession per orbit, J_2 is the coefficient of the Earth oblateness, a is the orbit semi-major axis, e is the orbit eccentricity and $R_\oplus$ is the radius of the Earth (6371 km).

When the angular precession rate matches the mean motion of the Earth about the Sun, the orbit plane can maintain a fixed angle to the Sun through the year. According to Equation (2.4), the required inclination for a SSO is approximately 98 °, with detailed results shown in Figure 2.8. Therefore, SSO is a nearly polar orbit and slightly retrograde to the Earth's rotation. Generally, the altitude of SSOs are approximately 600-800 km. Using an SSO, the spacecraft will pass the same location at the same local mean solar time. Thus, SSO is widely used for Earth remote sensing missions (Macdonald, McKay, et al., 2010). Some special SSOs which can be found are the noon/midnight SSO where the spacecraft will pass the equator at noon or midnight local mean solar time and the dawn/dusk SSO where the spacecraft will pass the equator at sunrise or sunset local mean solar time.

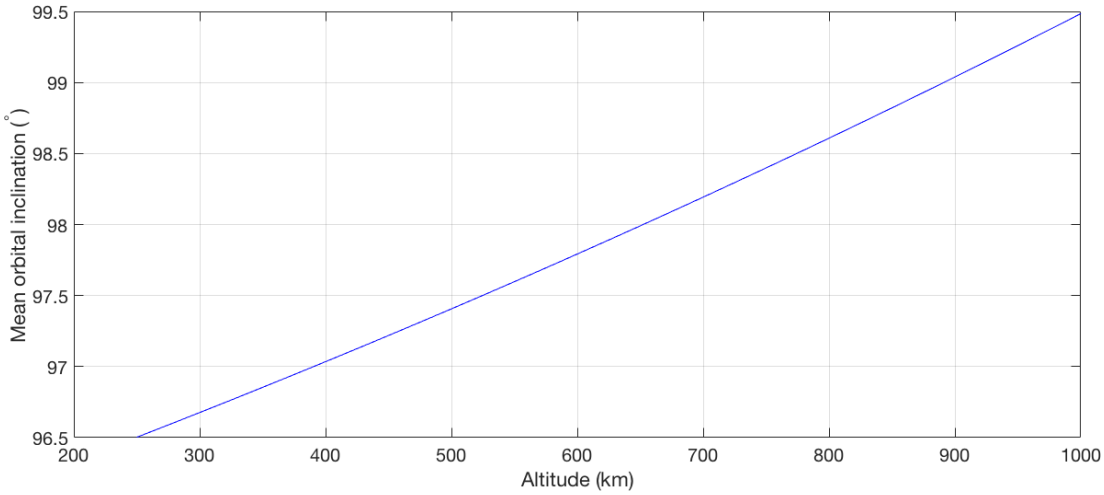

FIGURE 2.8: Required inclination for Sun-synchronous orbits

The unique feature of the dawn/dusk SSO is that the orbit plane is perpendicular to the incoming solar radiation providing a constant solar flux without eclipse. The spacecraft will be under direct illumination during the entire orbit to maximise power generation and enable SRP for orbit control. This orbit will be used for the femtosatellite swarm to be described later in Chapters 4, 5 and 6.

2.8 Summary

This chapter has presented a review of different aspects of femtosatellites and mission design. The femtosatelite concept was introduced and its related subsystems were discussed. Two promising designs, WikiSat and Sprite, were reviewed as proof of concepts where both of them feature integrated subsystems. These were discussed as the starting point for the novel femtosatellite design in Chapter 4. To solve the limitation on ADCS, power and propulsion for femtosatellites, solar sailing was introduced as a propellentless propulsion technique to extend the mission lifetime and capability of femtosatellites. The unique dawn/dusk SSO was also

considered to overcome the limitation on power generation and enable as the use of SRP for orbit and attitude control. The combination of solar sailing and the dawn/dusk SSO will be further investigated in Chapter 5 for an active orbit control strategy for relative motion.

Chapter 3

Synthetic Aperture Radar Principles for Femtosatellite Swarms

3.1 Introduction

In this chapter, the application of synthetic aperture radar (SAR) to femtosatellite swarms is discussed. The concept of synthetic aperture radar is introduced in Section 3.2. SAR signal processing is discussed in Section 3.3, with the signal model and radar system configuration introduced in Section 3.3.1 and 3.3.2. The SAR signal processing algorithm used in this thesis is provided in Section 3.3.3. Finally, a widely used spaceborne Earth remote sensing method is concluded from two current missions in Section 3.4.

3.2 Synthetic Aperture Radar

Synthetic aperture radar is a radar system that generates radar images (Cumming et al., 2005). Compared to optical sensors, SAR can provide more robust performance regardless of weather and light conditions. SAR includes its own signal source, so it operates night and day, unlike optical sensors which depend on scattered sunlight. It has been used for a wide range of Earth remote sensing applications including disaster monitoring, Earth imaging and surveillance. Instead of using a large real aperture antenna, SAR uses a large virtual antenna that is formed by the relative motion between the radar platform and target to achieve high-resolution images.

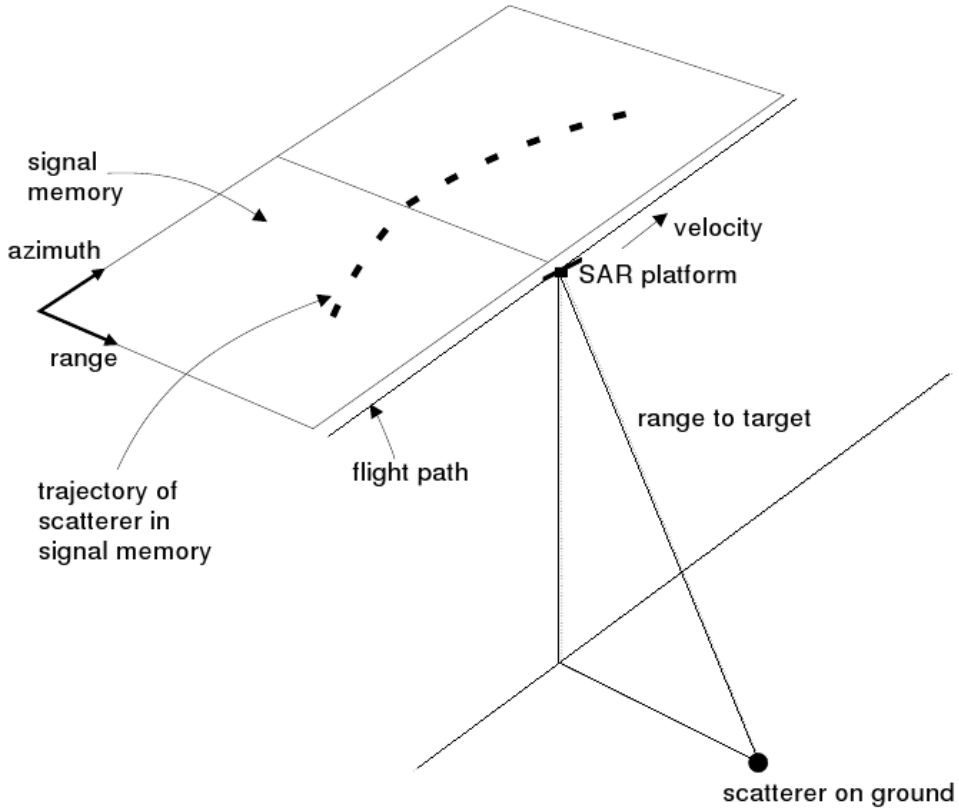

FIGURE 3.1: SAR geometry (Clemente, 2013)

A standard space-based SAR operation geometry is shown in Figure 3.1. The radar transmits a pulse to the surface in the direction perpendicular to the direction of travel and then receives its echo. The received signal will be processed on-board or at the ground station, depending on the mission. The femtosatellite is not capable of processing the SAR signal on-board. It will be transmitted to the carrier spacecraft for processing and down-linking to an Earth ground station.

3.3 Synthetic Aperture Radar Signal Processing

3.3.1 Signal Model

The simplified transmitted signal s_{tx} can be expressed as (Cumming et al., 2005):

$$s_{tx}(t) = w_r(t)\cos\left(2\pi f_o \pm \frac{\pi B_0 t^2}{T_r}\right) \tag{3.1}$$

It is a function of the fast time t, which is sampled continuously. The transmit envelop is represented by w_r. The signal's carrier frequency is f_0 and bandwidth is B_0, while the range chirp pulse duration is T_r. The approximate resolution in the range direction, ρ_r, can be expressed as (3.2):

$$\rho_r \approx \frac{c}{2B_0} \tag{3.2}$$

where c is the speed of light.

The demodulated received signal $s_{rx}(t,\tau)$ can be expressed as (Cumming et al., 2005):

$$\begin{aligned} s_{rx}(t,\tau) = \sum_{k=0}^{K-1} \Bigg[& F_k w_a(\tau-\tau_c) w_r\left(t-\frac{2R(\tau,k)}{c}\right) \\ & \exp\left(-j2\pi f_o \frac{2R(\tau,k)}{c} + j\pi K_r\left(t-\frac{2R(\tau,k)}{c}\right)^2\right)\Bigg] \\ & + n(t,\tau) \end{aligned} \tag{3.3}$$

It is a function of the fast time t and slow time τ, which is sampled at the pulse repetition frequency. The scatterers' identifier is k and the attenuation factor is F_k. The range is represented by $R(\tau,k)$ and the range chirp pulse frequency is K_r. The antenna pattern is implemented by w_a and the Gaussian noise is n and τ_c is the centre of slow time.

3.3.2 Radar System Configuration

There are two main radar configurations: mono-static and bi-static, which can be defined based on the bi-static angle of the radar system. The bi-static angle, β, is the angle subtended between the transmitter, target and receiver as shown in Figure 3.2.

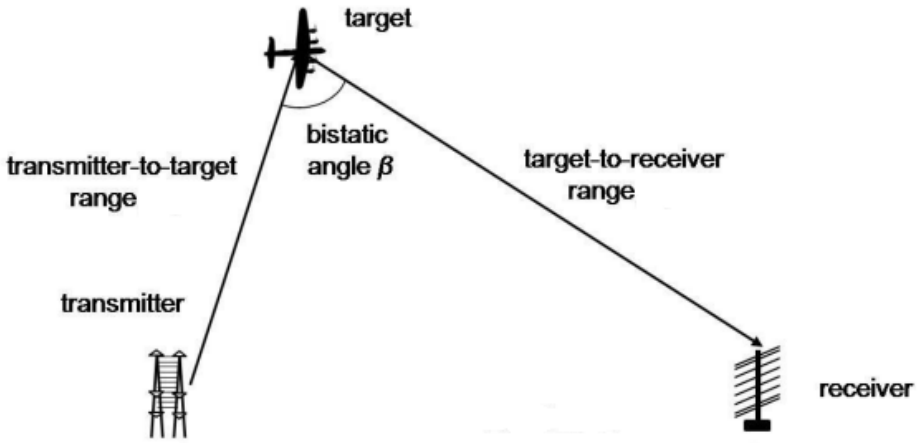

FIGURE 3.2: Bi-static radar (Griffiths et al., 2010)

Mono-static is when the transmitter and receiver of the radar system are collocated. The bi-static angle of a mono-static radar system is 0°. Instead, bi-static is when the transmitter and receiver of the radar system are spatially separated compared to the target distance.

There are four classes of bi-static radar configurations (Cherniakov, 2008; Griffiths et al., 2010). Pseudo mono-static is when the bi-static angle is close to 0°. In this configuration, the estimated range between the radar system and the target is orders of magnitude larger than the distance between the transmitter and the receiver. The femtosatellite swarm and carrier spacecraft system will operate in this configuration during the Earth remote sensing mission. A simulated SAR mission is evaluated later in Chapter 6.

Forward scatter radar is when the bi-static angle is equal or close to 180°. Jayasimha et al. provides an example of when orbital debris is close to the line-of-sight between a satellite and ground station (Jayasimha et al., 2013). This is widely used in space debris detection radar systems (Jayasimha et al., 2013; Muntoni et al., 2017; Persico et al., 2019).

Multi-static radar is when there are more then 2 elements in the radar system. It is a generalisation of the bi-static radar system and includes single-input-multi-output (SIMO), multi-input-single-output (MISO) and multi-input-multi-output (MIMO). Passive radar is when there is no transmitter in the radar system. It operates from non-cooperative sources of illumination. Persico et al. investigate the feasibility of space situational awareness for CubeSat platforms (Persico et al., 2019). It was demonstrated that a forward scatter passive radar is capable of detecting a 20 cm^2 target in a 600 km orbit. The femtosatellite swarm to be considered later is capable of space debris detection when configured as a forward scatter passive radar.

The raw SAR data will be arranged into a 2-D matrix consisting of range and azimuth, shown in Figure 3.1. This can be considered as a superposition of the point scatterers' response

which spreads in both range and azimuth. SAR processing will compress that response back to a single point. This can be achieved by applying a matched filter. The data will be processed separately in range and azimuth due to the difference time-scale. A common algorithm for SAR signal processing is the range-Doppler algorithm, which will now be considered.

3.3.3 Range-Doppler Algorithm

The range-Doppler algorithm (RDA) is a widely used algorithm for processing SAR data, developed by MacDonald Dettwiler and Associates and NASA JPL (Cumming et al., 2005). It takes advantage of the large difference in the time-scale of range and azimuth to process data separately. RDA applies range cell migration correction (RCMC) in the range-Doppler domain to correct the hyperbolic behaviour of the target trajectories (Cumming et al., 2005). The range-Doppler domain means range-time and azimuth-frequency. RDA is designed for simplicity and efficiency. It can be applied to a block of SAR data and is a one-dimensional process during data processing. A block diagram of RDA is shown in Figure 3.3.

The range compression is achieved by applying the matched filter in the range direction. It multiplies the data and the range reference function in the frequency domain for better efficiency. First, each azimuth bin is processed by a fast Fourier transform (FFT). Next, it multiplies the result by the range reference function in the range direction in the frequency domain. Last, an inverse fast Fourier transform (IFFT) is applied in the range direction to convert the data back to the time domain. An azimuth FFT is then applied to the result from the last step, converting it into the range-Doppler domain. The data is shifted in the range direction based on the target trajectories for range cell migration correction. The azimuth compression is utilised

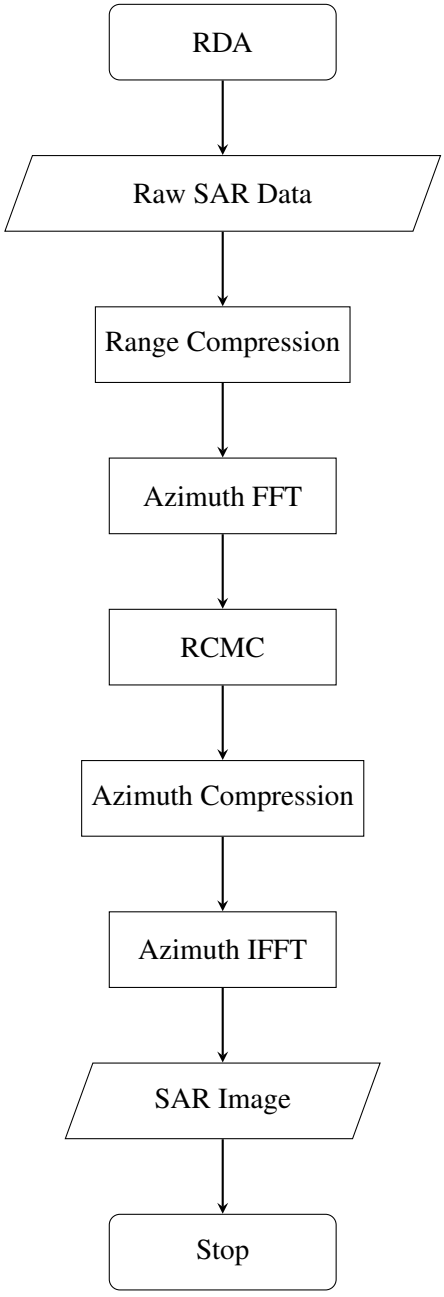

FIGURE 3.3: Block diagram of RDA

by multiplying data with the azimuth reference function in the azimuth direction. Finally, applying azimuth IFFT to the data to convert the data back to the time domain results in the final processed SAR image.

3.4 Current Spaceborne Missions

Compared to S-band (2 to 4 GHz) and C-band (4 to 8 GHz), X-band (8 to 12 GHz) features shorter wavelengths, therefore, a smaller antenna can be used. In addition, X-band radar can achieve higher spatial resolution (Marzano et al., 2011). Ku-band (12 to 18 GHz) and above would introduce challenges for radar payload hardware design and it has a higher attenuation due to the shorter wavelength. X-band is the most feasible option for femtosatellite Earth remote sensing missions.

3.4.1 TerraSAR-X and TanDEM-X

There have been some very successful spaceborne SAR missions in recent years. The TerraSAR-X mission was launched in June 2007, jointly developed by the German Aerospace Centre (DLR) and EADS Astrium (now Airbus Defence and Space). It carries a SAR payload operating at X-band in a dawn/dusk SSO (Melvin et al., 2011). A summary of the TerraSAR-X specifications is listed in Table 3.1. TerraSAR-X is able to reliably provide excellent radar images with a resolution up to 1 m in the spotlight mode.

TerraSAR-X could only operate as a mono-static SAR system until TanDEM-X was launched in June 2010. TanDEM-X is designed for digital elevation mesurement (DEM) and is almost

TABLE 3.1: TerraSAR-X specifications (Melvin et al., 2011)

TerraSAR-X	Value
Orbit altitude	514.8 km
Inclination	97.44°
Eccentricity	0.001
Argument of perigee	90°
Centre frequency	9.65 GHz
Bandwidth	300 MHz

identical to TerraSAR-X. With TanDEM-X flying beside TerraSAR-X closely in formation-flying, they are orbiting each other in the relative motion frame. The combined bi-static SAR configuration is able to provide elevation data in addition to the 2D radar images. The results are published in WorldDEM in 2014 and the data is available for the entire globe. Krieger et al. investigated the performance of an interferometric SAR mission enabled by formation-flying and proposed Tandem-L to further enrich the capability of spaceborne Earth remote sensing (Krieger, Hajnsek, et al., 2010).

3.4.2 COSMO-SkyMed

In contrast to formation-flying, spaceborne SAR also utilises constellations. COSMO-SkyMed (COnstellation of small Satellites for the Mediterranean basin Observation) was developed by the Italian Space Agency (ASI) and launched during June 2007 and November 2010 (Bianchessi et al., 2008). This mission consists of 4 satellites in a constellation with 90° phase shift along their orbit. Similar to TerraSAR-X, COSMO-SkyMed is operating in a dawn/dusk SSO and

carries an X-band SAR payload. A summary of the COSMO-SkyMed specifications is listed in Table 3.2.

TABLE 3.2: COSMO-SkyMed specifications (Bianchessi et al., 2008)

COSMO-SkyMed	Value
Orbit altitude	619.6 km
Inclination	97.86°
Eccentricity	0.00118
Argument of perigee	90°
Centre frequency	9.6 GHz
Bandwidth	400 MHz

3.4.3 Capella Constellation

The Capella constellation was developed by the Capella Space from the United States. Synthetic aperture radar satellites have been launched since 2018 and the constellation will consist of 36 individual synthetic aperture radar satellites in 12 different orbit planes by 2021 (Farquharson et al., 2018). Different from TerraSAR-X and COSMO-SkyMed, the Capella constellation is operating in polar orbit instead of SSO. When fully deployed, the Capella constellation will able to provide an hourly visit rate. A summary of the Capella constellation specifications is listed in Table 3.3.

All discussed spaceborne missions are using X-band SAR, two of which operate at a dawn/-dusk SSO. This is a widely used combination for Earth remote sensing missions. This will also

TABLE 3.3: Capella constellation specifications (Farquharson et al., 2018)

Capella	Value
Orbit altitude	485 - 525 km
Inclination	90°
Argument of perigee	90°
Centre frequency	9.4 - 9.9 GHz
Bandwidth	500 MHz

be used for the femtosatellite swarm later in Chapters 4, 5 and 6.

3.5 Summary

This chapter presented the concept of synthetic aperture radar with a focus on Earth remote sensing missions. Related SAR signal models and radar configurations are reviewed and discussed. A commonly used mono-static SAR signal processing range-Doppler algorithm is introduced to evaluate the performance of the femtosatellite swarm later in Chapter 6. Finally, three current SAR missions are also introduced to demonstrate the capability of the mission concept introduced in Chapter 4.

Chapter 4

Femtosatellite Design

4.1 Introduction

In this chapter, a novel femtosatellite design and mission concept based on the utilisation of solar radiation pressure (SRP) is proposed. As noted in Section 2.4, current femtosatellites use commercial off-the-shelf integrated circuits to reduce cost. However, the mission capabilities of such femtosatellites are limited by their propulsion and power subsystems. In order to further exploit the mission capability of femtosatellites, an overview of a new femtosatellite concept and mission is presented in Section 4.2. A novel femtosatellite design for such a mission is then described in Section 4.3. In Section 4.3.4, a detailed mission configuration is developed for the novel femtosatellite design. The hardware design for the femtosatellite is provided and evaluated in Section 4.4. The application of the proposed configuration will be investigated in Chapters 5 and 6.

4.2 Femtosatellite Mission Overview

In this thesis, the proposed demonstration mission is to exploit the femtosatellite concept for synthetic aperture radar for Earth remote sensing. With the unique advantages of femtosatellites, the overall system mass can be reduced, and so, the combined launch cost of the mission can be reduced. Moreover, a femtosatellite swarm allows a large, distributed system to be deployed to enhance mission performance.

The proposed mission concept is inspired by TerraSAR-X and TanDEM-X that were described in Section 3.4.1. Femtosatellites are configured as the receivers for a bi-static SAR system. A swarm of femtosatellites will operate in addition to a carrier spacecraft. During the mission, the carrier spacecraft is responsible for the radar signal transmission and communication to a ground station. The femtosatellite swarm will be used as a passive receiver. With this bi-static configuration, enhanced performance can be delivered by implementing advanced radar signal processing. The femtosatellites will operate close to the carrier spacecraft, which can be considered as relative orbital motion. The distance between the femtosatellites and the carrier spacecraft is controlled by using active orbit control which will be discussed in Chapter 5, and will focus on the orbit dynamics and control of the femtosatellites. The radar performance of the femtosatellite swarm will be considered in Chapter 6.

The proposed mission orbit is similar to the TerraSAR-X and TanDEM-X missions which use dawn/dusk Sun-synchronous orbits at 700 km altitude. The selection of the orbit altitude will be explored further in detail in Chapter 5. The proposed Earth remote sensing mission now forms the basis of the femtosatellite preliminary design.

4.3 Femtosatellite Preliminary Design

In order to design the femtosatellite for the proposed mission, a novel SRP enabled design approach is proposed to fully exploit the capabilities of femtosatellites for the chosen orbit configuration. The proposed design is inspired both by current femtosatellite prototypes and conventional satellites. It utilises SRP for attitude control and orbit control. The proposed design would be capable of undertaking the proposed SAR mission.

4.3.1 Design Objectives

The main objective of the novel design is to configure a femtosatellite platform which will enable swarm usage for the Earth remote sensing mission. Compared to conventional satellites, one distinct feature of femtosatellites is their low mass, as discussed in Section 2.2. As noted in Table 2.1, the femtosatellite class has a wet mass lower than 100 g. This is the core of the femtosatellite concept.

In addition to being lightweight, femtosatellites require a compact design. Before deployment from the carrier spacecraft, their small size will increase the efficiency of packing in the carrier spacecraft. This objective can be achieved by a flat design or a folded structure. Most of the femtosatellites designs noted in Section 2.4 feature a simple flat design. The origami folding robot introduced by Boyvat et al. also presents a promising method to enable complicated geometries (Boyvat et al., 2017). Combining low mass and size, femtosatellites can be launched by multiple methods: by a carrier spacecraft, as a secondary payload to similar orbits, or as a dedicated launch. A large number of femtosatellites in a swarm will improve mission performance.

Also, to enhance the femtosatellite concept, it is necessary that a femtosatellite swarm is capable of executing a complete mission. This requires that the femtosatellite has an orbit lifetime sufficient for the mission. Moreover, an on-the-fly re-configurable software design will boost the usability of the femtosatellite significantly.

To further increase the mission capability of femtosatellites, passive or active orbit control strategies can be considered. Since femtosatellites are mainly designed to operate in Low Earth Orbit (LEO), a de-orbit solution is also required to reduce the risk of swarms of devices becoming space debris.

4.3.2 Design Methodologies

To meet the design objectives noted above, a review of current femtosatellite designs and other small satellites is provided. WikiSat and Sprite were reviewed in Section 2.4, both of which feature a flat design geometry. Compared to other geometries, a flat plate is the easiest option to manufacture. This is the fundamental structure of most electronic devices. Compared to other geometries, a flat design also features the maximum projected area which will benefit orbit control using SRP. Three common geometries are investigated: a plate, cube and sphere. Figure 4.1 illustrates those geometries with the same characteristic length-scale L and the thickness coefficient ε ($\varepsilon << 1$) for the plate (Atchison et al., 2011).

SRP and atmospheric drag (AD) are the major sources of perturbations on femtosatellites. Both are directly proportional to their projected area (Vallado, 2013). For a dawn/dusk Sun-synchronous orbit, the incident sunlight is assumed perpendicular to the orbit plane, therefore, it is always perpendicular to the velocity vector of the femtosatellite and the atmospheric drag

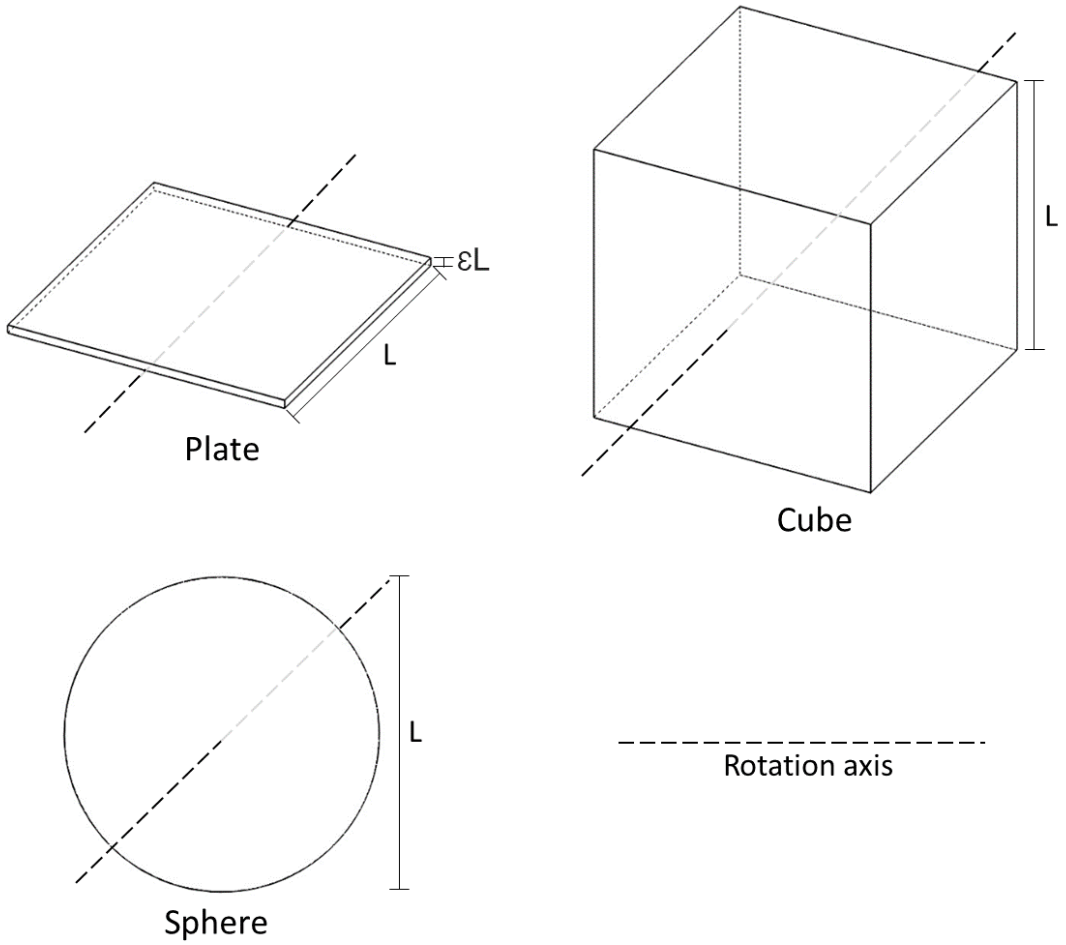

FIGURE 4.1: Definition of femtosatellite geometries

force it experiences. A higher maximum/minimum projected area ratio therefore creates the possibility of increasing the effect of SRP while decreasing the effect of atmospheric drag.

To enable orbit control, a torque will be generated by the femtosatellite to change its attitude. The torque required for attitude control is proportional to the femtosatellite moment of inertia. A lower moment of inertia means that less torque is required to change the attitude angle for a given required angular acceleration. Table 4.1 presents a comparison between

common geometries for femtosatellite designs, where ρ is the mean density of the spacecraft.

TABLE 4.1: Comparison of femtosatellite geometries (Atchison et al., 2011)

Geometry	Min. projected (for AD)	Max. projected (for SRP)	Max/min ratio	Area-to-mass ratio (for SRP)	Moment of inertia
Plate	εL^2	L^2	$\frac{1}{\varepsilon}$	$\frac{1}{\varepsilon\rho L}$	$\frac{\varepsilon}{12}\rho L^5$
Cube	L^2	$\sqrt{3}L^2$	$\sqrt{3}$	$\frac{\sqrt{3}}{\rho L}$	$\frac{1}{6}\rho L^5$
Sphere	$\frac{\pi}{4}L^2$	$\frac{\pi}{4}L^2$	1	$\frac{3}{2\rho L}$	$\frac{\pi}{60}\rho L^5$

Combining both projected area and moment of inertia, the flat plate is the most suitable option for the femtosatellite geometry design for the proposed SAR mission. It features the highest maximum/minimum projected area ratio when the normal to its surface is perpendicular to the orbit plane. Especially in this configuration, atmospheric drag is negligible due to the minimum projected area. Compared to other geometries, a plate also has the highest area-to-mass ratio for SRP and lowest moment of inertia for attitude control if ε is small ($\varepsilon << 1$).

4.3.3 Proposed Design

As noted, the two major challenges for femtosatellites are the propulsion and power subsystems. According to Section 2.3, these challenges can be overcome by using solar radiation pressure for orbit control. In order to fully explore the potential of using solar radiation pressure on a femtosatellite, a novel preliminary design has to be defined. It will also be used as the concept demonstrator and the test subject for active orbit control later in Chapter 5.

Taking the design objectives and methodologies into consideration, the proposed design is composed of a flat-bubble shaped femtosatellite (Cao et al., 2015). The femtosatellite is built on

Kapton film as an alternative to a conventional glass fibre based printed circuit board to reduce weight and provide flexibility (McLeod, 2003). The use of flexible material also satisfies the low mass design objectives. The flexural stress on the femtosatellite could also provide energy for the initial ejection from the carrier spacecraft. This would therefore reduce the complexity of the femtosatellite release mechanism on the carrier spacecraft.

The onboard components are assumed to be commercial off-the-shelf (COTS) to reduce cost. All core electronics in the centre of the femtosatellite are covered by an extra layer of Kapton film on top to protect them from radiation and provide passive thermal control. The thin film solar panels around the edge are not covered to maximise the solar power generation.

The design features a high area-to-mass ratio which, again, enables the femtosatellite to take advantage of solar radiation pressure for propulsion without onboard propellant. Electrochromic panels in each corner can be controlled electronically to change their transparency between reflective and black to enable attitude control (Lücking et al., 2012; Mingotti et al., 2014). Size and weight are greatly minimised by integrating the propulsion and power subsystems together. A rendered image of the proposed design is shown in Figure 4.2

The onboard firmware of the femtosatellite would be able to reconfigure on-the-fly to perform updated mission tasks, for example, radar receiver mode and communication relay mode. This will increase usability and further enhance the mission capability of the femtosatellites.

4.3.4 Mission Concept

With the proposed femtosatellite design, a mission concept is proposed to evaluate the feasibility of a fetmosatellite swarm. As noted in Section 4.2, the proposed mission is inspired by the TerraSAR-X and the TanDEM-X missions. The femtosatellite swarm can operate on a

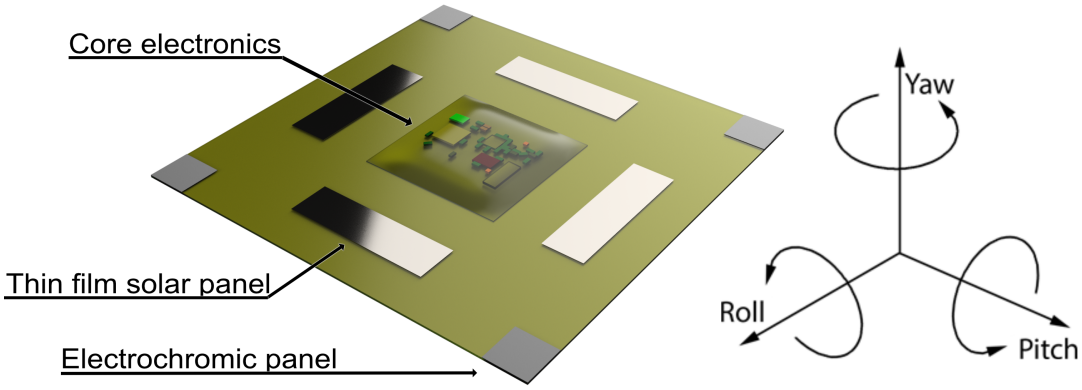

FIGURE 4.2: Rendered flat-bubble shaped design

dawn/dusk Sun-synchronous orbit for the proposed Earth remote sensing mission. Orbit specifications are shown in Table 4.2. The orbit altitude will investigated further in Section 5.2.2.

TABLE 4.2: Femtosatellite mission specifications

Femtosatellite	Value
Orbit altitude	700 *km*
Inclination	98.19°
Argument of perigee	90°
Eccentricity	0

The orbit plane of such an SSO is perpendicular to the incoming sunlight. Therefore the femtosatellite will operate under maximum illumination during the entire orbit to maximise the effect of SRP and power generation.

The normal to the femtosatellite surface would be parallel to the normal to the orbit plane.

According to Table 4.1, this will maximise the projection area for SRP while minimising the effect of atmospheric drag. During the Earth remote sensing operation, the femtosatellite would rotate around its velocity vector to point the radar antenna at the area of interest. Under this condition, the normal of the femtosatellite surface would remain perpendicular to the velocity vector, so that atmosphere drag remains minimised.

In order to maximise the benefits of SRP for orbit control and to maintain a high area-to-mass ratio, a flat micro-strip antenna and surface-mount chip antenna are considered for the Earth remote sensing mission. According to the femtosatellite orbit and the required attitude of the femtosatellite, the antenna design will vary, for example, a patch antenna whose main lobe is parallel to the antenna normal, or a Vivaldi antenna whose main lobe is perpendicular to the antenna normal. The design could vary from a single or array design depending on the radar carrier frequency and beam-forming requirements. The antenna could also be placed symmetrically and controlled by an electrical relay to reduce the required manoeuvre along the femtosatellite's yaw axis. A surface-mount chip antenna can be used for communication between the femtosatellites and the carrier spacecraft. This features a smaller footprint and a more stable performance than other commonly used antennas. A mission concept is illustrated in Figure 4.3. The carrier spacecraft would be responsible for transmitting radar signals and collecting received signals from the femtosatellites. The collected data would then be processed or compressed depending on the processing capability of the carrier spacecraft before sending the data back to a ground station.

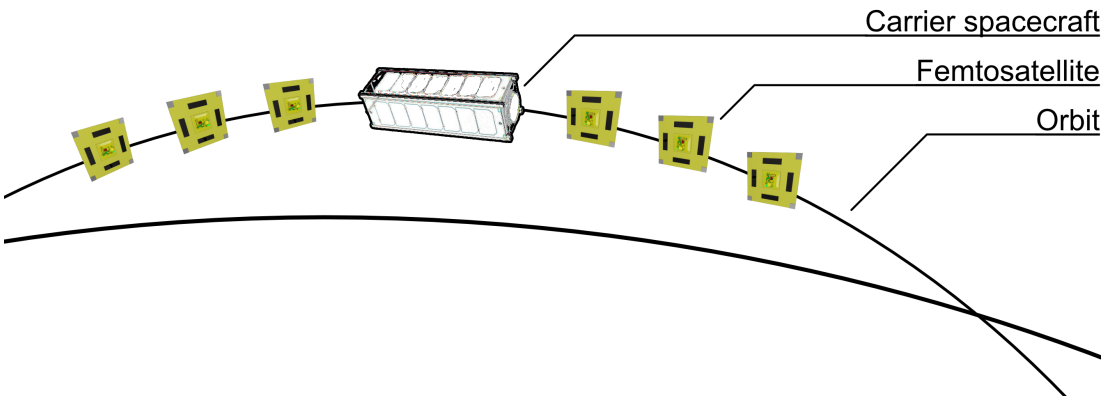

FIGURE 4.3: Mission concept

4.4 Femtosatellite Hardware Design

Since the power supply and energy storage on the femtosatellite is limited due to its small size and low mass, a Texas Instruments MSP430F2274-EP ultra-low-power microcontroller and CC2520 RF transceiver have been chosen to minimize power consumption (Cao et al., 2015). These components are the core electronics for the femtosatellite command and data handling and communication subsystems, as described in Section 2.3.

Compared to other microcontrollers, the MSP430F2274 also includes two configurable operational amplifiers (Texas Instruments, 2020c). This combination could be reconfigured in software for different objectives to enhance mission capability. The device working temperature of $-40\,^{\circ}\text{C}$ to $85\,^{\circ}\text{C}$ is a limitation for some applications. MSP430F2274-EP is an enhanced version for defence, aerospace and medical applications. Compared to the standard model, the main feature of the EP model is the military temperature range of $-40\,^{\circ}\text{C}$ to $105\,^{\circ}\text{C}$. The power consumption is 0.7 μA in standby mode and 270 μA in active mode.

CC2520 is an RF transceiver designed for low power wireless sensor networks at 2.4 GHz (Texas Instruments, 2020b). The working temperature range is $-40\,^{\circ}\text{C}$ to $125\,^{\circ}\text{C}$. Combined

with the EP model microcontroller, the reliability and survivability of the femtosatellite core electronics would be improved in extreme thermal conditions. It capable of up to 250 $kbps$ data rate with a power consumption 25.8 mA for transmitting and 18.5 mA for receiving. For the synthetic aperture radar, which will be introduced in Chapter 6, with Pulse Repeat Frequency of 3000 Hz for a duration of 0.5 s, a swath width of 500 m, a bandwidth of 100 MHz and with a 5% communication overhead (Agrawal et al., 2011), the estimated total received data is 160.26 *megabit*, which is equivalent to 20.03 *megabyte*. The details of the SAR signal space are listed in Table 4.3.

TABLE 4.3: SAR signal space specifications

Parameter	Value
Azimuth	1500 *bins*
Range	4668 *bins*
Date depth	12 *bits*
Data format	Complex I/Q
Communication overheads	5%
Data rates	250 *kbps*
Duration	11.20 *minutes*

It would take 11.20 *minutes* to transmit all received data to the carrier spacecraft. This could be considered as the gap between individual radar images. In addition, the CC430 series is also available for simple applications to reduce mass, which has an integrated microcontroller and sub-1GHz RF transceiver (Hu et al., 2019).

The attitude determination subsystem of the femtosatellite is enabled by a TDK InvenSense MPU-9250 inertia measurement unit (IMU) (InvenSense, 2020). This is a 9 degree-of-freedom IMU consist of a 3-axis gyroscope, 3-axis accelerometer and 3-axis magnetometer. The working temperature is $-40\,^{\circ}$C to $85\,^{\circ}$C. The attitude control and propulsion subsystems are enabled by using SRP. These will be discussed and further evaluated in Chapter 5.

The power subsystem includes solar panels and an energy harvesting chip. Thin film solar panels from Alta Devices (Alta Devices, 2020) are used for power generation. This dual junction Gallium Arsenide (GaAs) photovoltaic solar panel features a high efficiency of 29%. The power density is estimated at 345 W/m^2 for the space environment. Combined with an Analog Devices ADP 5090 energy harvesting ultra-low-power boost regulator (Analog Decice, 2020), low voltage power generated from the solar panels can be regulated to supply a stable 3 V power to other subsystems with 90% efficiency.

4.4.1 Budget Analysis

A power budget of the femtosatellite is listed in Table 4.4. The command and data handling power consumption is based on the Texas Instruments MSP430F2274-EP microcontroller (Texas Instruments, 2020c). The communication power consumption is based on the Texas Instruments CC2520 RF transceiver (Texas Instruments, 2020b). The peak condition is when the system is transmitting and receiving data simultaneously at full speed. The attitude determination power consumption is based on the TDK InvenSense MPU-9250 IMU (InvenSense, 2020). The attitude control power consumption is based on Rdot Display printed flexible electrochromic displays (Displays, 2020). The payload power consumption is based

on the Texas Instruments ADS5295 octal channel 12 *bit*, 100 *Msps* high-signal-to-noise-ratio and low-power analogue-to-digital converter (Texas Instruments, 2020a).

TABLE 4.4: Power budget

Subsystems	Idle (mW)	Peak (mW)
Command and data handling	0.002	0.81
Communication	4.8	133
Attitude determination	10.5	10.5
Attitude control	0	10
Payload	5	190
Redundancy (10%)	1.63	34.4
Total power consumption	17.9	378.7

Considering the 90% efficiency of the power boost regulator (Analog Decice, 2020), a total power of $420mW$ is required from solar panels, therefore, 4 of 35×10 mm solar panels are placed around the core electronics to provide an even mass distribution. No batteries are required for this configuration to reduce mass since the femtosatellites will be on a dawn/dusk SSO. When the femtosatellite is not perpendicular to the incident sunlight less power will be generated from the solar panels, so the communication and payload subsystems could be turned off to reduce total power consumption and ensure sufficient power for attitude control. A schematic of the femtosatellite concept is illustrated in Figure 4.4.

The mass budget of the femtosatellite concept is listed in Table 4.5. The mass of each module is estimated based on common electronics and existing femtosatellites (Janson and

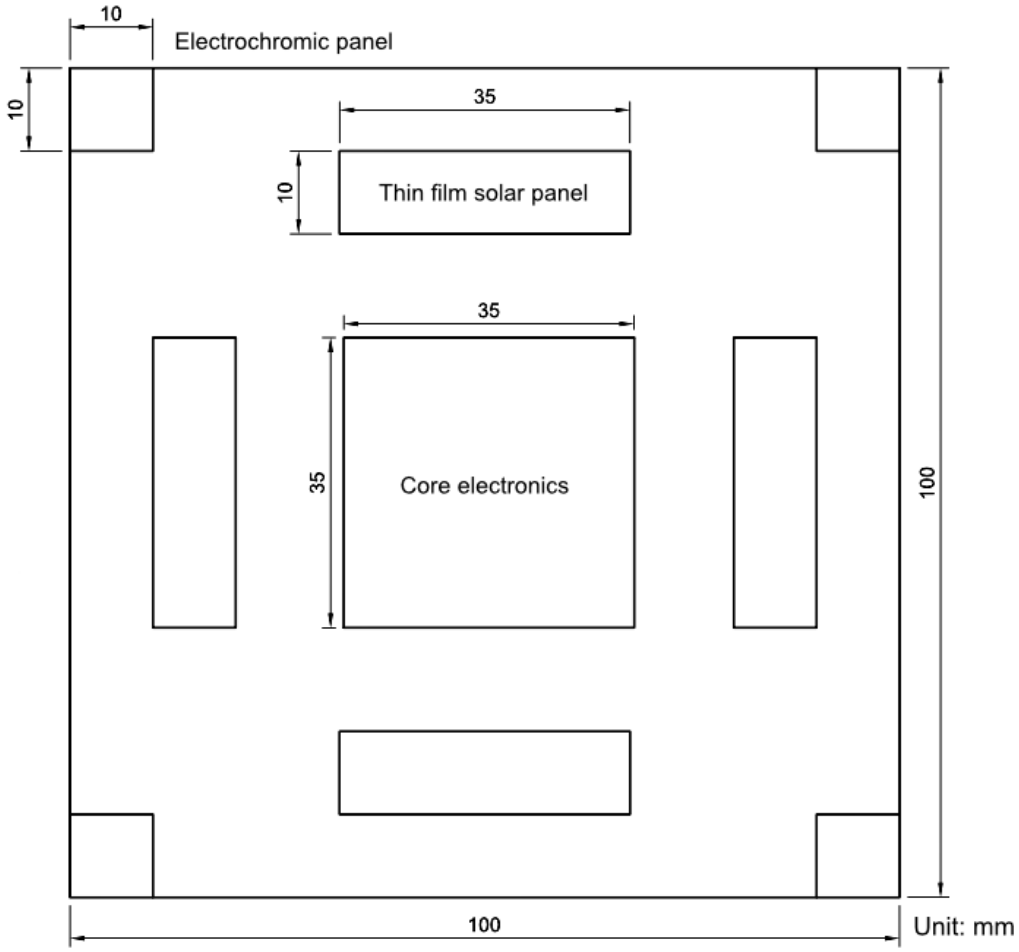

FIGURE 4.4: Flat-bubble shaped design schematic - top view

Barnhart, 2013). A payload of 50% of the total mass is included to ensure a margin for mission capability (Larson et al., 1999).

Due to the small size and low power design, the thermal control subsystem is a passive design with Kapton film. The condition for thermal equilibrium can be expressed as (Janson, 1995):

$$\alpha_s A_s G_s + \alpha_s A_e G_r + \varepsilon_s A_e G_e + Q_{int} = \varepsilon_s \sigma T^4 A_r \tag{4.1}$$

TABLE 4.5: Weight budget

Components	Weight (g)
Core electronics	4
Solar panels	2
Electrochromic panels	1
Structural	3
Payload (50%)	10
Total	20

where α_s is the spacecraft surface solar absorptivity, ε_s is the spacecraft infrared emissivity, A_s is the surface area for absorption of solar energy, A_e is the surface area for absorption of the radiation from the Earth, A_r is the surface area for heat radiation, G_s is the direct solar flux, G_r is the reflected solar flux from the Earth surface, G_e is the thermal energy radiated by the Earth, σ is the Stefan-Boltzmann constant, Q_{int} is the internal heat generation rate and T is the spacecraft surface temperature.

For the mission concept described in Section 4.3.4, where the normal to the femtosatellite is perpendicular to the orbit plane ($G_r = 0, G_e = 0$), the temperature of the femtosatellite can be expressed as:

$$T = \sqrt[4]{\frac{\alpha_s A_s G_s + Q_{int}}{\varepsilon_s \sigma A_r}} \tag{4.2}$$

Base on the design shown in Figure 4.4, the surface area is 0.1 m^2 for absorption of solar energy and 0.2 m^2 for heat radiation. The solar absorptivity and infrared emissivity are based on the characteristic of the Kapton film structure (Kang et al., 2016). The solar flux of 1370 W/m^2 is

TABLE 4.6: Femtosatellite specifications

Parameter	Value
α_s	0.4
A_s	0.01 m^2
A_r	0.02 m^2
G_s	1370 W/m^2
ε_s	0.8
σ	5.67×10^{-8} $W/(m^2T^4)$
$Q_{internal}$	Idle: 17.9 mW
	Peak: 378.7 mW

based on the LEO environment at 1 AU (Janson, 1995). With the parameters listed in Table 4.6, the thermal equilibrium temperature of the femtosatellite is estimated as 279.0 K and 283.5 K in the idle and peak power conditions. These results will be used in Chapter 6 for the radar performance analysis.

If the femtosatellite was in an alternative orbit whose orbit plane is 45° to the incident sunlight and the normal of the femtosatellite remains perpendicular to the orbit plane ($G_r = 0, G_e = 0$), the femtosatellite will enter eclipse and go through a thermal cycle during each orbit. By numerically integrating a lumped-heat-capacity model, expressed as (Janson, 1995):

$$\alpha_s A_s G_s + \alpha_s A_e G_r + \varepsilon_s A_e G_e + Q_{int} - \varepsilon_s \sigma T^4 A_r = \frac{\mathrm{d}}{\mathrm{d}\,t}(mc_p T) \tag{4.3}$$

where c_p is the heat capacity of the Kapton structure of femtosatellite ($c_p = 1090\ J/(kgK)$,

Doorly et al., 1987), the dynamic temperature of the femtosatellite in such an alternative orbit is shown in Figure 4.5.

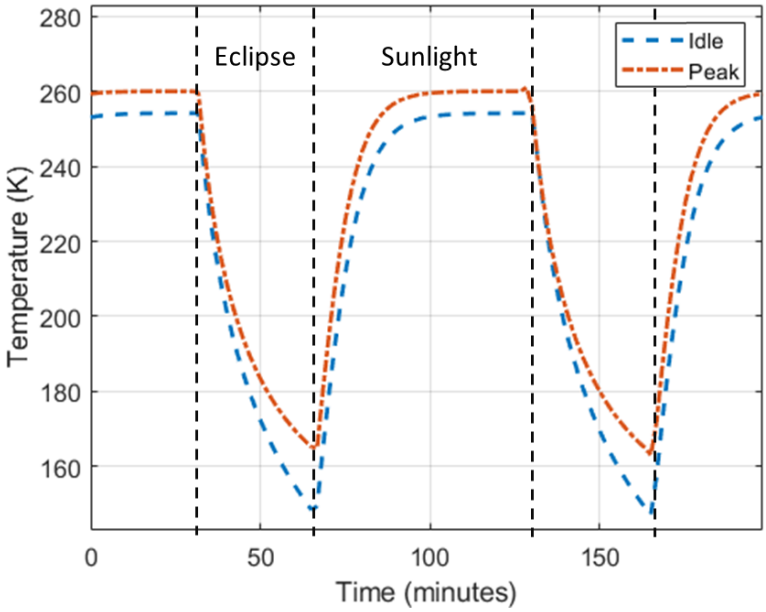

FIGURE 4.5: Dynamic temperature profile

From Figure 4.5, it can be seen that the temperature will decrease during eclipse and increase when illuminated by sunlight. The femtosatellite will reach a maximum equilibrium temperature of 254 K when idle or 260 K when working at the peak power condition. Compared to the mission concept described in Section 4.3.4, the maximum equilibria are lower due to the angle of the incident sunlight. The lowest temperatures during eclipse are 148 K and 165 K for the idle and peak conditions. These are lower than the working temperature of the electronic components, and therefore, may physically damage those core electronics (Gutierrez-D et al., 2001). From this analysis it is clear that the use of a dawn/dusk SSO provides key advantages for thermal control (uniform temperature) as well as continuous power generation.

4.5 Summary

In this chapter, a novel femtosatellite design and a novel mission concept have been proposed. They are based on existing femtosatellite designs and SAR missions introduced in Section 2.4 and 3.4. The design objectives and methodologies were listed and discussed in Section 4.3.1 and 4.3.2. In Section 4.3.3, a flat-bubble shape femtosatellite design has been described and a novel mission concept to take advantage of such design was proposed in Section 4.3.4. This mission configuration largely eliminates the influence of atmospheric drag, therefore simplifying the complexity of attitude control. The hardware design of the femtosatellite was provided in Section 4.4 based on the femtosatellite subsystems review in Section 2.3. A budget analysis was also provided in Section 4.4.1 to evaluate the power, mass and thermal performance of the femtosatellite. These result will be used in Chapters 5 and 6. The novel femtosatellite design features a high area-to-mass ratio of 0.5 m^2/kg to maximise the effect of SRP for orbit control. The orbital dynamics and control of the femtosatellite will now be investigated in Chapter 5.

Chapter 5

Femtosatellite Dynamics and Control

5.1 Introduction

In this chapter, integrated orbital dynamics and attitude control strategies are introduced to exploit the capability of the femtosatellite concept proposed in Chapter 4. All assumptions used in the chapter are listed in Section 5.1.1. This chapter focuses on the relative motion between the femtosatellite and the carrier spacecraft under the model described in Section 2.6. Based on these assumptions, the evolution of the orbital dynamics of the femtosatellite is established in Section 5.2 by investigating a force model comparing the effects of relative solar radiation pressure (SRP) and relative atmospheric drag. This model creates the foundation for orbit control in Section 5.3. With the active orbit control strategy developed, a swarm of femtosatellites could maintain a formation relative to the carrier spacecraft for the radar applications in Chapter 6. Two example scenarios are provided in Section 5.4 to demonstrate the active orbit control strategy.

5.1.1 Assumptions

A number of assumptions have been made to simplify the femtosatellite dynamical model for relative motion. The mission is assumed to be in a nearly circular orbit and the femtosatellites remain close[1] to the carrier spacecraft to enable the use of the linear Clohessy-Wiltshire or Hill's equation introduced in Section 2.6 (Vallado, 2013). The centre-of-mass coincides with the geometric centre of each femtosatellite and torques are generated by electrochromic panels. It is assumed that yaw control can be achieved by utilising a MEMS reaction wheel included in the core electronics which will not be considered here. This is independent from the roll and pitch control of the femtosatellite which will be achieved using SRP. The incident sunlight is assumed perpendicular to the orbit plane, so that a dawn-dusk orbit is assumed. The effect of SRP on the electrochromic panels is simulated as being at the outer edge of each panel instead of integrated along the panel surface.

5.1.2 Contributions

The main contribution of this chapter includes: integrating a generalised analytic solution of the Clohessey-Wiltshire equations with the attitude dynamics of the femtosatellite; a force analysis of a flat femtosatellite; and an active orbit control strategy for the femtosatellites based on attitude control. All contributions are demonstrated by example scenarios.

[1]The distance between the femtosatelite and the carrier spacecraft is below 0.1% of the orbit radius and so a linear approximation applies.

5.2 Orbital Dynamics

As noted in Section 4.3.4, the Earth remote sensing mission proposed is a bi-static synthetic aperture radar mission which includes a swarm of the femtosatellites as passive receivers and a carrier spacecraft as the transmitter. Therefore, this chapter will focus on the relative motion between the femtosatellites and the carrier spacecraft.

In the proposed mission, the distance between the femtosatellite and the carrier spacecraft will be maintained by utilising an SRP enabled orbit control strategy. With the assumptions noted in Section 5.1.1, this scenario fits the relative motion model introduced in Section 2.6.

During the Earth remote sensing mission, each femtosatellite is free-flying in close proximity to the carrier spacecraft. Due to perturbations, for example, atmospheric drag, the femtosatellites will drift away from the carrier spacecraft. Therefore, an orbit control strategy is required to maintain the formation. As noted in Section 2.3, solar radiation pressure is the most appropriate propulsion solution for orbit control for the femtosatellite platform.

5.2.1 Relative motion with external acceleration

The relative motion between the femtosatellite and the carrier spacecraft can be described by the linear Clohessy-Wiltshire equations introduced in Section 2.6.

By solving the Clohessy-Wiltshire Equations (2.2)[2] in Section 2.6, a generalised analytic solution for analysis and fast computation is found as follows:

$$x(t) = \left(\frac{\dot{x}_0}{\omega_n} - \frac{2a_y}{\omega_n^2}\right)\sin(\omega_n t) - \left(3x_0 + \frac{2\dot{y}_0}{\omega_n} + \frac{a_x}{\omega_n^2}\right)\cos(\omega_n t) + \frac{2a_y}{\omega_n}t + \left(4x_0 + \frac{2\dot{y}_0}{\omega_n} + \frac{a_x}{\omega_n^2}\right) \tag{5.1a}$$

$$y(t) = \left(6x_0 + \frac{4\dot{y}_0}{\omega_n} + \frac{2a_x}{\omega_n^2}\right)\sin(\omega_n t) + \left(\frac{2\dot{x}_0}{\omega_n} - \frac{4a_y}{\omega_n^2}\right)\cos(\omega_n t) - \frac{3a_y}{2}t^2 - \left(6\omega_n x_0 + 3\dot{y}_0 + \frac{2a_x}{\omega_n}\right)t + \left(y_0 - \frac{2\dot{x}_0}{\omega_n} + \frac{4a_y}{\omega_n^2}\right) \tag{5.1b}$$

$$z(t) = \frac{\dot{z}_o}{\omega_n}\sin(\omega_n t) + \left(z_0 - \frac{a_z}{\omega_n^2}\right)\cos(\omega_n t) + \frac{a_z}{\omega_n^2} \tag{5.1c}$$

$$\dot{x}(t) = \left(3\omega_n x_0 + 2\dot{y}_0 + \frac{a_x}{\omega_n}\right)\sin(\omega_n t) + \left(\dot{x}_0 - \frac{2a_y}{\omega_n}\right)\cos(\omega_n t) + \frac{2a_y}{\omega_n} \tag{5.1d}$$

$$\dot{y}(t) = -\left(2\dot{x}_0 - \frac{4a_y}{\omega_n}\right)\sin(\omega_n t) + \left(6\omega_n x_0 + 4\dot{y}_0 + \frac{2a_x}{\omega_n}\right)\cos(\omega_n t) - 3a_y t - \left(6\omega_n x_0 + 3\dot{y}_0 + \frac{2a_x}{\omega_n}\right) \tag{5.1e}$$

$$\dot{z}(t) = -\left(\omega_n z_0 - \frac{a_z}{\omega_n}\right)\sin(\omega_n t) + \dot{z}_0\cos(\omega_n t) \tag{5.1f}$$

By integrating the Clohessy-Wiltshire Equation (2.2b) without external acceleration ($a_y = 0$) it can be seen that

$$\int \ddot{y}\,\mathrm{d}t + \int 2\omega_n \dot{x}\,\mathrm{d}t = C \tag{5.2}$$

[2]The derivation of the Clohessy-Wiltshire equation analytical solution is provided in Appendix A

and so $\dot{y} + 2\omega_n x = C$ for some constant C.

Therefore, a new parameter $\Gamma = \dot{y}_0 + 2\omega_n x_0$ can be defined which again is constant and evaluated at the initial conditions of the femtosatellite at release. When the femtosatellite is free-flying ($a_x = a_y = 0$), from Equation (5.1e) it can be seen that

$$\dot{y}(t) = -2\dot{x}_0 \sin(\omega_n t) + (6\omega_n x_0 + 4\dot{y}_0)\cos(\omega_n t) - 3\Gamma \tag{5.3}$$

Then, the long-term average speed along the y-axis, $\bar{\dot{y}}$, can be written as

$$\bar{\dot{y}} = \frac{1}{T}\int_0^T \dot{y}(t)\mathrm{d}t \tag{5.4}$$

where $T = \dfrac{2\pi}{\omega_n}$ is the orbit period of the carrier spacecraft. Substituting $\dot{y}(t)$ with Equation 5.3, it can be found that

$$\bar{\dot{y}} = \frac{1}{T}\left(\frac{2\dot{x}_0}{\omega_n}\cos(\omega_n t) + \frac{6\omega_n x_0 + 4\dot{y}_0}{\omega_n}\sin(\omega_n t) - 3\Gamma\, t + C \Big|_0^T \right) \tag{5.5}$$

for some constant C, therefore

$$\bar{\dot{y}} = \frac{1}{T}\left(\frac{2\dot{x}_0}{\omega_n} - 3\Gamma T - \frac{2\dot{x}_0}{\omega_n} \right) \tag{5.6}$$

and so

$$\bar{\dot{y}} = -3\Gamma \tag{5.7}$$

When $\Gamma = 0$, the femtosatellite will therefore only have periodic motion relative to the carrier spacecraft and will not drift. This result will be used later to assess orbit control strategies.

5.2.2 Force Analysis

After ejection from the carrier spacecraft, typically with $\Gamma \neq 0$, the femtosatellites will drift without active orbit control. By using the electrochromic panels on each corner, each femtosatellite can adjust its attitude to achieve active orbit control using solar radiation pressure. According to Equation (5.1c), the motion along the z-axis is decoupled from the x-axis and the y-axis. The length-scale of motion along the y-axis is typically larger compared to the x-axis. According to Equation (5.1a) and (5.1b), the ratio of the oscillation range between the y-axis and x-axis is 2:1 when $\Gamma = 0$. Therefore, an external force applied along the y-axis is used to constrain the distance between the femtosatellites and the carrier spacecraft to ensure a coherent swarm is established. This can be controlled via modulation of the attitude angle of the femtosatellite relative to the xy-plane (Lücking et al., 2012; Mingotti et al., 2014). The force model for a femtosatellite is shown in Figure 5.1, demonstrating the effect of solar radiation pressure and atmospheric drag, where α is the angle between the femtosatellite surface normal and the flight direction.

Solar radiation pressure (SRP) and atmospheric drag (AD) are the main external forces applied to both the femtosatellites and the carrier spacecraft. The consequences of those two external forces are now considered. With the carrier spacecraft acceleration (Carr) included, the total differential acceleration (Total) caused by the external forces are summarised as:

$$\begin{cases} a_{y,Total} = a_{y,SRP} + a_{y,AD} - a_{y,Carr} \\ a_{z,Total} = a_{z,SRP} + a_{z,AD} - a_{z,Carr} \end{cases} \tag{5.8}$$

From Figure 5.1 it can be seen that the y-axis acceleration can be reversed, while the x-axis

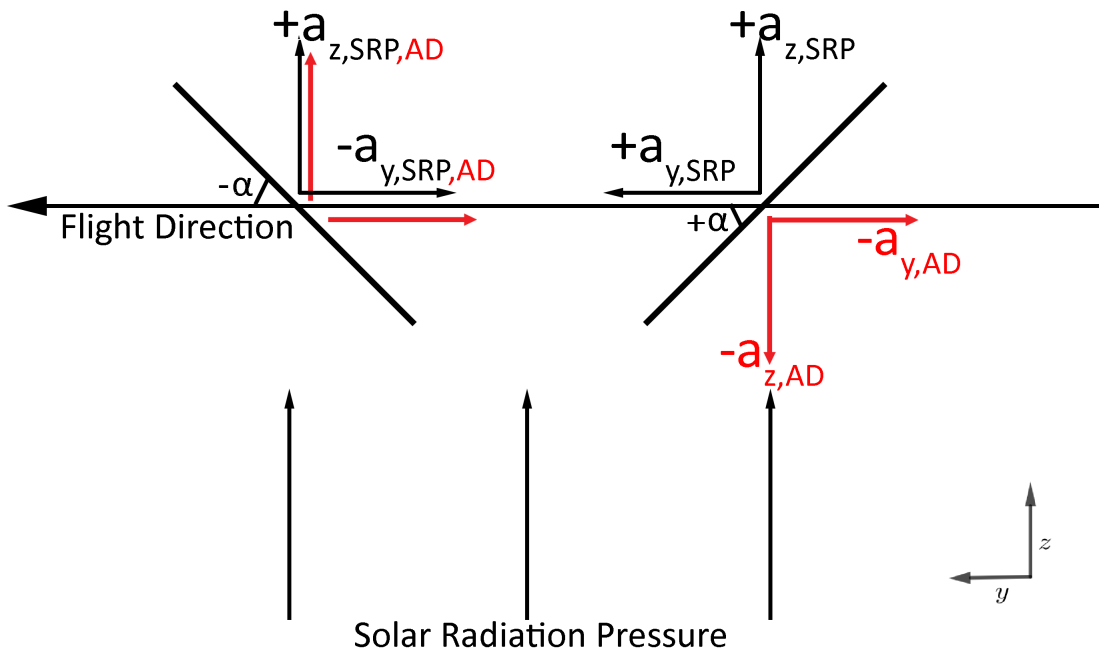

FIGURE 5.1: Femtosatellite force model

acceleration remains fixed, through changing the femtosatellite pitch angle from $-\alpha$ to $+\alpha$. This will form the basis of the orbit control strategy.

5.2.2.1 Solar Radiation Pressure

The effect of solar radiation pressure on each femtosatellite can be illustrated as shown in Figure 5.2. According to Equation (2.1), the acceleration generated by SRP depends on the SRP cross-section for a given satellite. The projected area of a femtosatellite of total surface area A along the Sun vector is given by

$$A_{SRP} = A\cos\alpha \tag{5.9}$$

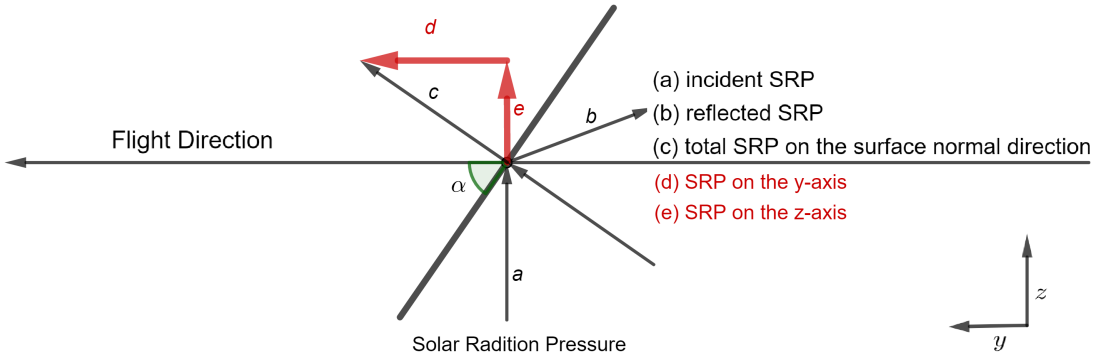

FIGURE 5.2: Force model - solar radiation pressure

Therefore, the total SRP acceleration applied in the femtosatellite surface normal direction becomes

$$a_{SRP} = \frac{2\eta PA}{m}\cos^2\alpha \tag{5.10}$$

The reflective efficiency, η, is incorporated to represent the non-perfect optical properties of the femtosatellite surface, although it is assumed the force is normal to the surface. The solar radiation pressure, P, is approximately $4.56 \times 10^{-6} Nm^{-2}$ in low Earth orbit (McInnes, 2004). The femtosatellite's mass and surface area are described by m and A. The femtosatellite's attitude angle in the xy-plane along the x-axis is again defined by α. When the acceleration generated by SRP is split along the y-axis and z-axis, this becomes

$$\begin{cases} a_{y,SRP} = \dfrac{2\eta PA}{m}\cos^2\alpha\sin\alpha \\ a_{z,SRP} = \dfrac{2\eta PA}{m}\cos^3\alpha \end{cases} \tag{5.11}$$

5.2.2.2 Atmospheric Drag

The other major perturbation that can influence the orbit evolution of the high area-to-mass ratio femtosatellite is atmospheric drag. For atmospheric drag, the projected area of a femtosatellite along the velocity vector is, A_{AD}, given by

$$A_{AD} = A|\sin\alpha| \tag{5.12}$$

The drag and lift forces on the femtosatellite (Sowter, 1989) are then given by

$$\begin{cases} F_{Drag} = -\frac{1}{2} c_D A_{AD} \rho v_{rel}^2 \\ F_{Lift} = -\frac{1}{2} c_L A_{AD} \rho v_{rel}^2 \end{cases} \tag{5.13}$$

where c_D is the drag coefficient, c_L is the lift coefficient, ρ is the atmospheric density (Vallado, 2013) and v_{vel} is the velocity of the femtosatellite relative to the atmosphere. In this chapter, the atmospheric density, ρ, is considered as constant across the entire mission orbit since only close proximity motion relative to the carrier spacecraft is considered. Assuming a Newtonian approximation with free molecular flow and specular reflection of molecules (Sowter, 1989), the drag and lift coefficients are:

$$\begin{cases} c_D = 2\sin^2\alpha \\ c_L = 2\sin\alpha\cos\alpha \end{cases} \tag{5.14}$$

so that, the aerodynamic forces in the y-axis and z-axis become

$$\begin{cases} a_{y,AD} = -\dfrac{A}{m}\rho v_{rel}^2 |\sin\alpha| \sin^2\alpha \\ a_{z,AD} = -\dfrac{A}{m}\rho v_{rel}^2 |\sin\alpha| \sin\alpha\cos\alpha \end{cases} \tag{5.15}$$

5.2.2.3 Carrier Spacecraft

In addition to the direct effect of solar radiation pressure and atmospheric drag on each femtosatellite, the differential acceleration between the femtosatellite and the carrier spacecraft in the relative coordinate system can be considered. As discussed in Section 2.6, the y-axis is aligned with the spacecraft velocity vector and z-axis is perpendicular to the orbit plane. For a mission that operates in a dawn/dusk SSO as described in Section 4.3.4, where the orbit plane is assumed normal to the incident sunlight, the carrier spacecraft is perturbed by the atmospheric drag in the y-axis and solar radiation pressure in the z-axis. The cross-section of the carrier spacecraft has been defined as $A_{carr,xz}$ for the y-axis and $A_{carr,xy}$ for the z-axis, with its mass m_{carr}. In the coordinate system defined in Figure 2.7, where the origin of the local frame of reference is at the carrier spacecraft, the effect of forces applied to the carrier spacecraft can be considered as

$$\begin{cases} a_{y,Carr} = -\dfrac{1}{2}\dfrac{c_D A_{carr,xz}}{m_{carr}}\rho v_{rel}^2 \\ a_{z,Carr} = \dfrac{2\eta P A_{carr,xy}}{m_{carr}} \end{cases} \tag{5.16}$$

5.2.2.4 Example Scenario

Figure 5.3 shows the ratio of $a_{y,AD}$ to $a_{y,SRP}$ at various altitudes when, for example, $\alpha = 12^{\circ}$ at which half of the maximum acceleration along the y-axis can be achieved according to Equation (5.11). Atmospheric drag using a non-exponential atmospheric model[3] (Vallado, 2013) is the dominant force along the y-axis at lower altitudes, while radar applications also favour lower altitudes to reduce the required transmit power and round-trip signal loss. Therefore, 700 km is chosen as the orbit altitude for investigation in this thesis as discussed earlier. The $a_{y,AD}$ is approximately 1% of $a_{y,SRP}$, therefore, can be ignored. At 700 km altitude, the atmospheric density ρ is $3.614 \times 10^{-14}\, kg/m^3$ (Vallado, 2013) and the relative speed v_{rel} is $7.5043\, km/s$. The femtosatellite used is assumed to be 0.02 kg with an area of 0.01 m^2, as discussed in Chapter 4.

A standard 3U CubeSat mass of 3 kg, cross-section 0.01 m^2 in the xz-plane and 0.03 m^2 in the xy-plane has been used as the carrier spacecraft and, again, femtosatellites of 0.02 kg mass and 0.01 m^2 surface area are considered, with the assumption that the carrier spacecraft will maintain a fixed attitude and has perfectly reflecting panels. The external forces as a function of femtosatellite orientation are shown in Figure 5.4 and 5.5. It can be seen that the forces acting on the carrier spacecraft are extremely small relative to the femtosatellite, due to the difference in their area-to-mass ratio.

It can be seen that the effect of atmospheric drag is small relative to solar radiation pressure at the mission orbit altitude of 700 km. This provides the basis for the femtosatellite to use solar radiation pressure for orbit control. Figure 5.4 shows that the total y-axis acceleration is minimised when $\alpha = 0$, which verifies the design goal in Chapter 4. For example, when $\alpha \in$

[3]The atmospheric density is not exponential above 100 km.

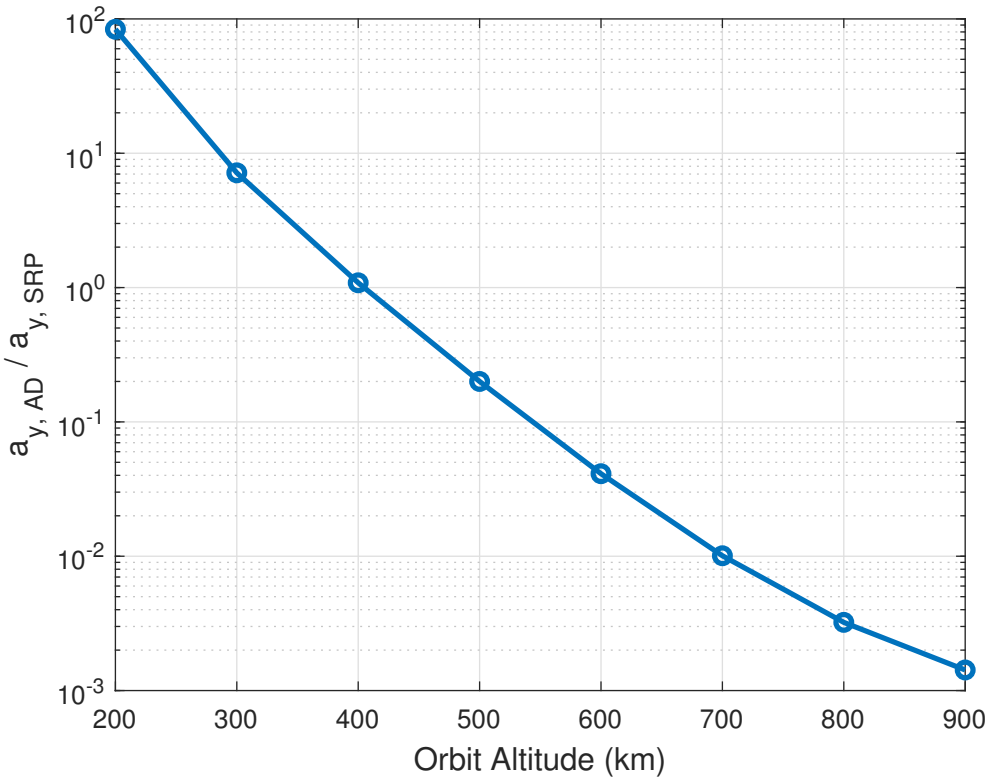

FIGURE 5.3: Ratio of $a_{y,AD}$ to $a_{y,SRP}$ at various altitudes when $\alpha = 12^\circ$

$(-12^\circ, 12^\circ)$, atmospheric drag is negligible where it contributes approximately 1% to the total acceleration along the y-axis. As a result of atmospheric drag, it can be seen that the maximum magnitude of a_y in the $+y$ and $-y$ directions is at $\alpha = 31^\circ$ and $\alpha = -41^\circ$ respectively. This will be the operating range of α for maximum manoeuvrability. Atmospheric drag will have a significant influence on long-term orbit evolution, therefore it is necessary to consider these forces when planning a long-term mission, and indeed the influence of these drag forces can be overcome by active orbit control. However, here the direct SRP acceleration dominates the dynamics of the relative motion of the femtosatellite and the carrier spacecraft, as will be used later in Section 5.4. Based on Equation (5.1c), the maximum range of motion in the z-axis due to solar radiation pressure is $z_{max} = 2\dfrac{a_z}{\omega_n^2}$ when $z_0 = 0$ and $\dot{z}_0 = 0$. For a 700 km altitude Earth

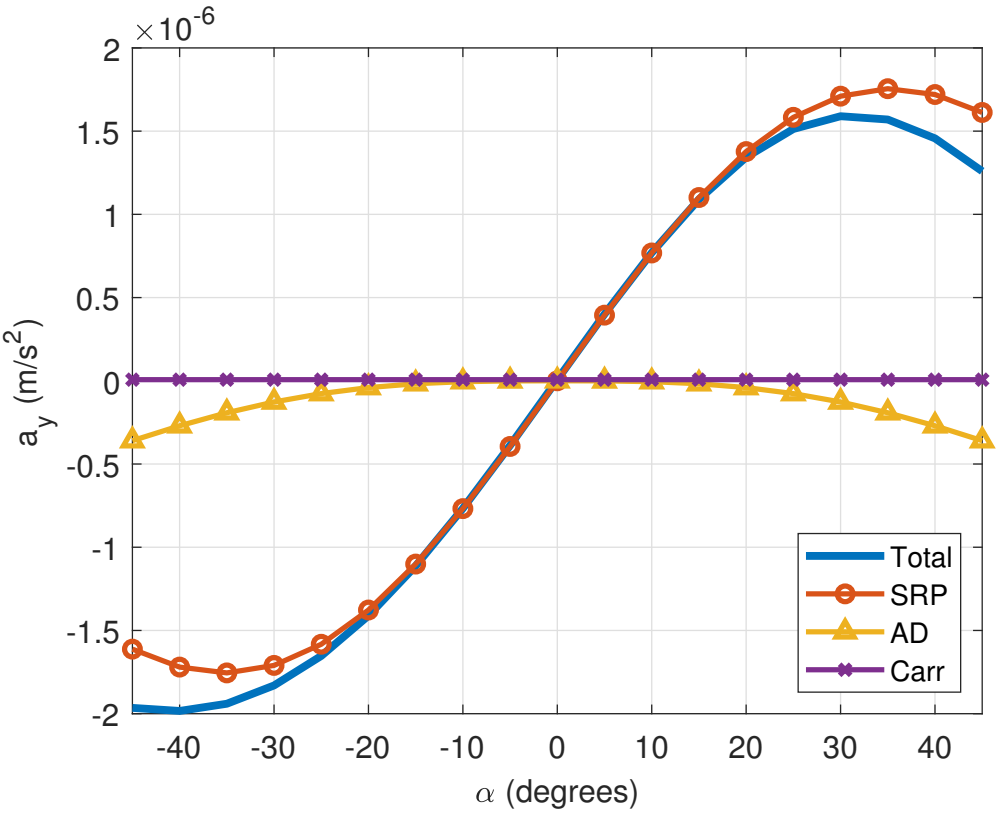

FIGURE 5.4: Effect of atmospheric drag and solar radiation pressure along the *y*-axis

orbit, the maximum range of motion is only 8 *m* with the assumption that the Earth is a perfect sphere with a radius of 6371 *km*. An in-plane control strategy can now be developed.

5.3 Orbit Control

As noted in Section 5.2, orbit control in this thesis will focus on motion along the *y*-axis. The foundation of the active orbit control strategy is the ability to control the attitude angle of the femtosatellite to modulate SRP.

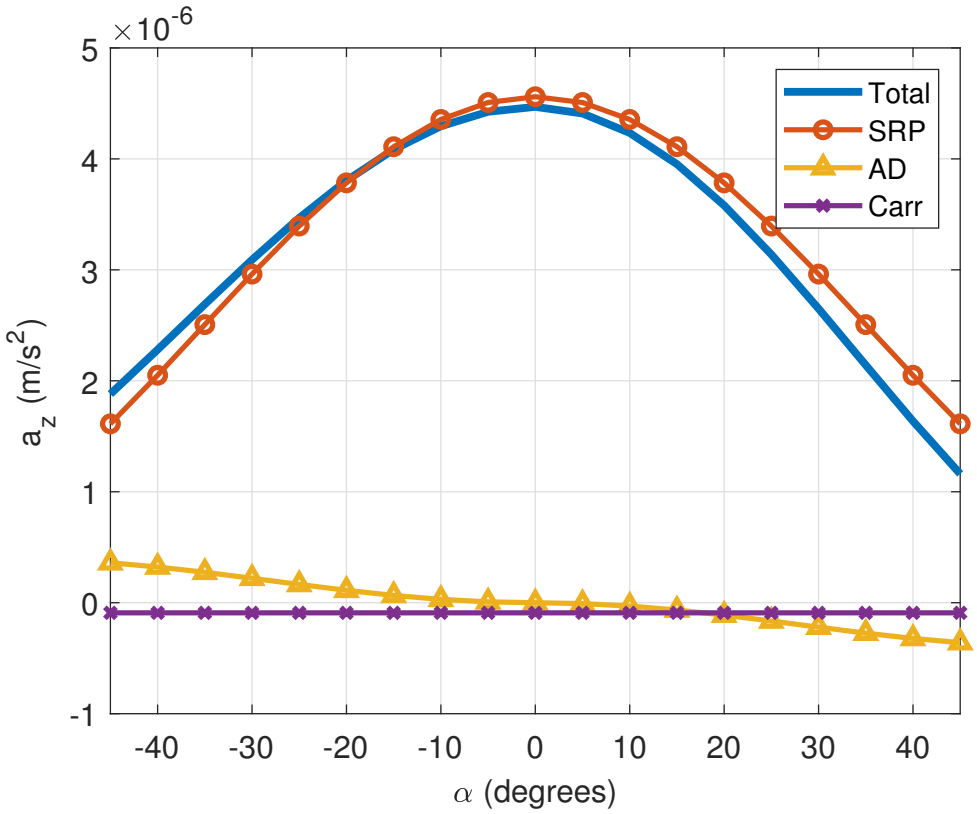

FIGURE 5.5: Effect of atmospheric drag and solar radiation pressure along the z-axis

5.3.1 Attitude Control

In order to explore the manoeuvrability of the femtosatellites for active position control, electrochromic panels are used, placed on each corner of the femtosatellites to control the solar radiation pressure by modulating the panel reflectivity. With the assumption that the centre-of-mass (CM) coincides with the geometric centre of the femtosatellite, a differential force ΔF_{SRP} can generate a torque τ, shown in Figure 5.6, to enable attitude control.

The dynamics of the femtosatellite with electrochromic panels introduced in Chapter 4 can be investigated as a function of orientation α and from the moment of inertia I as shown later in Equation (5.21). Here, L is the length of femtosatellite and A_{LCD} is the total surface area of

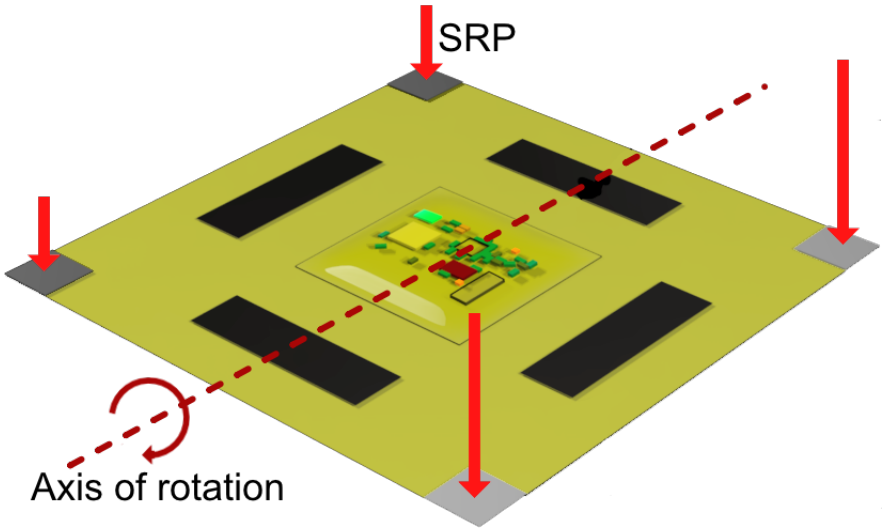

FIGURE 5.6: Torque generated by differential SRP

all electrochromic panels. The differential force ΔF_{SRP} in the direction of surface normal can be written as

$$\Delta F_{SRP} = 2\Delta_\eta P \frac{A_{LCD}}{2} \cos^2 \alpha \tag{5.17}$$

where Δ_η is the difference of reflective efficiency between the electrochromic panels. These will form the basis for active orbit control, so that for control torque τ

$$\tau = I\ddot{\alpha} \tag{5.18}$$

where

$$\tau = \Delta F_{SRP} \frac{1}{2} L \tag{5.19a}$$

$$I = \frac{1}{12} m L^2 \tag{5.19b}$$

therefore

$$\Delta F_{SRP} \frac{1}{2} L = \frac{1}{12} m L^2 \ddot{\alpha} \tag{5.20}$$

and finally, substituting ΔF_{SRP} using Equation (5.17) it can be seen that

$$2\Delta_\eta P \frac{A_{LCD}}{2} \cos^2 \alpha \, \frac{1}{2} L = \frac{1}{12} m L^2 \ddot{\alpha} \tag{5.21}$$

From Equation (5.21), a simplified dynamic model can be shown as follows

$$\ddot{\alpha} = \lambda \cos^2 \alpha \tag{5.22}$$

where

$$\lambda = \frac{6\Delta_\eta P A_{LCD}}{mL} \tag{5.23}$$

In order to represent the torque direction and magnitude that can be achieved by using electrochromic panels, a new torque coefficient parameter $k = [-1, 1]$ is added to Equation (5.22), so that

$$\ddot{\alpha} = k\lambda \cos^2 \alpha \tag{5.24}$$

From Equation (5.24) it can be seen that

$$\frac{\mathrm{d}\dot{\alpha}}{\mathrm{d}\, t} = k\lambda \cos^2 \alpha \tag{5.25}$$

so that

$$\frac{\mathrm{d}\alpha}{\mathrm{d}\, t} \frac{\mathrm{d}\dot{\alpha}}{\mathrm{d}\alpha} = k\lambda \cos^2 \alpha \tag{5.26}$$

and therefore

$$\dot{\alpha}\frac{\mathrm{d}\dot{\alpha}}{\mathrm{d}\alpha} = k\lambda\cos^2\alpha \tag{5.27}$$

Equation (5.27) can then be written as

$$\dot{\alpha}\mathrm{d}\dot{\alpha} = k\lambda\cos^2\alpha\mathrm{d}\alpha \tag{5.28}$$

and integrating on both sides

$$\int_{\dot{\alpha}_0}^{\dot{\alpha}} \dot{\alpha}\mathrm{d}\dot{\alpha} = \int_{\alpha_0}^{\alpha} k\lambda\cos^2\alpha\mathrm{d}\alpha \tag{5.29}$$

$$\frac{1}{2}\dot{\alpha}^2\Big|_{\dot{\alpha}_0}^{\dot{\alpha}} = \frac{1}{2}k\lambda\left(\frac{\sin 2\alpha}{2}+\alpha\right)\Big|_{\alpha_0}^{\alpha} + C \tag{5.30}$$

$$\dot{\alpha}^2 - {\dot{\alpha}_0}^2 = k\lambda\left(\frac{\sin 2\alpha}{2}+\alpha-\frac{\sin 2\alpha_0}{2}-\alpha_0\right)+C \tag{5.31}$$

Finally, when $\dot{\alpha} = \dot{\alpha}_0$ and $\alpha = \alpha_0$, $C = 0$, so that,

$$\dot{\alpha}^2 = k\lambda\left(\frac{\sin 2\alpha}{2}+\alpha-\frac{\sin 2\alpha_0}{2}-\alpha_0\right)+{\dot{\alpha}_0}^2 \tag{5.32}$$

The relation between α and $\dot{\alpha}$ can be established as shown in Equation (5.32), which can now be used to develop an attitude control strategy. A phase plane can then be created as shown in Figure 5.7. The vectors are calculated using Equation (5.24) and (5.32) to visualise the attitude behaviour under different conditions, where red lines illustrate an example attitude transition process. It shows that the torque direction can be reversed at any point by changing the reflectivity of the electrochromic panels. This is required to transit between different fixed

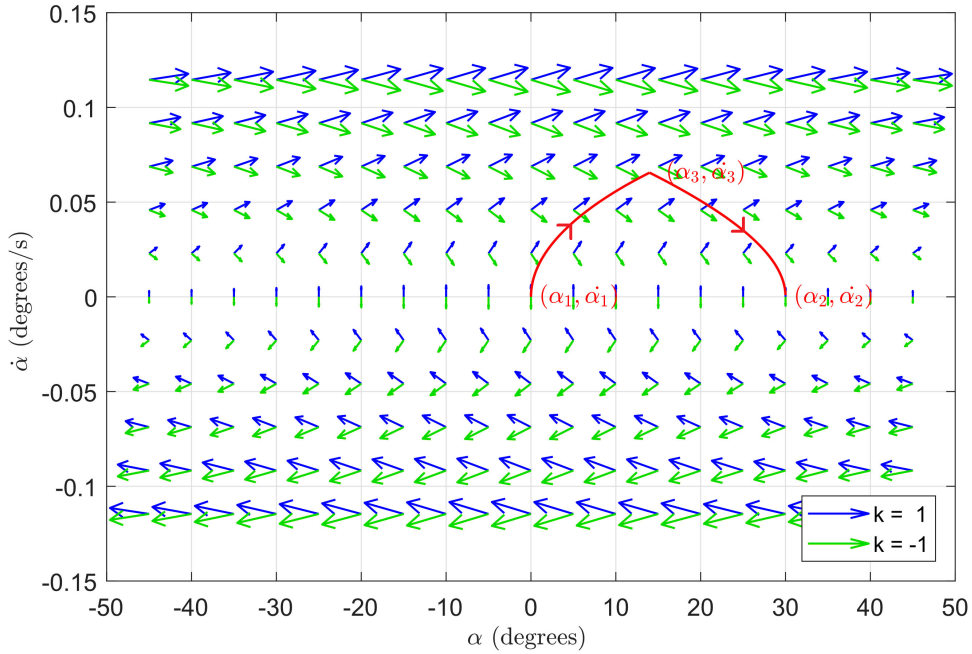

FIGURE 5.7: Angle transfer from the α_1 to the α_2 with phase plane

attitude angles.

5.3.2 Attitude Transition

When the femtosatellite is required to change its attitude angle from α_1 to α_2, and from rest-to-rest, as illustrated in Figure 5.7, the attitude transition process can be divided into two phases, when the magnitude of $\dot{\alpha}$ is increasing to start the rotation and decreasing to stop the rotation. The switch point between these two phases, $(\alpha_3, \dot{\alpha}_3)$, can be determined by substituting the initial condition $(\alpha_0, \dot{\alpha}_0)$ in Equation (5.32) with $(\alpha_1, \dot{\alpha}_1)$ and $(\alpha_2, \dot{\alpha}_2)$. With the appropriate torque coefficient, k, it is found that

$$\begin{cases} \dot{\alpha}_3 = \lambda\left(\dfrac{\sin 2\alpha_3}{2} + \alpha_3 - \dfrac{\sin 2\alpha_1}{2} - \alpha_1\right) + \dot{\alpha}_1{}^2 \\ \dot{\alpha}_3 = -\lambda\left(\dfrac{\sin 2\alpha_3}{2} + \alpha_3 - \dfrac{\sin 2\alpha_2}{2} - \alpha_2\right) + \dot{\alpha}_2{}^2 \end{cases} \tag{5.33}$$

so that

$$\frac{\sin 2\alpha_3}{2} + \alpha_3 = \frac{1}{2}\left(\frac{\sin 2\alpha_1}{2} + \alpha_1 + \frac{\sin 2\alpha_2}{2} + \alpha_2 + \frac{\dot{\alpha_2^2} - \dot{\alpha_1^2}}{\lambda}\right) \tag{5.34}$$

The switch point $(\alpha_3, \dot{\alpha_3})$ can then be found by solving Equation (5.24) and (5.34).

By integrating Equation (5.24) from the α_1 to α_3 and from the α_3 to α_2, the time required for each phase can be found as t_1 and t_2 respectively. The change in velocity, $\Delta v_y = \int a_y \mathrm{d}t$, during each phase, can then be found by integrating the angle transition over time, as will be discussed later in Section 5.3.3. This process is reversed when the attitude transfer is from α_2 to the α_1.

5.3.2.1 Example Scenario

For the femtosatellite prototype with 4 cm^2 total surface area for the electrochromic panels, as discussed in Chapter 4, Figure 5.8 shows the influence of the total electrochromic panel surface area on the transfer time between, for example, 0° and 12°, which indicates a logarithmic relation. A balance can be found between the electrochromic panel size and the femtosatellite manoeuvrability based on specific mission requirements.

In addition, Figure 5.9 demonstrates the time required to change between different attitude angles. In the extreme situation, from -45° to 45°, only 21 minutes is required to complete the manoeuvre. With the ability to control the attitude angle of a femtosatellite, and therefore to generate an acceleration along the y-axis, an active orbit control strategy can now be developed.

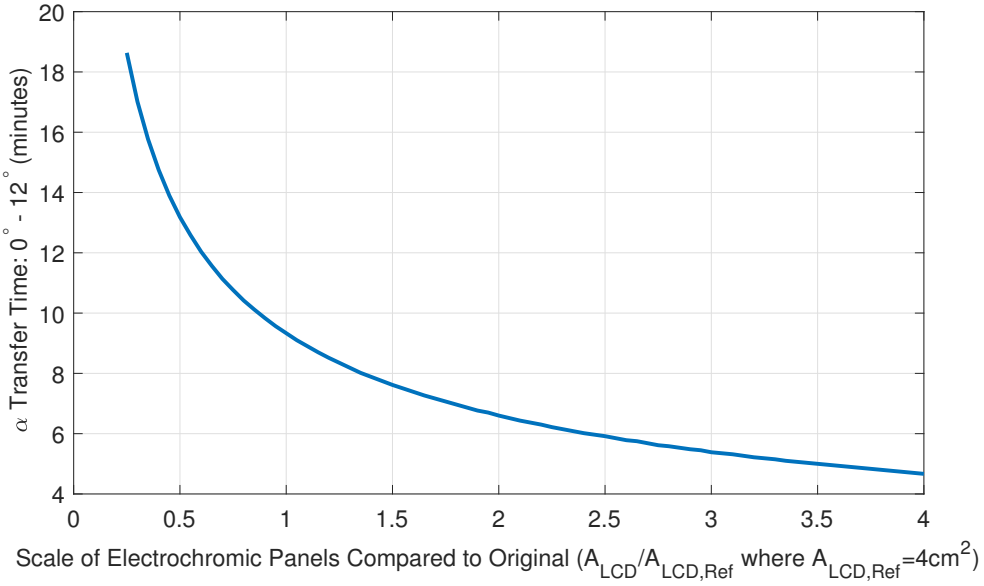

FIGURE 5.8: Electrochromic panel scaling

5.3.3 Active Orbit Control

A 'bang-bang' controller is defined to execute the active orbit control strategy. This is an open-loop controller to demonstrate the capability of using SRP acting on each femtosatellite for orbit control in various scenarios. The strategy is capable of controlling a femtosatellite to change its average speed along the *y*-axis. When the average speed is zero, the femtosatellite will be in periodic motion relative to the carrier spacecraft, therefore maintaining a relative stationary position.

Similar to the attitude transition discussed in Section 5.3.2, orbit control can also be divided into two stages; change the attitude angle of the femtosatellite to manoeuvrer and then recover the attitude angle back to zero. During both stages, the femtosatellite will generate an acceleration along the *y*-axis. A look-up table (LUT) is created to establish the relationship between the time required for each attitude transition state and the total change in velocity along

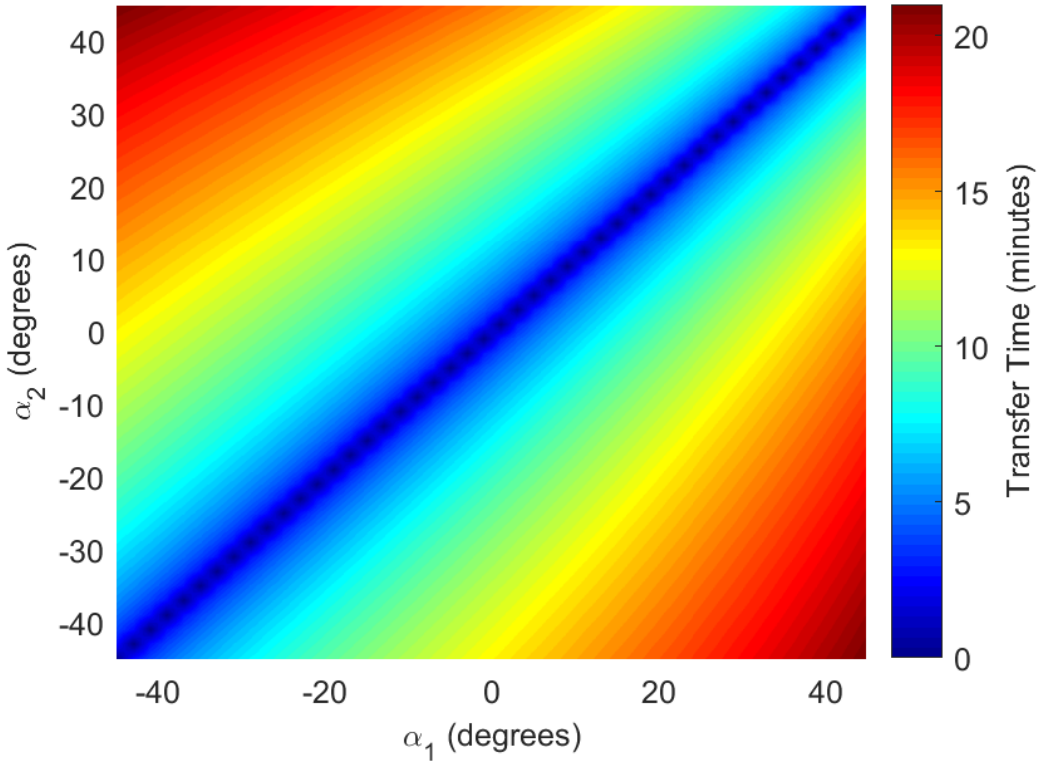

FIGURE 5.9: Attitude angle transfer time between the α_1 and the α_2

the y-axis, Δv_y, during such orbit control. The maximum total change in velocity is defined as $\Delta v_{y,max}$, when the femtosatellite's attitude angle reaches its limit of 35° in the first stage at maximum acceleration $a_{y,max}$ and so starts the second stage immediately. When the required Δv_y is higher than $\Delta v_{y,max}$, an extra stage will be added where the femtosatellite remains at its maximum acceleration to generate an additional change in velocity. The time required for such a stage can be defined as

$$t_3 = \frac{\Delta v_y - \Delta v_{y,max}}{a_{y,max}} \tag{5.35}$$

A flow chart to summarise the active orbit control strategy is shown in Figure 5.10.

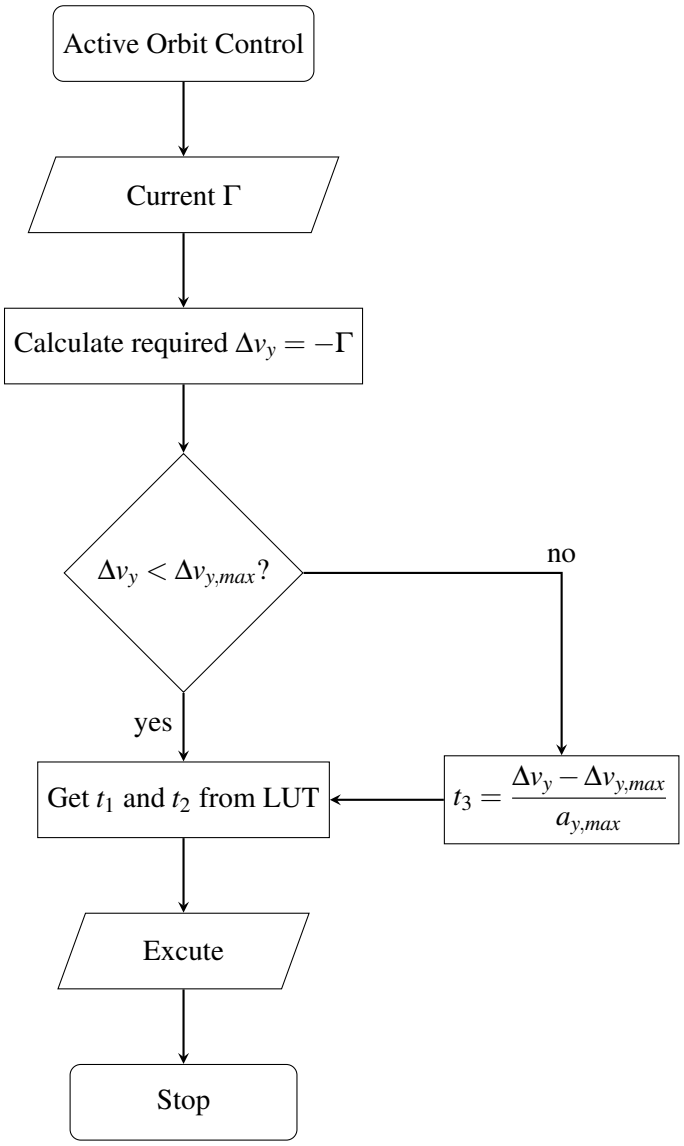

FIGURE 5.10: Active orbit control flow chart

5.4 Example Scenarios

Based on the orbital dynamics and control strategy discussed above, an example mission scenario is now investigated for demonstration. In this example, the orbit control will initiate once the distance of the femtosatellite along the y-axis reaches 100 m from the carrier spacecraft. Once reached, the femtosatellite will apply active orbit control to maintain the desired distance,

with $\dot{\tilde{y}} = 0$ as described in the Equation (5.7), before continuing the mission.

The dynamical model can be approximated through Equation (5.36) based on Equation (2.2), (5.11) and (5.24) , such that

$$\begin{cases} \ddot{x} - 2\omega_n \dot{y} - 3\omega_n^2 x = 0 \\ \ddot{y} + 2\omega_n \dot{x} = \dfrac{2\eta PA}{m} \cos^2\alpha \sin\alpha \\ \ddot{z} + \omega_n^2 z = \dfrac{2\eta PA}{m} \cos^3\alpha \\ \ddot{\alpha} = k\lambda \cos^2\alpha \end{cases} \tag{5.36}$$

The model couples the attitude control, the relative motion model and the femtosatellite force model together. In order to better demonstrate active orbit control, only solar radiation pressure on the femtosatellite has been considered in this section. The effect of atmospheric drag on the femtosatellite and the forces on the carrier spacecraft and are small relative to the solar radiation pressure acting on the femtosatellite, as demonstrated in Figure 5.4 and 5.5. AD varies due to solar cycles which have a period of 11 years (Hathaway, 2010). A lower AD could decrease the $a_{y,AD}$ to $a_{y,SRP}$ ratio, therefore, enable the femtosatellite to operate at lower altitude orbits and vice versa. Compared to conventional Earth remote sensing missions, femtosatellite will have a limited mission lifetime. The size of the electrochromic panels can be changed to satisfy the mission altitude requirement and AD variation due to solar cycles. With attitude control introduced in Section 5.3.1, a small perturbation can be corrected by modulating the electrochromic panels. A specialised release mechanism could be exploited as future work to minimise the tumbling at the initial release phase.

5.4.1 Low Initial Speed on Y-axis

The active orbit control strategy is utilised with a 'bang-bang' controller, achieved using the parameter k in Equation (5.36). The femtosatellite is ejected from the carrier spacecraft with an initial speed of 1 mm/s along the y-axis in the opposite direction to the carrier spacecraft orbital motion. Figure 5.11 shows the simulated result along the y-axis. A detailed demonstration of

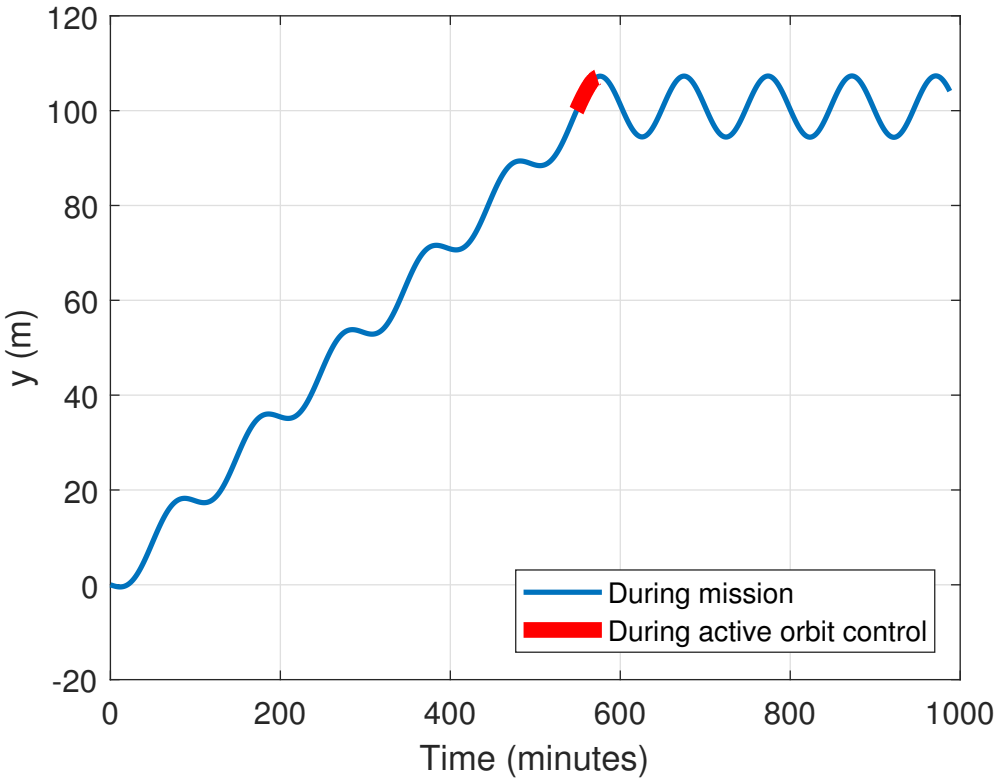

FIGURE 5.11: Femtosatellite's distance to the carrier spacecraft along the y-axis

the active orbit control strategy is shown as Figure 5.12.

Figure 5.12a represents the direction of the differential solar radiation pressure on the electrochromic panels. Figure 5.12b and 5.12c shows the femtosatellite attitude angular rate and

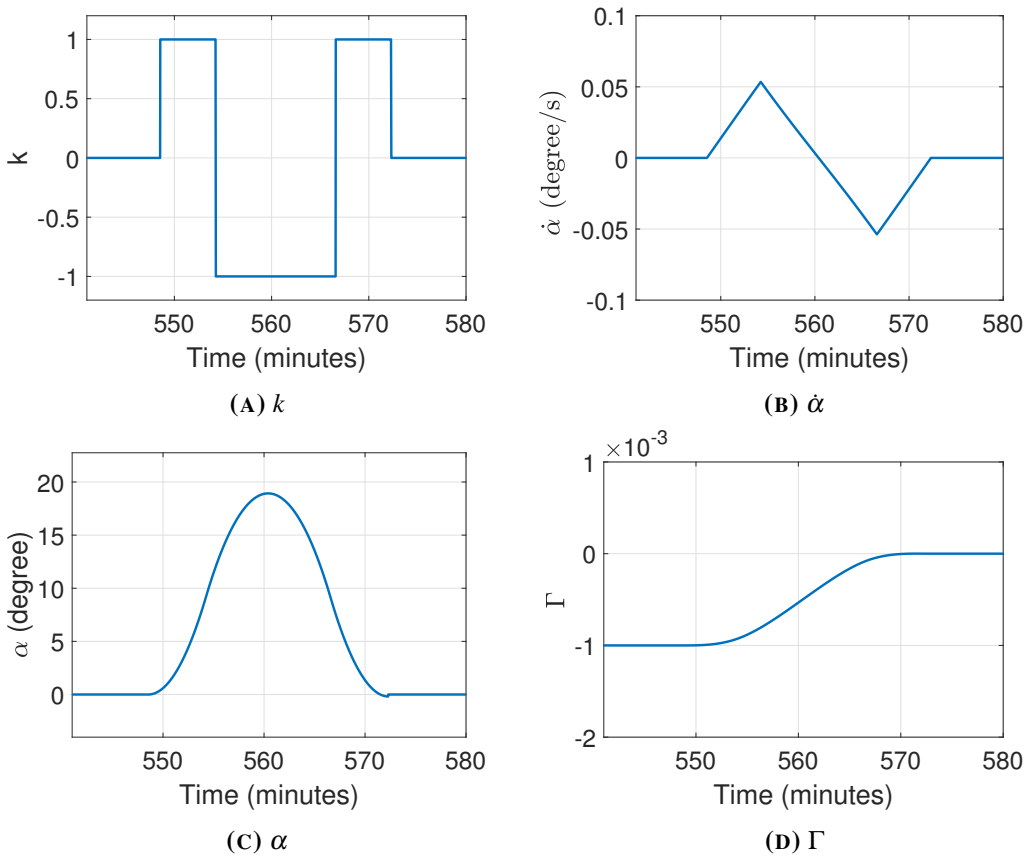

(A) k **(B)** $\dot{\alpha}$ **(C)** α **(D)** Γ

FIGURE 5.12: Active orbit control (time elapsed since release from carrier spacecraft)

angle during active orbit control as the result of differential solar radiation pressure on the electrochromic panels. These results show the acceleration and de-acceleration of the femtosatellite attitude angle α to reduce the speed along the y-axis. Γ is shown in Figure 5.12d, which shows the effect of the active orbit control on the drift of the femtosatellite orbit. After active orbit control, the femtosatellite enters periodic motion relative to the carrier spacecraft, as indicated by $\Gamma = 0$. For this mission, the duration of active orbit control is 23 minutes, which is equivalent to a quarter of the full orbit period. This demonstrates a smooth orbit transition from drift to periodic motion relative to the carrier spacecraft.

5.4.2 High Initial Speed on Y-axis

When the femtosatellite is ejected with a high initial speed, a different approach is required where an extra stage is add as discussed in Section 5.3.3. During such a stage, the femtosatellite will maintain its attitude angle to generate the additional velocity change Δv_y.

In this scenario, the femtosatellite is ejected from the carrier spacecraft with an initial speed of 5 mm/s along the y-axis in the opposite direction of the carrier spacecraft orbital motion. Figure 5.13 shows the simulated results. After active orbit control, the femtosatellite

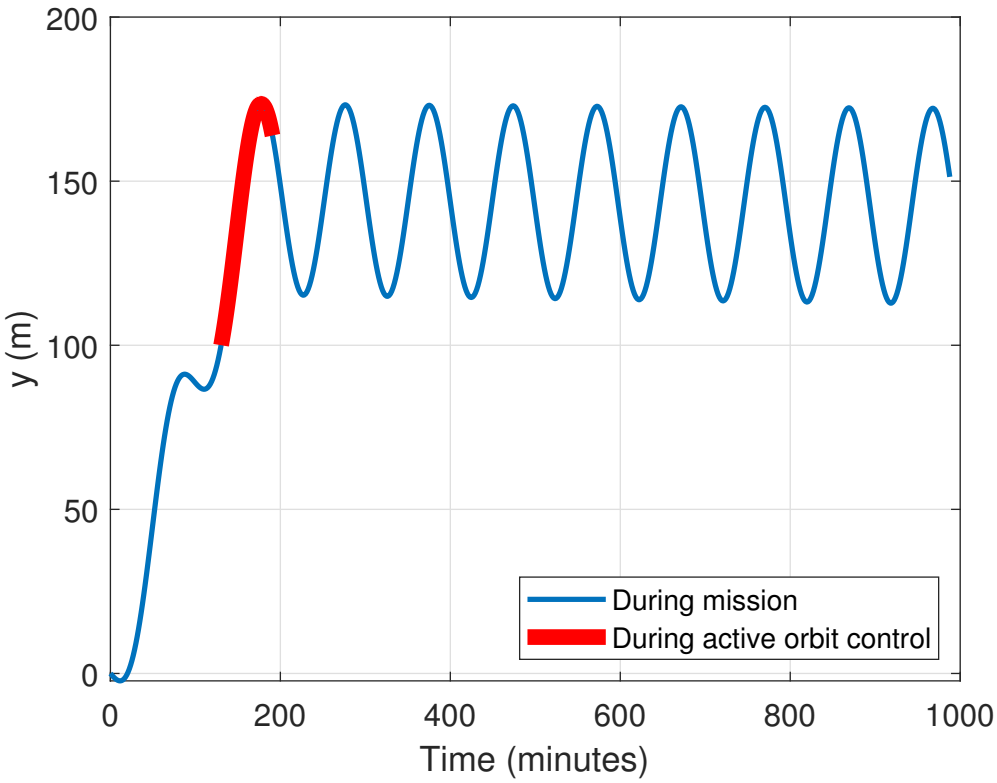

FIGURE 5.13: Femtosatellite's distance to the carrier spacecraft along the y-axis

is oscillating at a point 145 m from the carrier spacecraft along the y-axis. The active orbit control strategy can be triggered early to reduce the overshoot along the y-axis. A detailed

demonstration of the active orbit control is shown as Figure 5.14.

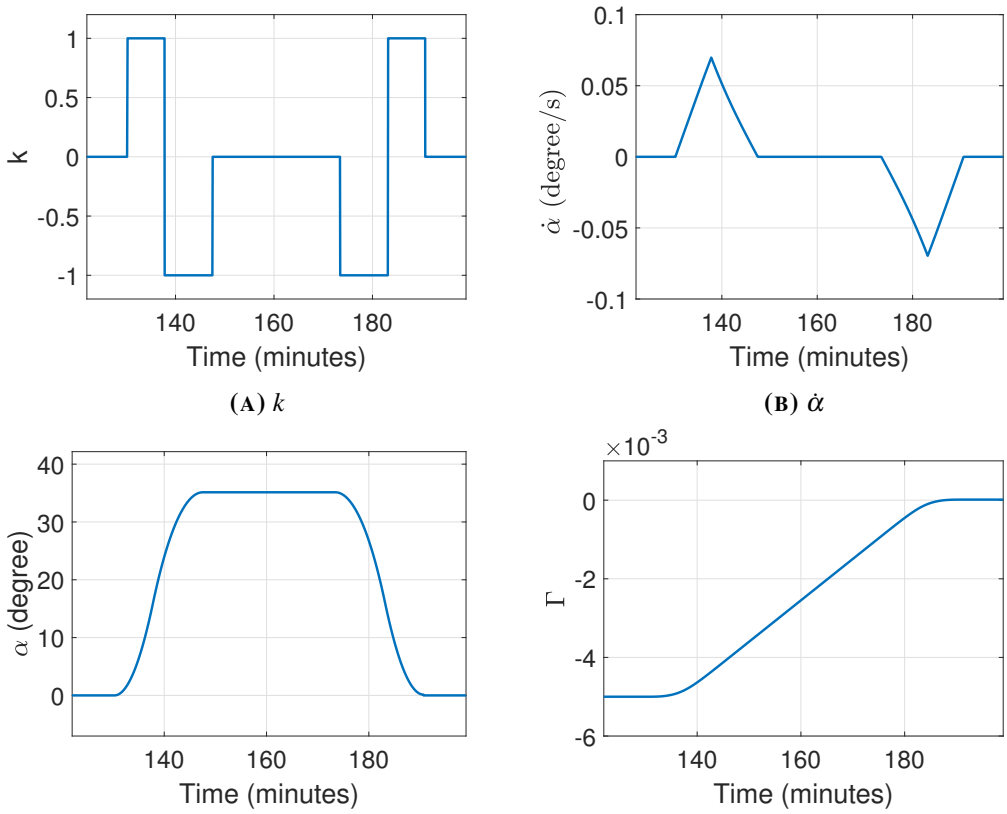

(A) k **(B)** $\dot{\alpha}$ **(C)** α **(D)** Γ

FIGURE 5.14: Active orbit control (time elapsed since release from carrier spacecraft)

Compared to Figure 5.12a, Figure 5.14a shows the stage where the femtosatellite maintains its attitude angle, also shown in Figure 5.14b and 5.14c. In addition, Figure 5.14a and 5.14b shows the impact of a larger attitude angle, where the available torque is lower as described in Equation (5.17) and (5.19a). Releasing the femtosatellites at high initial speed will introduce greater challenges for orbit control. As shown in Figure 5.14c and 5.14d, the rate of change of Γ is directly related to the femtosatellite attitude angle. These examples demonstrate the feasibility of using solar radiation pressure for femtosatellite active orbit control with different speeds along the y-axis, when neglecting atmospheric drag perturbations.

5.4.3 High Initial Speed on Y-axis with Tumbling

Tumbling could happen when the femtosatellite is ejected with a high initial speed. A simple detumbling strategy based on attitude control from Section 5.3.1 is applied after release without consideration on the effect of orbit control.

As in Section 5.4.3, the femtosatellite is ejected from the carrier spacecraft with an initial speed of 5 mm/s along the y-axis in the opposite direction of the carrier spacecraft orbital motion and an angular speed of 0.05 $^\circ/s$ around the x-axis clockwise direction. Figure 5.15 shows the simulated results. It is similar to the scenario without tumbling shown in Figure

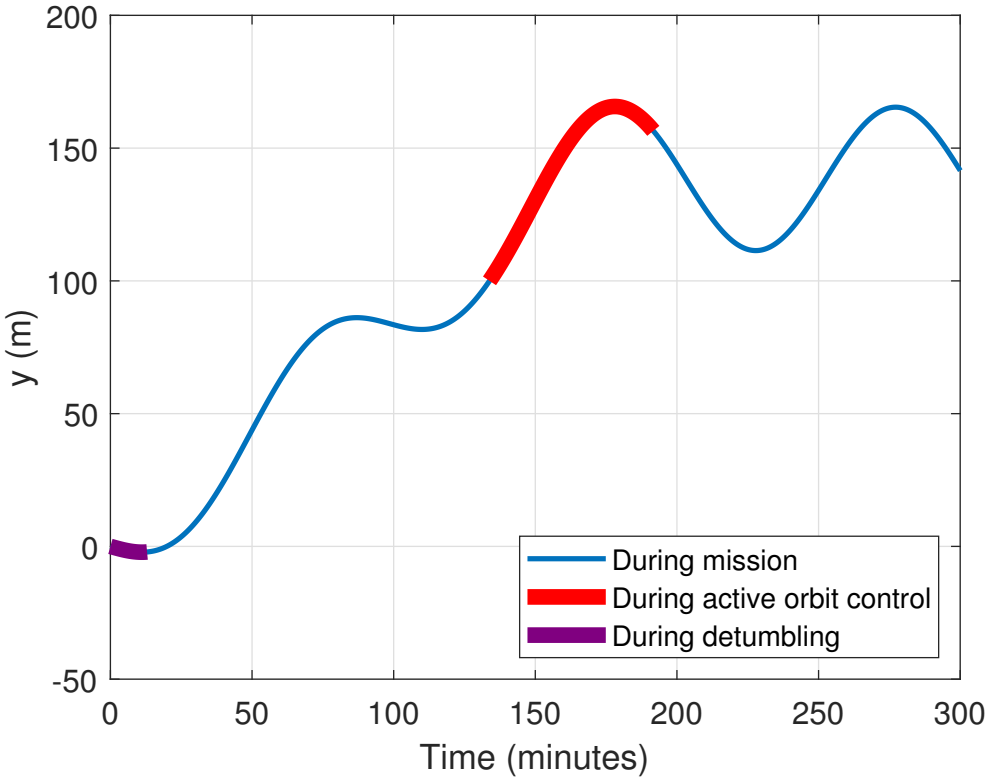

FIGURE 5.15: Femtosatellite's distance to the carrier spacecraft along the y-axis

5.13. The orbit trajectory is merely affected by the small initial attitude angle. A detailed

demonstration of the active orbit control is shown as Figure 5.16.

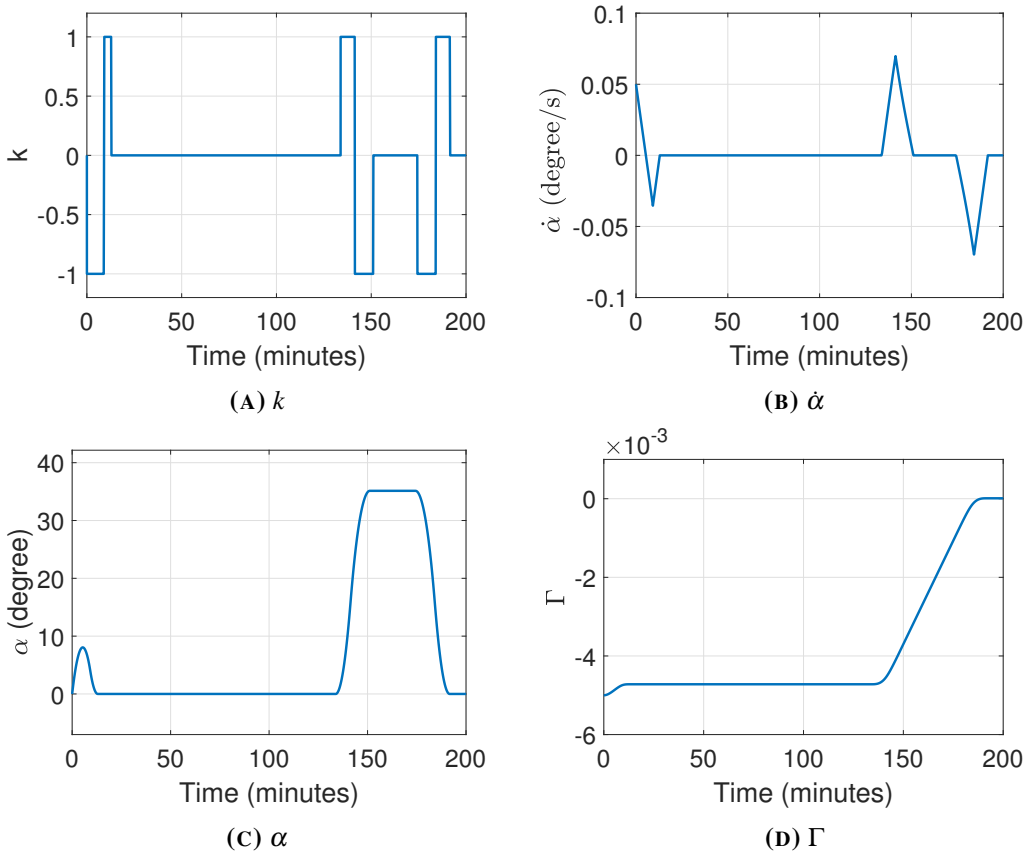

(A) k **(B)** $\dot{\alpha}$ **(C)** α **(D)** Γ

FIGURE 5.16: Active orbit control (time elapsed since release from carrier spacecraft)

Figure 5.16a represents the direction of the differential SRP on the electrochromic panels during the attitude control and the active orbit control. Figure 5.16b and 5.16c demonstrate the changes of attitude angle and rate during such a process. The initial detumbling requires 13 minutes. Γ is shown in Figure 5.16d. It can be seen that the mean speed is changed as the result of the detumbling process and the active control is not affected. This example demonstrates that a small perturbation during release could be corrected by using simple attitude control. However, it cannot be used with high initial attitude rates which result in the attitude exceeding 90°

during the detumbling process. The larger angular rate scenario requires a more comprehensive detumbling strategy.

5.4.4 Femtosatellite Swarm Deployment

By applying simple active orbit control on each femtosatellite, a swarm of femtosatellites can be manoeuvred away from the carrier spacecraft in a controlled manner to form a large sparse antenna for the Earth remote sensing radar application, as illustrated in Figure 5.17 and 5.18. In this example, the femtosatellite swarm will form a linear array on each side of the carrier spacecraft along the y-axis. Two femtosatellites are released from the carrier spacecraft every 5 seconds, with an initial speed of 1 mm/s in opposing directions along the y-axis. In total, 100 femtosatellites will be released and controlled individually to form a formation approximately 20 m away from the carrier spacecraft and spread 100 m long in both direction of the y-axis.

Figure 5.17a and 5.18a shows that all femtosatellites have been released from the carrier spacecraft and are free-flying before initiating active orbit control. In Figure 5.17b, the femtosatellites start to reach their desired distance and apply active orbit control to maintain their desired distance. From Figure 5.17c, the femtosatellites start to group within the swarm, this is due to the oscillation in the y-axis as shown in Figure 5.11. Figure 5.18 illustrates the motion along the z-axis during the deployment. Detailed results on the swarm evolution are provided in Appendix B.

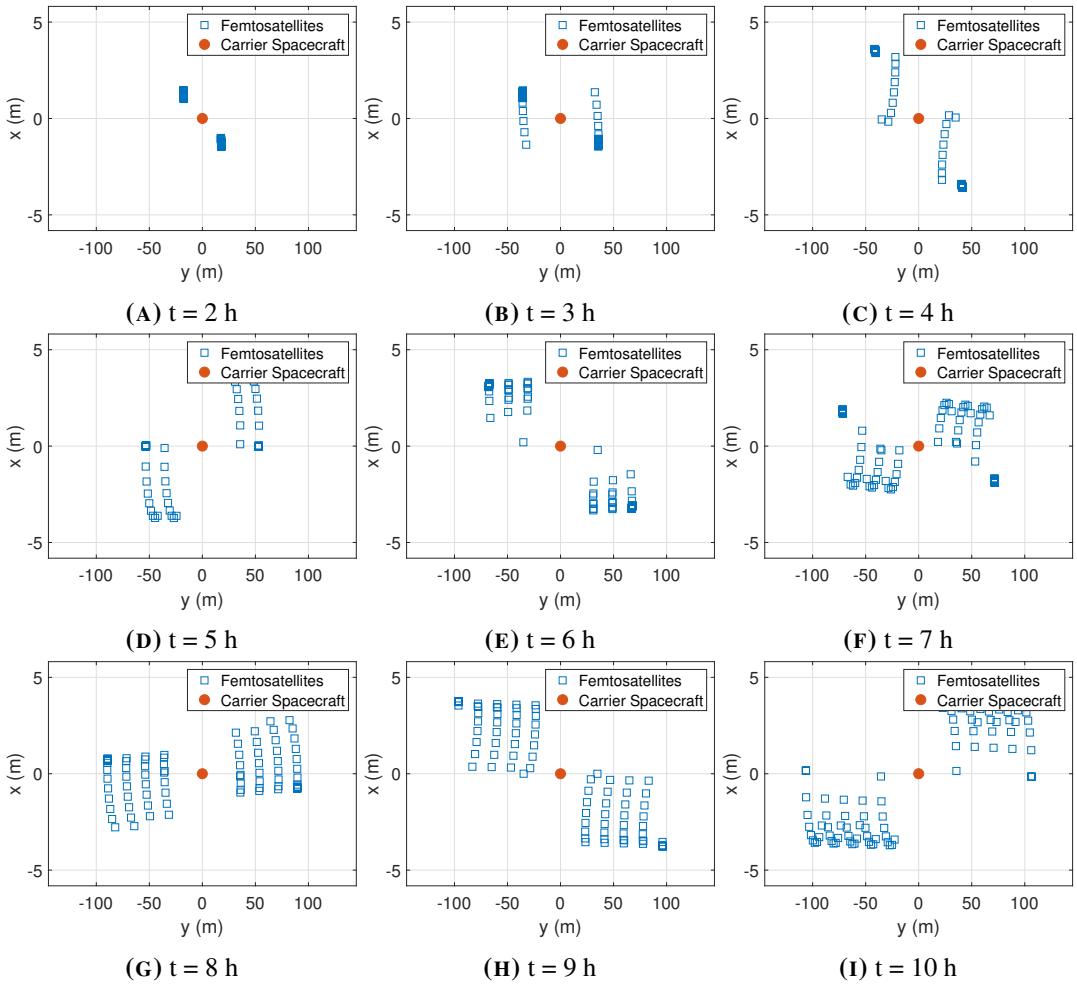

(A) t = 2 h **(B)** t = 3 h **(C)** t = 4 h

(D) t = 5 h **(E)** t = 6 h **(F)** t = 7 h

(G) t = 8 h **(H)** t = 9 h **(I)** t = 10 h

FIGURE 5.17: Deployed femtosatellites over time, *xy*-plane

5.5 Summary

In this chapter, the dynamics of femtosatellites have been investigated and exploited, with the assumptions used listed. The force analysis in Section 5.2 details the effect of solar radiation pressure for the femtosatellite concept proposed in Chapter 4. Results of this analysis are provided to demonstrate the feasibility of using solar radiation pressure for orbit control of the femtosatellites. In Section 5.3, the attitude control model was introduced and the attitude transition process has been discussed. An active orbit control strategy was also proposed in Section

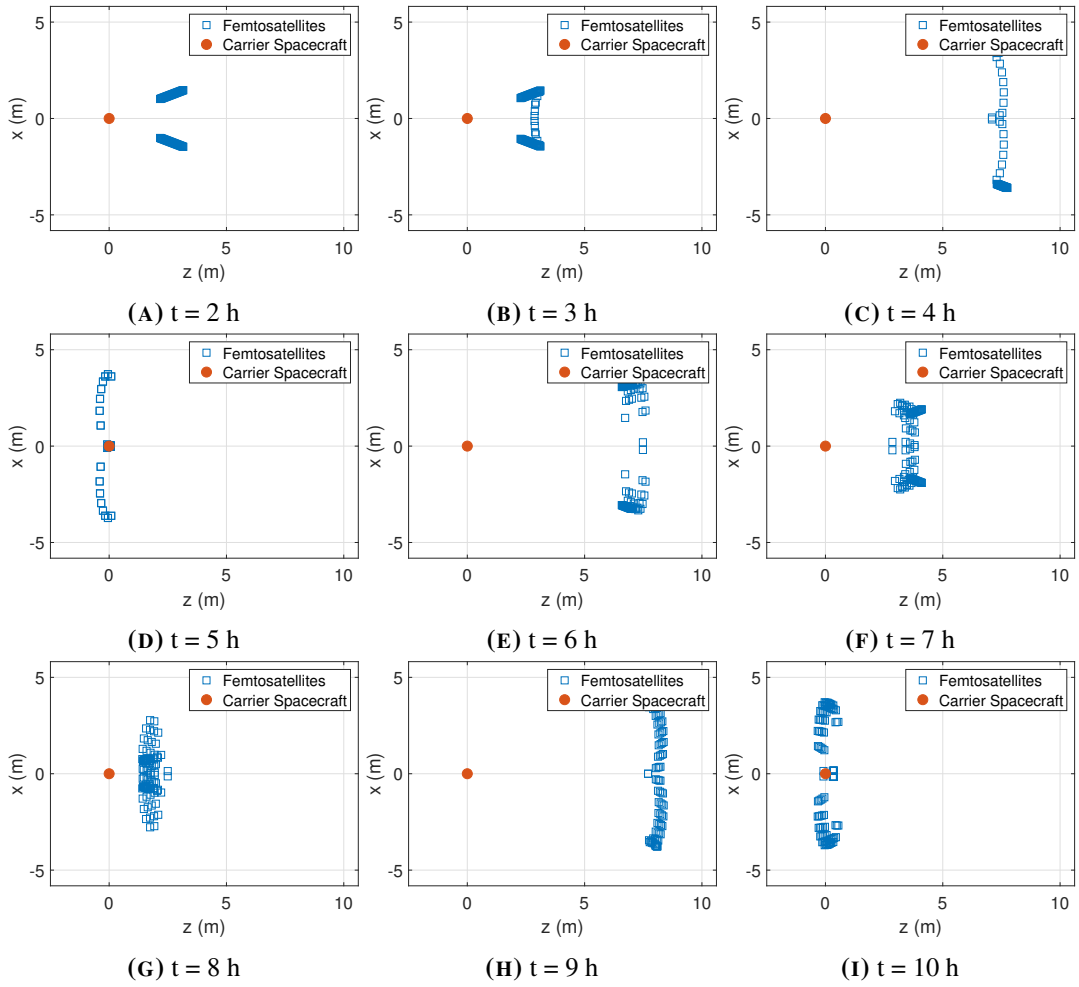

(A) t = 2 h **(B)** t = 3 h **(C)** t = 4 h

(D) t = 5 h **(E)** t = 6 h **(F)** t = 7 h

(G) t = 8 h **(H)** t = 9 h **(I)** t = 10 h

FIGURE 5.18: Deployed femtosatellites over time, *xz*-plane

5.3.3 to investigate the feasibility of orbit control. In Section 5.4, an example mission scenario was used to demonstration the active orbit control strategy under different initial release speeds. Finally, an example of femtosatellite swarm deployment was provided to further demonstrate the capability of the active orbit control strategy for the femosatellite radar application.

Chapter 6

Femtosatellite Radar Applications

6.1 Introduction

The femtosatellite swarm performance will now be evaluated in this chapter. As noted in Chapter 4, the SAR application will be used for system evaluation in this thesis. Section 6.2 introduces a modified range-Doppler algorithm (RDA) for a femtosatellite swarm using SAR signal processing. It is used to process the simulated radar data and to evaluate the capability of the femtosatellite swarm. The performance of the femtosatellite swarm is then analysed in Section 6.3, including the orbit and radar application specifications. The radar specification is similar to the TerraSAR-X mission in Section 3.4. In Section 6.4, a mock mission scenario is provided to further evaluate the femtosatellite swarm SAR system. The swarm performance is then characterised for 3 different configurations: the number of the femtosatellites, received signal SNR and positioning error. In addition to Earth remote sensing, Section 6.5 will demonstrate that the same femtosatellite swarm configuration can also be used for space situational awareness.

6.1.1 Assumptions

As noted in 3.3.2, a bi-static radar system can be considered as pseudo mono-static when the bi-static angle is close to 0°. In this chapter, the received signal is simulated at a position the same as the carrier spacecraft. No reference channel is not included in the simulation and the local oscillator is assumed synchronised across each femtosatellite. A commercial GPS chip is assumed to be used for positioning, although in principle computer vision at the carrier spacecraft could be used to enhance the femtosatellite relative positioning. The positioning error is simulated by shifting the raw SAR data in the azimuth and range direction separately.

The original code was created by Schlutz (Schlutz, 2009). Changes which have been made for this research include: different targets; geometries for ground and on-orbit targets; bi-static configuration; multiple receivers; inclusion of different noise / errors; modified RDA and radar image characterisation. The target is modelled as a binary occupancy map for simulation.

6.2 Modified RDA

Motion along the x-axis and z-axis in the local orbit frame will introduce challenges for radar signal processing due to focusing problems, requiring algorithms such as a non-linear chirp scaling methods to achieve finer focusing (Wong et al., 2008). Both mono-static and bi-static configurations have been investigated for small satellite platforms (Engelen et al., 2012; Pang et al., 2015). Due to the limitations of femtosatellites, one single femtosatellite is not powerful enough to be used in the mono-static configuration. Therefore, for bi-static configurations, the received signal will be described by Equation (6.1). The range of the target to the transmitter

and the target to the receiver are represented by R_{tx} and R_{rx} respectively, such that

$$s_{rx}(t,\tau) = \sum_{k=0}^{K-1} \left[F_k w_a(\tau - \tau_c) w_r \left(t - \frac{R_{tx}(\tau,k) + R_{rx}(\tau,k)}{c} \right) \right.$$
$$\left. \exp\left(-j2\pi f_o \left(\frac{R_{tx}(\tau,k) + R_{rx}(\tau,k)}{c} \right) + j\pi K_r \left(t - \frac{R_{tx}(\tau,k) + R_{rx}(\tau,k)}{c} \right)^2 \right) \right]$$
$$+ n(t,\tau) \tag{6.1}$$

Krieger and Moreira have noted that the spatial separation has to be 'a significant fraction' of R_{tx} or R_{rx} (Krieger and Moreira, 2006). In order to avoid the error introduced from bi-static radar algorithms and reduce the computation time from back projection (Yegulalp, 1999; Albuquerque et al., 2008), a modified mono-static range-Doppler algorithm (RDA) has been developed for the femtosatellite swarm case study in this thesis.

Introduced in Section 3.3.3, the RDA is a common algorithm for SAR signal processing. It converts a continuous SAR signal space to an image (Cumming et al., 2005). A block diagram of the modified RDA is shown in Figure 6.1. All received signals will be processed individually at the beginning via the standard RDA introduced in Chapter 3.3.3. The first step is range compression, which converts the long transmitted pulse width to a short high resolution pulse width in the range direction. Each azimuth bin is processed by a fast Fourier transform (FFT), matched filter and inverse fast Fourier transform (IFFT). Similarly, the result will be compressed in the azimuth direction. This process starts by applying azimuth FFT to each range bin to generate the range-Doppler domain. Then, the converted range-Doppler domain is processed by the range cell migration correction (RCMC) to flatten the hyperbolic range contour before matched filtering. All individually processed signals are shifted based on the relative distance in the flight direction and the radar signal round trip distance differences,

compared to the carrier spacecraft before data fusion. Data fusion is the process in which the signals are superimposed together coherently. This is a similar process to multi-look SAR (Melvin et al., 2012), however, by using data from each femtosatellite, the speckle on the final image can be reduced without reducing the resolution. Finally, the azimuth IFFT is applied to generate the final image.

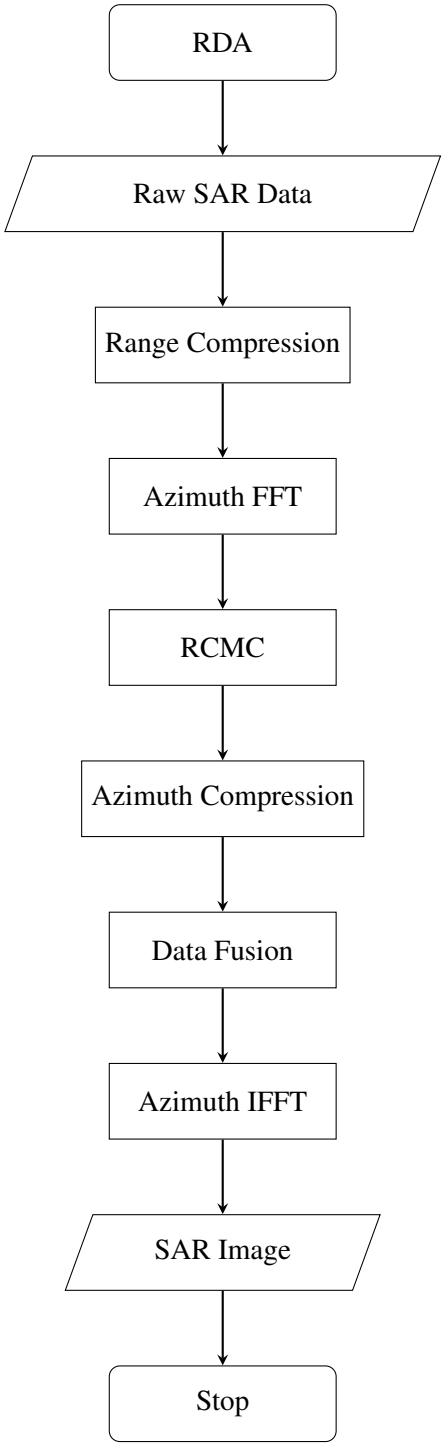

FIGURE 6.1: Block diagram of modified range-Doppler algorithm

6.3 Performance Analysis

The theoretical performance of a SAR system can be evaluated by using the noise equivalent sigma zero (NESZ) and signal-to-noise ratio (SNR), which can be expressed as (Wang et al., 2018):

$$SNR = \frac{\sigma_0}{NESZ} \tag{6.2}$$

where σ_0 is the backscattering coefficient and

$$NESZ = \frac{4 \cdot (4\pi)^3 \cdot R^3 \cdot V_s \cdot \sin\psi \cdot \sigma \cdot T_0 \cdot NF \cdot B_0 \cdot L_{tot}}{\lambda^3 \cdot c \cdot G_t \cdot G_r \cdot \tau \cdot P_t \cdot PRF} \tag{6.3}$$

where R is the range from the radar to the target, V_s is the velocity of the radar, ψ is the incident angle between the incidence radar beam and the target surface normal, σ is the Stefan-Boltzmann constant, T_0 is the receiver temperature, NF is the noise figure of the receiver, B_0 is the bandwidth, L_{tot} is the system loss, λ is the wavelength, G_t is the transmit antenna gain, G_r is the receive antenna gain, τ is the transmitting pulse width, P_t is the transmit power and PRF is the pulse repetition frequency.

For the femtosatellite SAR swarm, the number of the femtosatellites, n, is considered and the NESZ of can be expressed as:

$$NESZ_{swarm} = NESZ \cdot \sqrt{n} \tag{6.4}$$

In order to evaluate the performance of the bi-static femtosatellite swarm, an example scenario of a common X-band SAR system has been investigated for demonstration. The carrier spacecraft is orbiting at 700 *km* altitude. It is assumed that the orbit is circular with an orbital

speed of 7.50 km/s. The radar pulse repetition frequency is 3000 Hz and lasts for a duration of 0.5 s. The swath range, which is the distance between the carrier spacecraft nadir track and the target, is 400 km. The size of the Vivaldi antenna is approximately 14.5×37 mm (Mandeville et al., 2009). The main SAR parameters are listed in Table 6.1.

TABLE 6.1: SAR system parameters

Parameter	Value
Carrier frequency	9.65 GHz
Bandwidth	100 MHz
Pulse repeat frequency	3000 Hz
Duration	0.5 s
Chirp pulse duration	10 μs
Orbit altitude	700 km
Swath range	400 km
Velocity	7.50 km/s
Approximate range resolution	1.5 m
Receiver temperature	280 K
Noise figure	7 dB
System loss	-3 dB
Transmit antenna gain	30 dB
Receive antenna gain	10 dB
Transmitting pulse width	10 s
Transmit power	100 W

The NESZ and SNR of the femtosatellite swarm are shown in Figure 6.2 and 6.3. Most spaceborne SAR systems features a NESZ between -20 dB to -30 dB (Meng et al., 2017).

Therefore, a swarm of 50 femtosatellites is required to provide a competitive performance to a conventional spaceborne SAR system.

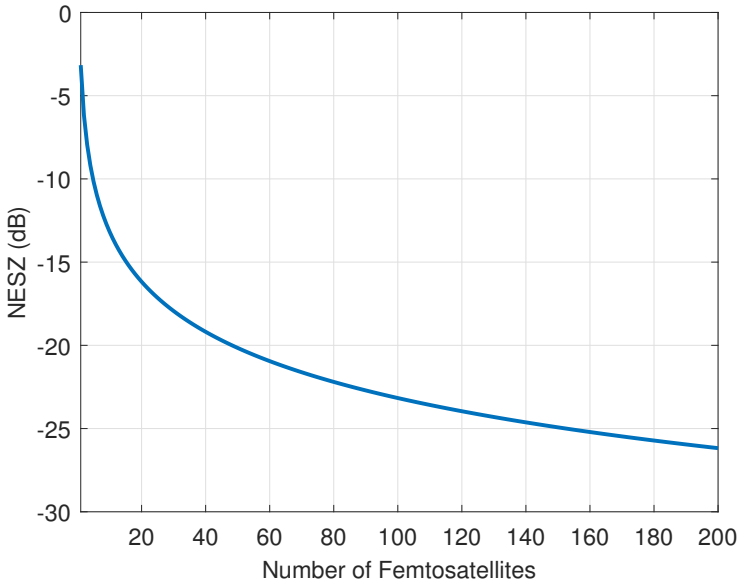

FIGURE 6.2: NESZ for femtosatellite swarm

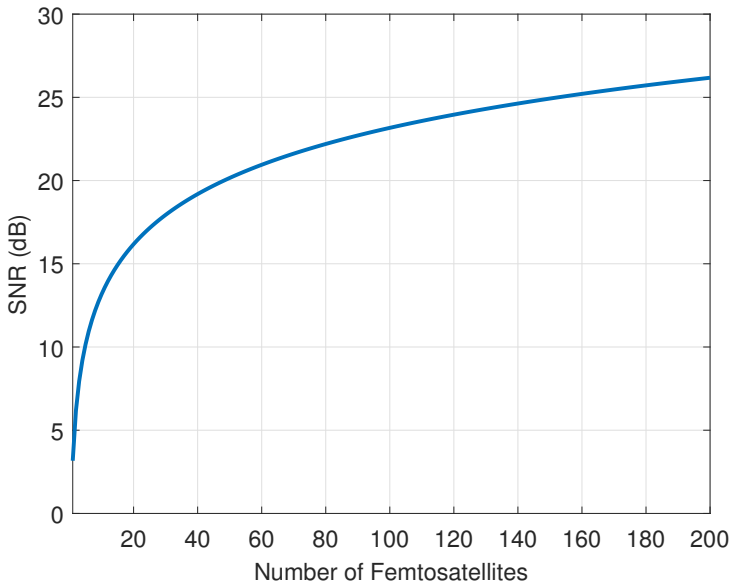

FIGURE 6.3: SNR for femtosatellite swarm

6.4 Performance Evaluation

An Airbus A380 airliner is used as the target, which is shown in Figure 6.4. It has a wingspan of 80 m and length of 73 m (Leung et al., 2007). The SAR signal space is calculated by using Equation (3.3) and processed by the modified range-Doppler algorithm to produce the final images (Cumming et al., 2005). The position offsets between the carrier spacecraft and femtosatellites are corrected based on their position. Figure 6.5 is generated by using the SAR signal space without noise and positioning errors. It is used as a benchmark to compare the performance under different conditions. The performance will be characterised based on the image peak SNR compared to the benchmark, as shown in Figure 6.5. The image peak SNR is calculated by Equation (6.5), such that

$$\text{image peak SNR} = 10\log_{10}\frac{1}{MSE} \tag{6.5}$$

where MSE is the mean square error between the final radar image and the reference image.

FIGURE 6.4: Example airliner (Airbus A380)

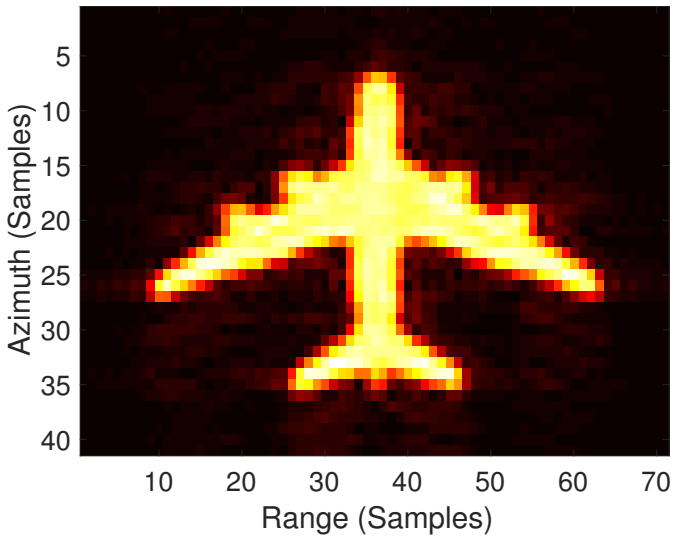

FIGURE 6.5: SAR image benchmark

6.4.1 Test 1: Number of Femtosatellites

Figure 6.6 shows images produced from different numbers of femtosatellites with -50 *dB* SNR. With only one femtosatellite, the airliner is invisible in Figure 6.6a. When there are up to 20 femtosatellites, the airliner starts to appear in the images, as in Figure 6.6b. The more femtosatellites, the less noisy an image can be produced.

Due to the nature of the data fusion method used in the modified RDA, the image quality is proportional to the square root of the number of femtosatellites, as shown in Figure 6.7. This matches the result in Figure 6.3. The image SNR will reach noise saturation as the low raw signal SNR results in loss of sensitivity. This test uses Gaussian white noise as an example for demonstration under optimistic conditions and applied to the entire raw SAR data from each femtosatellite. In reality, the sources of noise are more complicated and powerful noise may have other influences on the final radar image, therefore, further research is required.

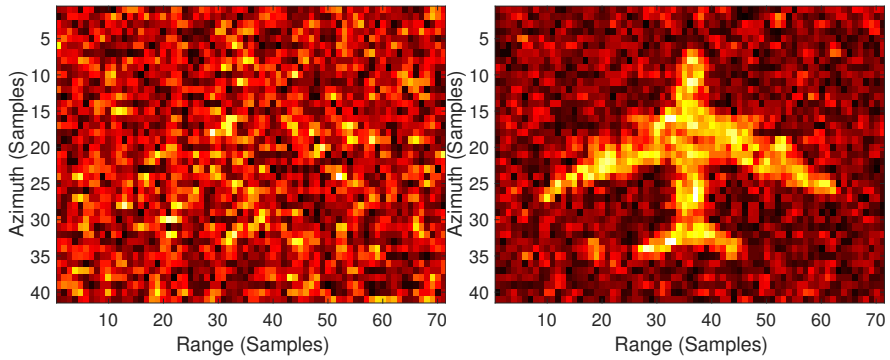

(A) 1 **(B)** 20

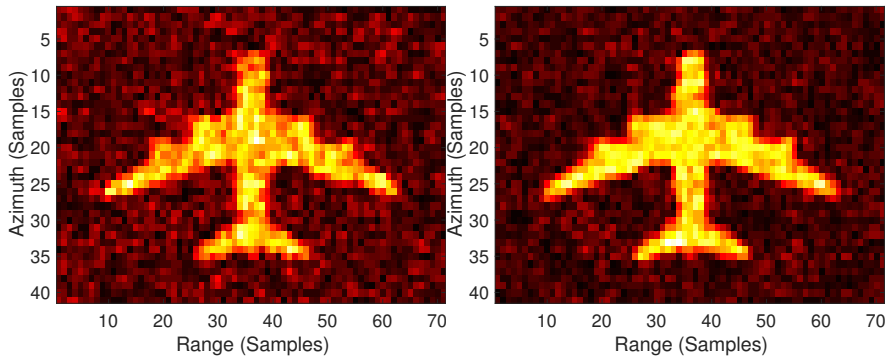

(C) 50 **(D)** 100

FIGURE 6.6: Radar image produced with different numbers of femtosatellites

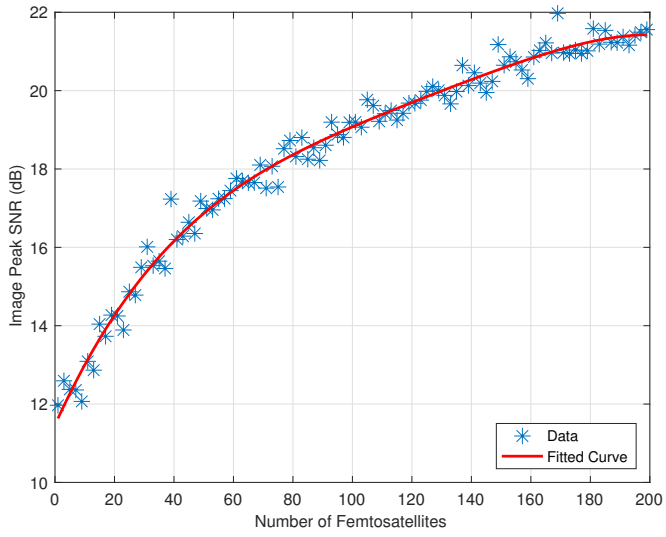

FIGURE 6.7: Image peak SNR against number of femtosatellites

6.4.2 Test 2: Received Signal SNR

Figure 6.8 shows the processed images with different signal-to-noise ratios. All images are processed based on the signal space from 20 femtosatellites. Figure 6.8a presents a similar result as the benchmark in Figure 6.5 with -30 *dB* SNR. As the SNR reduces, the airliner becomes less visible and hard to identify. The target is undetectable when the SNR reaches -60 *dB* as shown in Figure 6.8d.

Figure 6.9 shows a linear relationship between the received signal SNR and the image peak SNR. The image peak SNR will be saturated at low signal SNR and the target will not be visible at such a condition. An unsaturated low received signal SNR can still provide basic target detection capability, as shown in Figure 6.8c, and a high received signal SNR enables the identification capability as shown in Figure 6.8a and 6.8b. Based on these simulated result, it may possible to identify the airliner by its dimensions and number of engines when the signal SNR is -40 *dB* or higher. The required received signal SNR for a given femtosatellite swarm SAR system can then be estimated based on this simulated result.

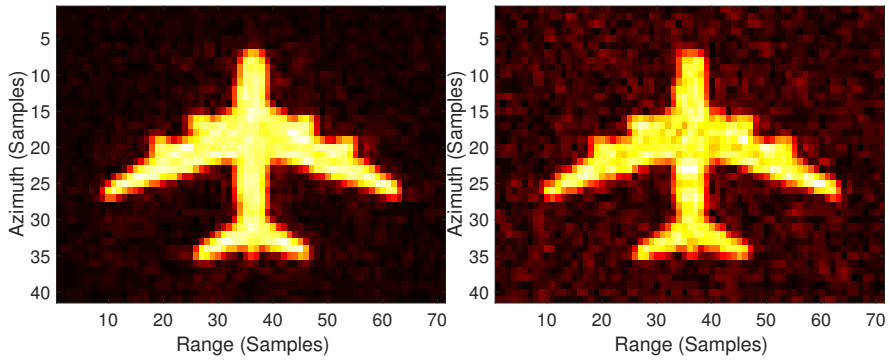

(A) -30 *dB*

(B) -40 *dB*

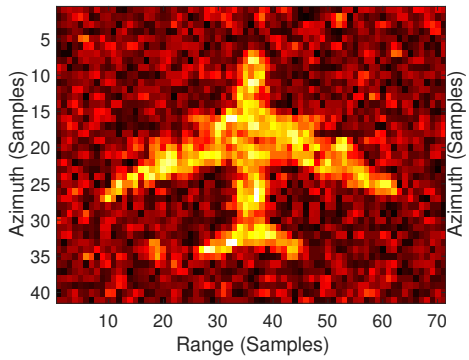

(C) -50 *dB*

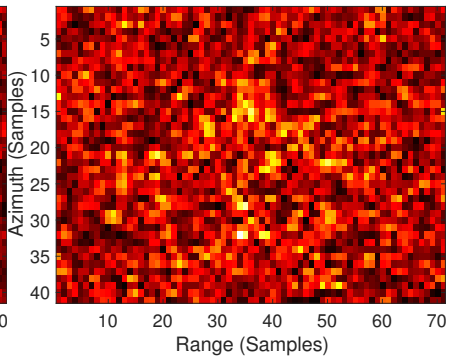

(D) -60 *dB*

FIGURE 6.8: Radar image produced with different received signal SNR

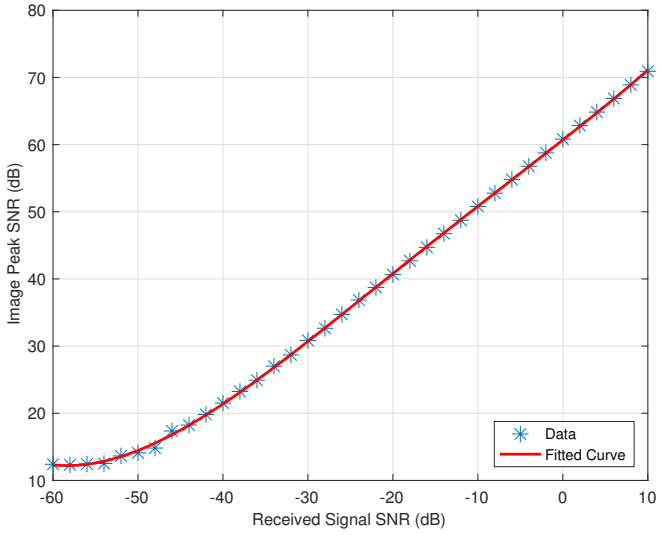

FIGURE 6.9: Image peak SNR against received signal SNR

6.4.3 Test 3: Positioning Error

In real-world scenarios, position errors will be present which will degrade the performance of the system. This will lead to an offset of the target in the final radar image. Figure 6.10 shows the effect of this error on processed radar images. All images are processed based on the signal space from 20 femtosatellites with -30 dB SNR. The processed radar image indicates an acceptable result with 2 m error, as shown in Figure 6.10b. The image is clearly blurred when the positioning error is 5 m. The image SNR flattens as positioning error increases and the boundary is proportional to the size of the target and the resolution of the radar. In Figure 6.10d, the target will be extremely hard to identify. Accurate position determination is key to reduce the ambiguity of the target. The effect of positioning error could be further reduced by matching the raw SAR data from each femtosatellite.

The effect of positioning error and SNR are shown in Figure 6.11. The image SNR has a steady drop as the positioning error increases unless it reaches a noise saturation at 12 dB where the target is entirely invisible. With higher SNR, the target remains detectable but no longer identifiable when the positioning error increases. This plot can be used to estimate the expected radar image quality from the bi-static femtosatellite swarm with a given system specification.

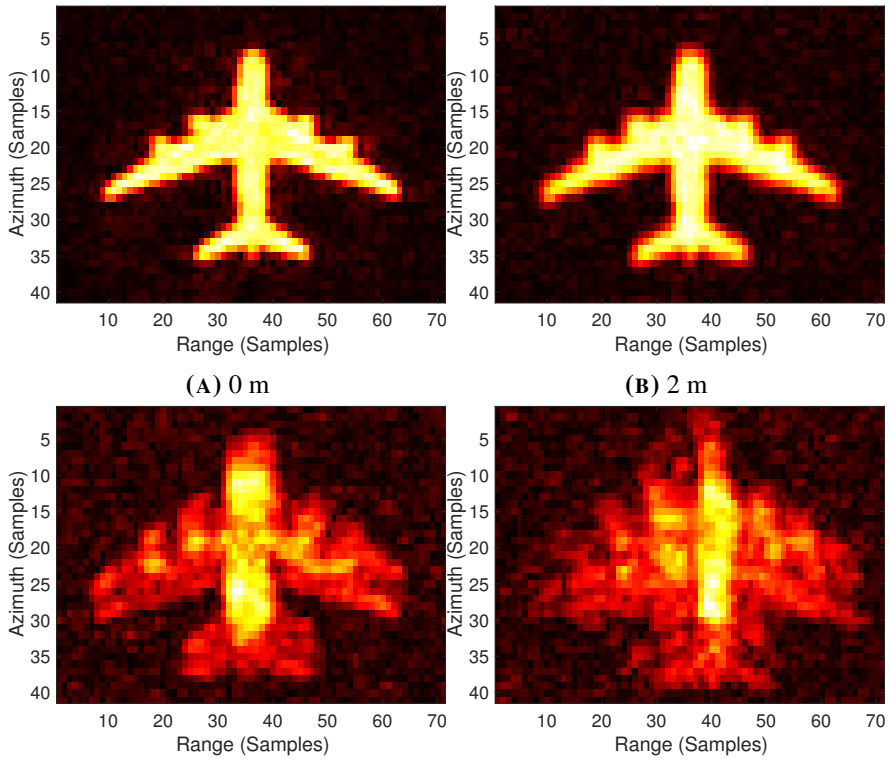

(A) 0 m **(B)** 2 m

(C) 5 m **(D)** 10 m

FIGURE 6.10: Radar image produced with different positioning errors

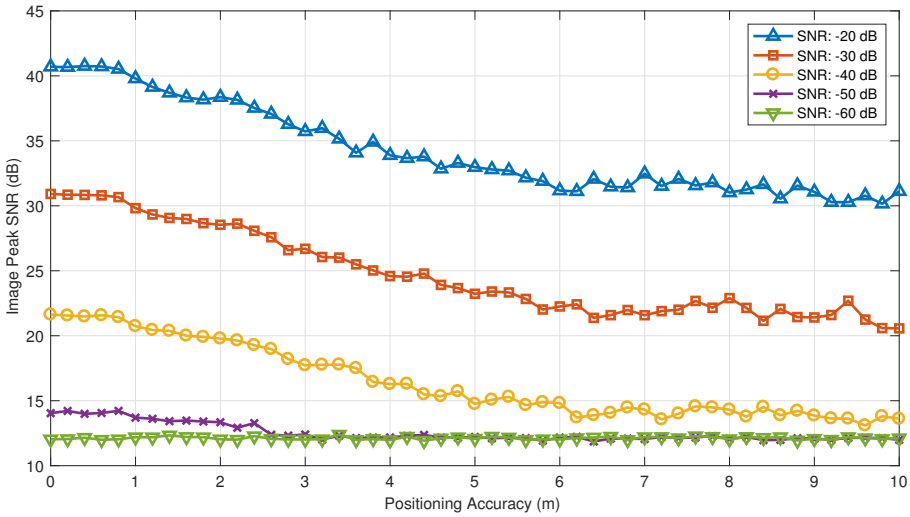

FIGURE 6.11: Image peak SNR

6.5 Space Situational Awareness

Space debris can be a threat to all active satellites and spacecraft (Johnson, 2010). Mullick et al. provides a comprehensive study of such threats (Mullick et al., 2019). Much research had been done on the detection of space debris (Anz-Meador et al., 2019; Mariappan et al., 2019).

In addition to the Earth remote sensing mission evaluated in Section 6.4, the same femtosatellite swarm could also be used to detect debris for space situational awareness. By adapting the RDA to focus on a moving target, on-orbit targets could be detected and imaged. In this scenario, both the femtosatellite swarm and the target are moving along their orbit. This is categorised as inverse synthetic aperture radar (ISAR) (Wang et al., 2018). Anger et al. and Qian et al. investigated advanced ISAR image processing algorithms to improve focusing in this scenario (Anger et al., 2019; Qian et al., 2019).

As noted in Section 6.2, motion along the range and the elevation directions will introduce focusing problems. In this section, the femtosatellite swarm and the target are investigated in a relative coordinate system where the origin is the target and is considered stationary. With the known orbit parameters of the femtosatellite swarm and the target, the relative motion can then be simplified. Targets on other orbits could also be detected by applying the SAR signal processing algorithm on the same SAR signal space with different target orbital elements.

6.5.1 Test 1: Target Orbit Altitude

The international space station (ISS) is used as the target, as shown in Figure 6.12, and the orbit specifications are listed in Table 6.2. It is the largest spacecraft in LEO and continuously faces the threat of collision with orbiting debris (Akella et al., 2000). It has an overall length

of 73 *m* and width of 110 *m* (Chan, 2009). The ISS is assumed to be in a circular orbit at 400 *km*[1] and an inclination of 51.64°. Figure 6.13 shows the radar image benchmark if the ISS was stationary.

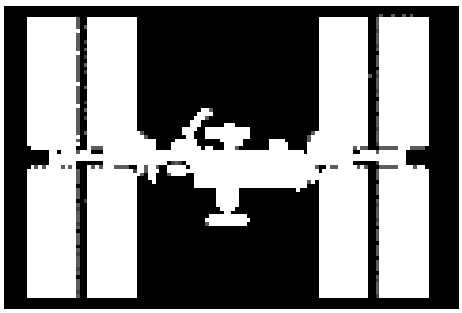

FIGURE 6.12: International space station (ISS)

TABLE 6.2: ISS orbit specifications

Parameter	Value
Orbit altitude	400 *km*
Inclination	51.64°
Speed	7.66 km/s

Figure 6.14 shows radar images of the ISS generated at different orbit altitudes without noise and positioning errors. The orbit inclination is 51.64° for each altitude and the speed is calculated based on the orbit altitudes. Compared to Figure 6.13, blurs are introduced due to the motion of ISS along the orbit. The shape of the ISS remains recognisable across all orbit altitudes. The intensity of the target in the radar images decreases while the orbit altitude increases. The modules of the ISS blur in Figure 6.14c and 6.14d due to the limited resolution of the SAR sensors composed by the femtosatellite swarm. Figure 6.15 shows a flat image

[1]The ISS altitude varies between 280 *km* and 460 *km* (Gustafsson et al., 2009).

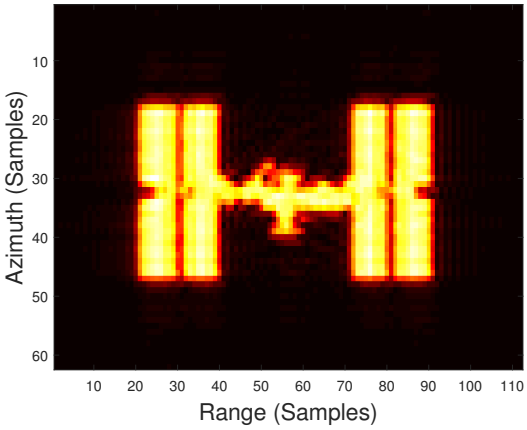

FIGURE 6.13: ISS image benchmark

peak SNR across all orbit altitudes. It can be considered that the target orbit altitude should not affect the performance of the space situational awareness application. Also, the magnitude of these results are approximately 9.6 dB which is worse than those in Section 6.4. This is caused by the additional motion of the target compared to the stationary scenario. It indicates that the performance of the SAR signal processing algorithm could be improved with advanced InSAR signal processing algorithms (Wang et al., 2018).

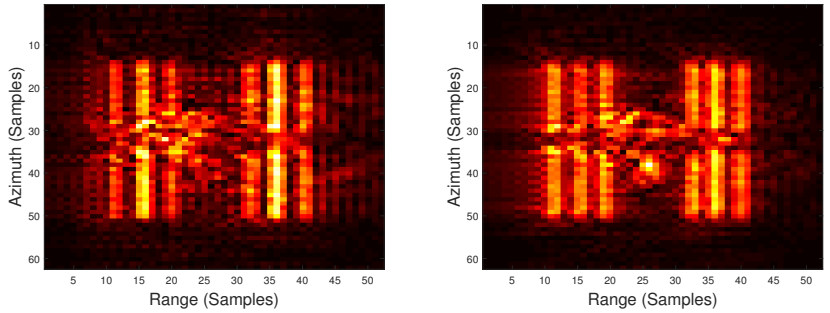

(A) 200 *km* **(B)** 300 *km*

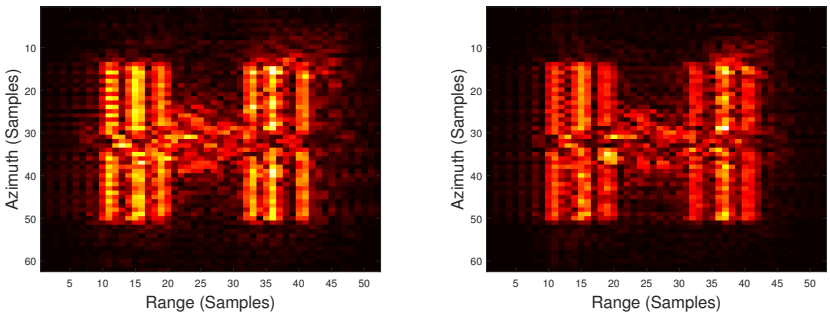

(C) 400 *km* **(D)** 500 *km*

FIGURE 6.14: Radar image produced of the ISS at different orbit altitudes

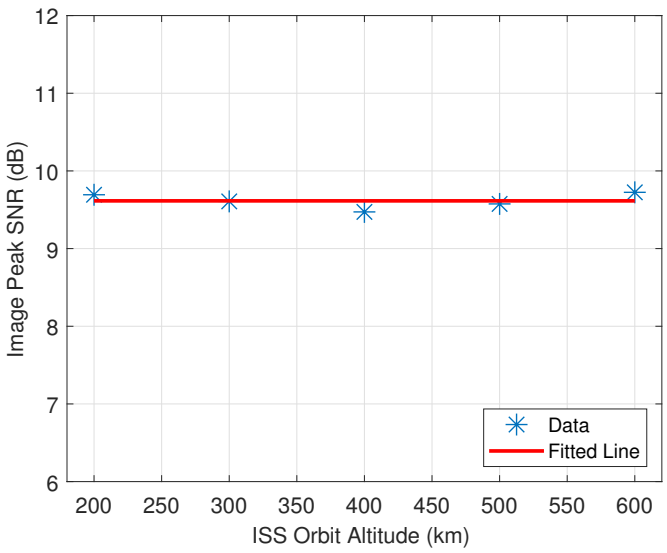

FIGURE 6.15: Image peak SNR of ISS at different orbit altitudes

6.5.2 Test 2: Target Size

After identifying the target spacecraft, a target with a square cross section is used to evaluate the capability of using the femtosatellite swarm to detect space debris. It is assumed that the target is orbiting at the same orbit as the ISS in a 400 km circular orbit. Figure 6.16 shows the radar images of different size targets. All images are processed based on the signal space from 20 femtosatellites with -50 dB SNR. As noted in Table 6.1, the approximate range resolution of the femtosatellite swarm is 1.5 m which is larger than most space debris (Smirnov, 2001).

Figure 6.16b, 6.16c and 6.16d show that the targets are detectable but unrecognisable when their size is smaller than the femtosatellite swarm SAR range resolution as listed in Table 6.1. This demonstrates that space debris smaller than a CubeSat could be detected by the femtosatellite swarm, although not spatially resolved. Figure 6.17 shows the image peak SNR against different target sizes. The image peak SNR is approximately 22.13 dB when the target size is larger or close to the radar system resolution, and approximately 20.56 dB when it is marginally smaller than the resolution. This shows that the image peak SNR can be used to test if the target been spatially resolved or not. Compared to stationary scenarios, the magnitude of the image peak SNR is higher due to the simple shape of the target. It also indicates that the image peak SNR is not related to the size of the target when it is not close to the radar system resolution.

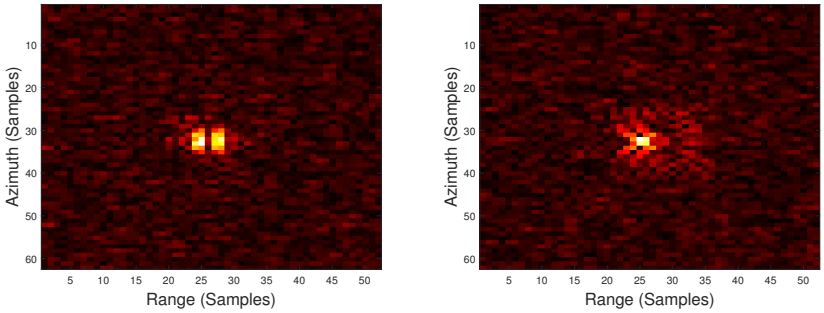

(A) $10 \times 10\ m$ **(B)** $1 \times 1\ m$

(C) $0.1 \times 0.1\ m$ **(D)** $0.01 \times 0.01\ m$

FIGURE 6.16: Radar image produced with different targets at the ISS orbit

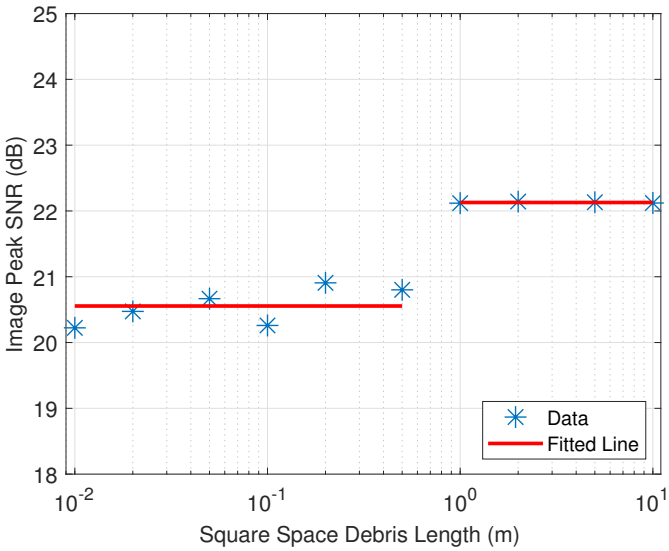

FIGURE 6.17: Image peak SNR against different space debris target sizes

6.6 Summary

In this chapter, the performance of the femtosatellite swarm for SAR applications is evaluated. A modified range-Doppler algorithm is proposed in Section 6.2 to process the received signal at the femtosatellite and generate the radar image. In Section 6.3, the performance of the femtosatellite swarm is analysed by using NESZ and SNR. A theoretical performance for SAR missions can then be estimated. It has then been further evaluated with a simulated mock mission scenario in different configurations in Section 6.4. The radar image quality from the femtosatellite swarm can be estimated based on the simulated configurations. Finally, by focusing the SAR signal processing for on-orbit targets, the femtosatellite swarm could be used for on-orbit target and space debris detection as demonstrated in Section 6.5.

Chapter 7

Conclusions and Future Work

7.1 Conclusions

This thesis provided a comprehensive system level analysis of femtosatellite swarms for synthetic aperture radar applications. It covers femtosatellite prototype design, orbital dynamics and control and synthetic aperture radar performance.

In Chapter 2, an extensive review of femtosatellite systems was provided. The femtosatellite concept and its subsystems were discussed to provide the foundation of the thesis. In particular, each subsystem is discussed in detail, specifically for the femtosatellite concept. Current designs of femtosatellites were reviewed as proof of concepts. WikiSat and Sprite prove the basic functionality of the femtosatellite concept. Solar sailing and relative motion are then introduced to establish the orbital dynamics required for the thesis. An active control strategy can be developed within such dynamic models. In addition, Sun-synchronous orbits are key to exploit the femtosatellite concept. In such orbits, the femtosatellite is under constant

illumination without eclipse, which increases the femtosatellite's orbit lifetime and mission capability. This combination provides an unique opportunity to enable the femtosatellite swarm to be used for synthetic aperture radar applications.

Chapter 3 introduced the basics of synthetic aperture radar. A signal model was provided to generate radar signals in a simulated scenario. Common radar system configurations, especially the bi-static configuration, were discussed for femtosatellite-based SAR missions. The range-Doppler algorithm was introduced to process the data from such missions and produce the final radar image. Current spaceborne missions were also reviewed as inspiration for the femtosatellite synthetic aperture radar mission.

A novel femtosatellite mission concept was proposed in Chapter 4 to exploit the concept of femtosatellite swarms. With this mission in mind, the design objectives were listed and discussed. The geometries of the femtosatellites were compared to take advantage of Sun-synchronous orbits and solar sailing. A novel flat-bubble shaped femtosatellite concept was then proposed. Its flat design is capable of maximising solar radiation pressure for orbit control while minimising atmospheric drag. The bubble protects the core electronics from solar radiation and heat. Electrochromic panels on each corner of the femtosatellite enable the control of solar radiation pressure, therefore generating torques for active attitude and orbit control. Finally, a detailed mission concept and femtosatellite hardware design were presented for later analysis in Chapter 5.

In Chapter 5, the orbital dynamics and orbit control of a femtosatellite in relative motion were explored, with assumptions made to simplify the analysis. The orbital dynamics of relative motion was investigated with external accelerations. The effect of solar radiation pressure, atmospheric drag and differential forces relative to the carrier spacecraft were evaluated in the

relative motion analysis. The attitude dynamics of the problem was then studied to exploit the manoeuvrability of the femtosatellite. An active orbit control strategy was developed based on solar radiation pressure. This demonstrates the attitude transfer process between different attitudes, therefore, enabling control of the orbit of the femtosatellite within the relative motion analysis. Example scenarios with low and high deployment speeds were presented to demonstrate the feasibility of the active orbit control strategy. An example of femtosatellite swarm deployment evolution was provided. This demonstrates the feasibility of the mission concept defined in Chapter 4.

With active orbit control, a swarm of femtosatellites can be controlled and positioned around the carrier spacecraft. Chapter 6 evaluates the performance of such femtosatellite swarms for the synthetic aperture radar applications. A modified range-Doppler algorithm was presented to process the radar signal from the femtosatellite swarm. The performance of the femtosatellite SAR system was analysed by noise equivalent sigma zero (NESZ) and signal-to-noise ratio (SNR). The results were then confirmed by a mock mission scenario. The performance of the swarm was evaluated in three different configurations: the number of femtosatellites, received radar signal SNR and positioning error. Based on these result, the performance of a given femtosatellite swarm configuration can be estimated. Furthermore, space situational awareness for on-orbit targets was also investigated to enhance the mission capability of the femtosatellite swarm. By refocusing the SAR processing on a moving target, orbiting targets and space debris can be detected and imaged.

7.2 Future Work

This thesis has demonstrated the feasibility of using femtosatellite swarms with active orbit control for synthetic aperture radar missions. A range of research topics can be further investigated.

The femtosatellite concept can benefit from a more comprehensive analyse of orbital dynamics and perturbations. With the latest development in MEMS technology, MEMS mirrors can be used in addition to the electrochromic panels. MEMS mirrors are able to provide torque to control the femtosatellite attitude in the yaw axis. A new closed-loop active orbit control strategy can then be developed for a more comprehensive dynamics model.

The hardware of the femtosatellite could be further optimised by using customised components, especially on the radar payload subsystem. As demonstrated in Chapter 6, the radar performance is strongly related to the radar received signal SNR. A faster communication link between the femtosatellites and the carrier spacecraft can reduce the response time of the femtosatellite swarm between measurements. The carrier spacecraft could also be investigated for different radar missions.

The sources of noise in the space environment can be evaluated to improve the accuracy of performance analysis. The performance of the femtosatellite swarm can be further improved by an advanced bi-static synthetic aperture radar signal processing method. As noted in Chapter 6, more advanced ISAR signal processing algorithms could be investigated to increase on-orbit target detection performance. In addition, a wider spatial spread of the femtosatellite swarm has the potential to form a sparse aperture radar system.

Appendix A

Clohessy-Wiltshire Equations with External Acceleration

First, re-write Equation (2.2a) as

$$\ddot{x} = a_x + 2\omega_n \dot{y} + 3\omega_n^2 x \tag{A.1}$$

and differentiate both sides

$$\dddot{x} = 2\omega_n \ddot{y} + 3\omega_n^2 \dot{x} \tag{A.2}$$

substituting $\ddot{y}$ in Equation (A.2) with Equation (2.2b), this becomes

$$\dddot{x} = 2\omega_n (a_y - 2\omega_n \dot{x}) + 3\omega_n^2 \dot{x} = 2\omega_n a_y - \omega_n^2 \dot{x} \tag{A.3}$$

and applying a Laplace transform provides

$$s^3X(s) - s^2x_0 - s\dot{x}_0 - \ddot{x}_0 + \omega_n^2 sX(s) - \omega_n^2 x_0 - \frac{2\omega_n a_y}{s} = 0 \tag{A.4}$$

which then becomes

$$sX(s)(s^2 + \omega_n^2) = (s^2 + \omega_n^2)x_0 + s\dot{x}_0 + \ddot{x}_0 + \frac{2\omega_n a_y}{s} \tag{A.5}$$

Then, solving for $X(s)$, it is found that

$$X(s) = \frac{x_0}{s} + \frac{\dot{x}_0}{s^2 + \omega_n^2} + \frac{\ddot{x}_0}{s\omega_n^2} - \frac{s\ddot{x}_0}{s(s^2 + \omega_n^2)} + \frac{2a_y}{s^2\omega_n} - \frac{2a_y}{\omega_n(s^2 + \omega_n^2)} \tag{A.6}$$

and applying the inverse Laplace transform to obtain the time domain solution, it is found that

$$x(t) = \left(\frac{\dot{x}_0}{\omega_n} - \frac{2a_y}{\omega_n^2}\right)\sin(\omega_n t) - \left(3x_0 + \frac{2\dot{y}_0}{\omega_n} + \frac{a_x}{\omega_n^2}\right)\cos(\omega_n t) \tag{A.7}$$

Taking the derivative of Equation (A.7) provides the time domain solution for $\dot{x}$, such that

$$\dot{x}(t) = \left(3\omega_n x_0 + 2\dot{y}_0 + \frac{a_x}{\omega_n}\right)\sin(\omega_n t) + \left(\dot{x}_0 - \frac{2a_y}{\omega_n}\right)\cos(\omega_n t) + \frac{2a_y}{\omega_n} \tag{A.8}$$

Then, re-writing Equation (2.2b) as

$$\ddot{y} = a_y - 2\omega_n\dot{x} \tag{A.9}$$

and substituting $\dot{x}$ with Equation (A.8) to obtain

$$\ddot{y} = a_y - 2\omega_n \left[\left(3\omega_n x_0 + 2\dot{y}_0 + \frac{a_x}{\omega_n} \right) \sin(\omega_n t) + \left(\dot{x}_0 - \frac{2a_y}{\omega_n} \right) \cos(\omega_n t) + \frac{2a_y}{\omega_n} \right] \tag{A.10}$$

This can be expanded as

$$\ddot{y} = -(2\omega_n \dot{x}_0 - 4a_y)\cos(\omega_n t) - (6\omega_n^2 x_0 + 4\omega_n \dot{y}_0 + 2a_x)\sin(\omega_n t) - 3a_y \tag{A.11}$$

Then, integrating to find $\dot{y}$ and y, it can be shown that

$$\dot{y} = -(2\dot{x}_0 - \frac{4a_y}{\omega_n})\sin(\omega_n t) + (6\omega_n x_0 + 4\dot{y}_0 + \frac{2a_x}{\omega_n})\cos(\omega_n t) - 3a_y t + C \tag{A.12}$$

$$y = (\frac{2\dot{x}_0}{\omega_n} - \frac{4a_y}{\omega_n^2})\cos(\omega_n t) + (6x_0 + \frac{4\dot{y}_0}{\omega_n} + \frac{2a_x}{\omega_n^2})\sin(\omega_n t) - \frac{3}{2}a_y t + Ct + D \tag{A.13}$$

where C and D are constants. When $t = 0$, the results become

$$\dot{y}_0 = 6\omega_n x_0 + 4\dot{y}_0 + \frac{2a_x}{\omega_n} + C \tag{A.14}$$

$$y_0 = \frac{2\dot{x}_0}{\omega_n} - \frac{4a_y}{\omega_n^2} + D \tag{A.15}$$

therefore

$$C = -6\omega_n x_0 - 3\dot{y}_0 - \frac{2a_x}{\omega_n} \tag{A.16}$$

$$D = y_0 - \frac{2\dot{x}_0}{\omega_n} + \frac{4a_y}{\omega_n^2} \tag{A.17}$$

and the time domain solution for $\dot{y}$ and y is given by

$$\dot{y}(t) = -\left(2\dot{x}_0 - \frac{4a_y}{\omega_n}\right)\sin(\omega_n t) + \left(6\omega_n x_0 + 4\dot{y}_0 + \frac{2a_x}{\omega_n}\right)\cos(\omega_n t) - 3a_y t - \left(6\omega_n x_0 + 3\dot{y}_0 + \frac{2a_x}{\omega_n}\right) \tag{A.18a}$$

$$y(t) = \left(6x_0 + \frac{4\dot{y}_0}{\omega_n} + \frac{2a_x}{\omega_n^2}\right)\sin(\omega_n t) + \left(\frac{2\dot{x}_0}{\omega_n} - \frac{4a_y}{\omega_n^2}\right)\cos(\omega_n t) - \frac{3a_y}{2}t^2 - \left(6\omega_n x_0 + 3\dot{y}_0 + \frac{2a_x}{\omega_n}\right)t + \left(y_0 - \frac{2\dot{x}_0}{\omega_n} + \frac{4a_y}{\omega_n^2}\right) \tag{A.18b}$$

Finally, re-writing Equation (2.2c) as

$$\ddot{z} + \omega_n^2 z - a_z = 0 \tag{A.19}$$

and applying a Laplace transform, it is found that

$$s^2 Z(s) - s z_0 - \dot{z}_0 + \omega_n^2 Z(s) - \frac{a_z}{s} = 0 \tag{A.20}$$

which becomes

$$(s^2 + \omega_n^2)Z(s) = \frac{a_z}{s} + s z_0 + \dot{z}_0 \tag{A.21}$$

and can be solved for $Z(s)$ as

$$Z(s) = \frac{s z_0}{s^2 + \omega_n^2} + \frac{\dot{z}_0}{s^2 + \omega_n^2} + \frac{a_z}{s\omega_n^2} - \frac{s a_z}{\omega_n^2(s^2 + \omega_n^2)} \tag{A.22}$$

Then, applying the inverse Laplace transform to obtain the time domain solution for z, it is found that

$$z(t) = \frac{\dot{z}_o}{\omega_n}\sin(\omega_n t) + \left(z_0 - \frac{a_z}{\omega_n^2}\right)\cos(\omega_n t) + \frac{a_z}{\omega_n^2} \tag{A.23}$$

and taking the derivative, the time domain solution for $\dot{z}$ can be found as

$$\dot{z}(t) = -\left(\omega_n z_0 - \frac{a_z}{\omega_n}\right)\sin(\omega_n t) + \dot{z}_0\cos(\omega_n t) \tag{A.24}$$

Finally, the analytical solution for the Clohessy-Wiltshire equations with external acceleration become

$$\begin{aligned}
x(t) =& \left(\frac{\dot{x}_0}{\omega_n} - \frac{2a_y}{\omega_n^2}\right)\sin(\omega_n t) - \left(3x_0 + \frac{2\dot{y}_0}{\omega_n} + \frac{a_x}{\omega_n^2}\right)\cos(\omega_n t) \\
&+ \frac{2a_y}{\omega_n}t + \left(4x_0 + \frac{2\dot{y}_0}{\omega_n} + \frac{a_x}{\omega_n^2}\right) && \text{(A.25a)} \\
y(t) =& \left(6x_0 + \frac{4\dot{y}_0}{\omega_n} + \frac{2a_x}{\omega_n^2}\right)\sin(\omega_n t) + \left(\frac{2\dot{x}_0}{\omega_n} - \frac{4a_y}{\omega_n^2}\right)\cos(\omega_n t) \\
&- \frac{3a_y}{2}t^2 - \left(6\omega_n x_0 + 3\dot{y}_0 + \frac{2a_x}{\omega_n}\right)t + \left(y_0 - \frac{2\dot{x}_0}{\omega_n} + \frac{4a_y}{\omega_n^2}\right) && \text{(A.25b)} \\
z(t) =& \frac{\dot{z}_o}{\omega_n}\sin(\omega_n t) + \left(z_0 - \frac{a_z}{\omega_n^2}\right)\cos(\omega_n t) + \frac{a_z}{\omega_n^2} && \text{(A.25c)} \\
\dot{x}(t) =& \left(3\omega_n x_0 + 2\dot{y}_0 + \frac{a_x}{\omega_n}\right)\sin(\omega_n t) + \left(\dot{x}_0 - \frac{2a_y}{\omega_n}\right)\cos(\omega_n t) + \frac{2a_y}{\omega_n} && \text{(A.25d)} \\
\dot{y}(t) =& -\left(2\dot{x}_0 - \frac{4a_y}{\omega_n}\right)\sin(\omega_n t) + \left(6\omega_n x_0 + 4\dot{y}_0 + \frac{2a_x}{\omega_n}\right)\cos(\omega_n t) \\
&- 3a_y t - \left(6\omega_n x_0 + 3\dot{y}_0 + \frac{2a_x}{\omega_n}\right) && \text{(A.25e)} \\
\dot{z}(t) =& -\left(\omega_n z_0 - \frac{a_z}{\omega_n}\right)\sin(\omega_n t) + \dot{z}_0\cos(\omega_n t) && \text{(A.25f)}
\end{aligned}$$

Appendix B

Evolution of Femtosatellite Swarm Deployment

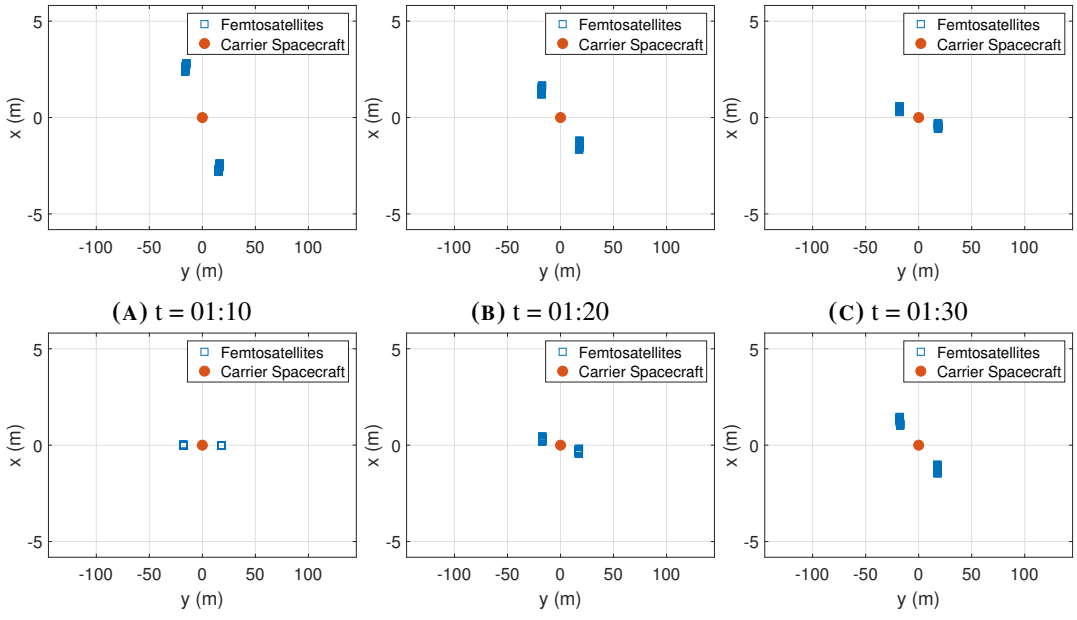

(A) t = 01:10 **(B)** t = 01:20 **(C)** t = 01:30

(D) t = 01:40 **(E)** t = 01:50 **(F)** t = 02:00

FIGURE B.1: Deployed femtosatellites over time, *xy*-plane (hr:min)

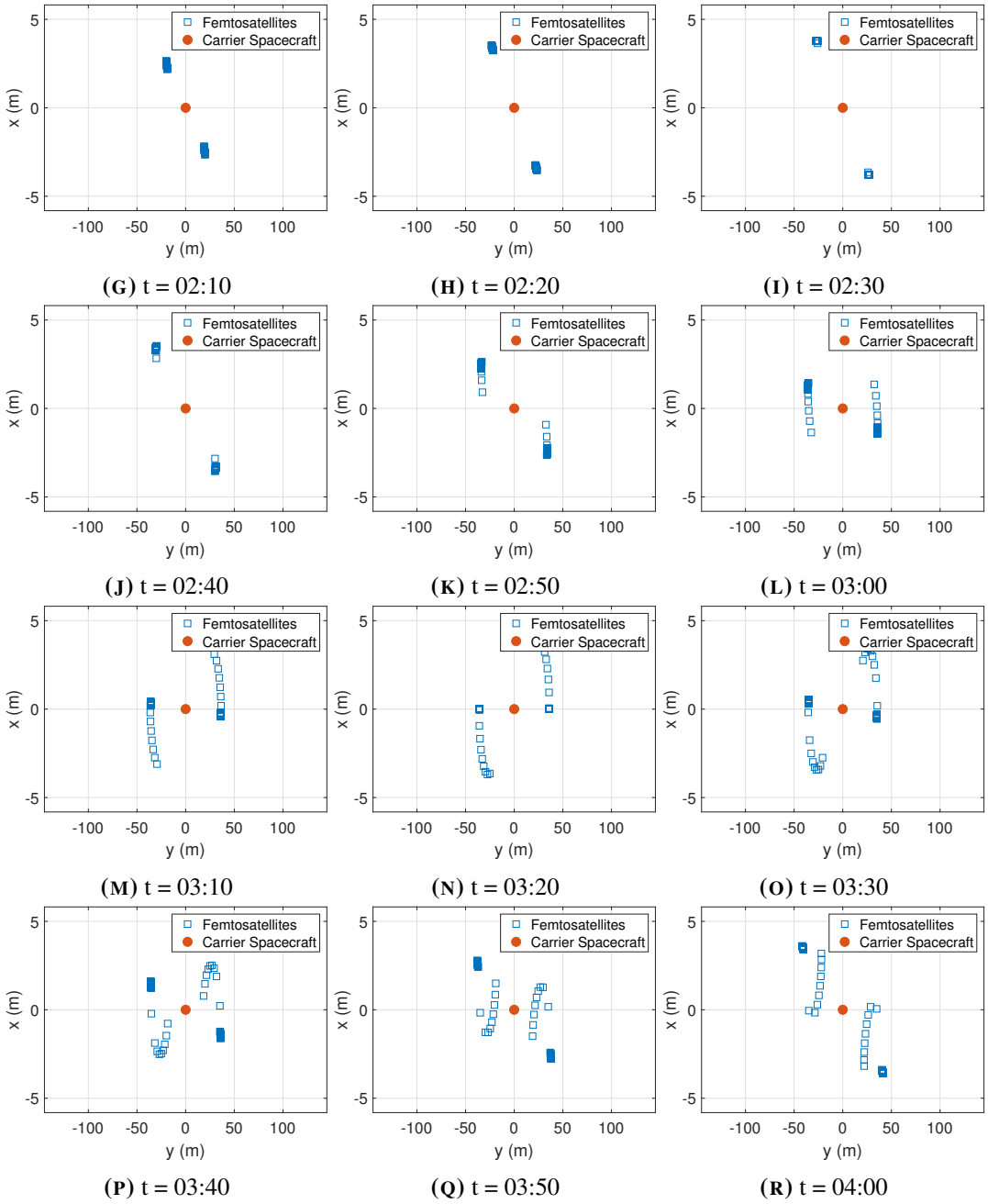

(G) t = 02:10 **(H)** t = 02:20 **(I)** t = 02:30

(J) t = 02:40 **(K)** t = 02:50 **(L)** t = 03:00

(M) t = 03:10 **(N)** t = 03:20 **(O)** t = 03:30

(P) t = 03:40 **(Q)** t = 03:50 **(R)** t = 04:00

FIGURE B.1: Deployed femtosatellites over time, *xy*-plane (hr:min) (continued)

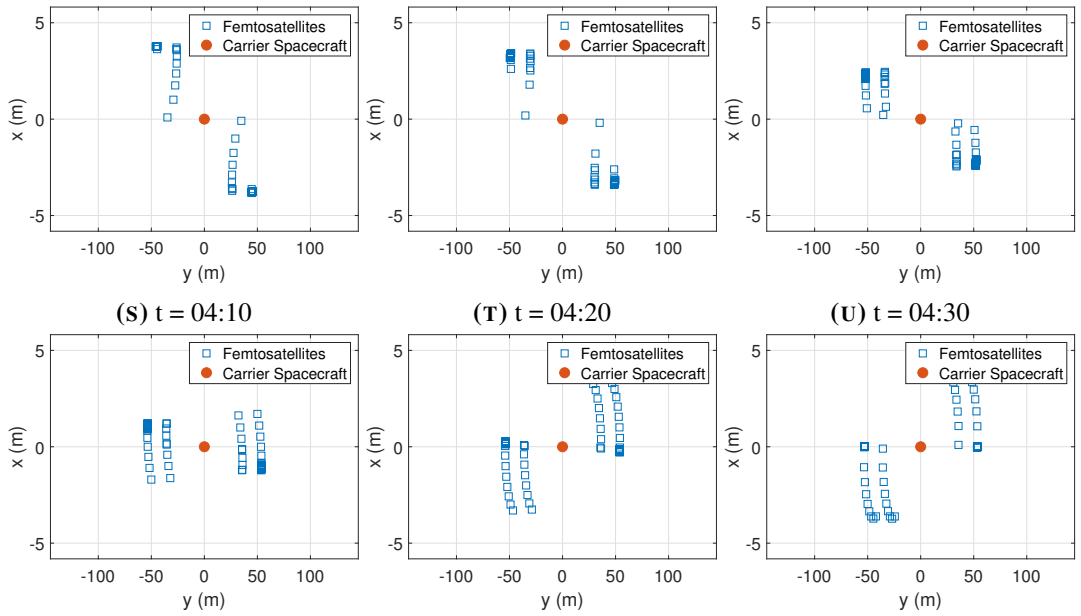

(S) t = 04:10 (T) t = 04:20 (U) t = 04:30

(V) t = 04:40 (W) t = 04:50 (X) t = 05:00

FIGURE B.1: Deployed femtosatellites over time, *xy*-plane (hr:min) (continued)

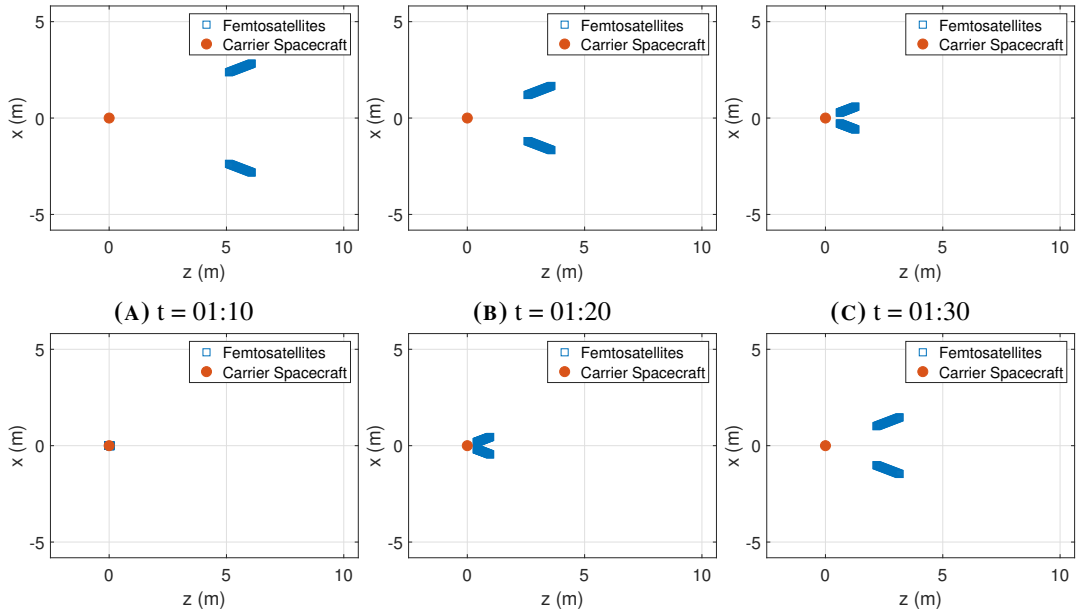

(A) t = 01:10 (B) t = 01:20 (C) t = 01:30

(D) t = 01:40 (E) t = 01:50 (F) t = 02:00

FIGURE B.2: Deployed femtosatellites over time, *xz*-plane (hr:min)

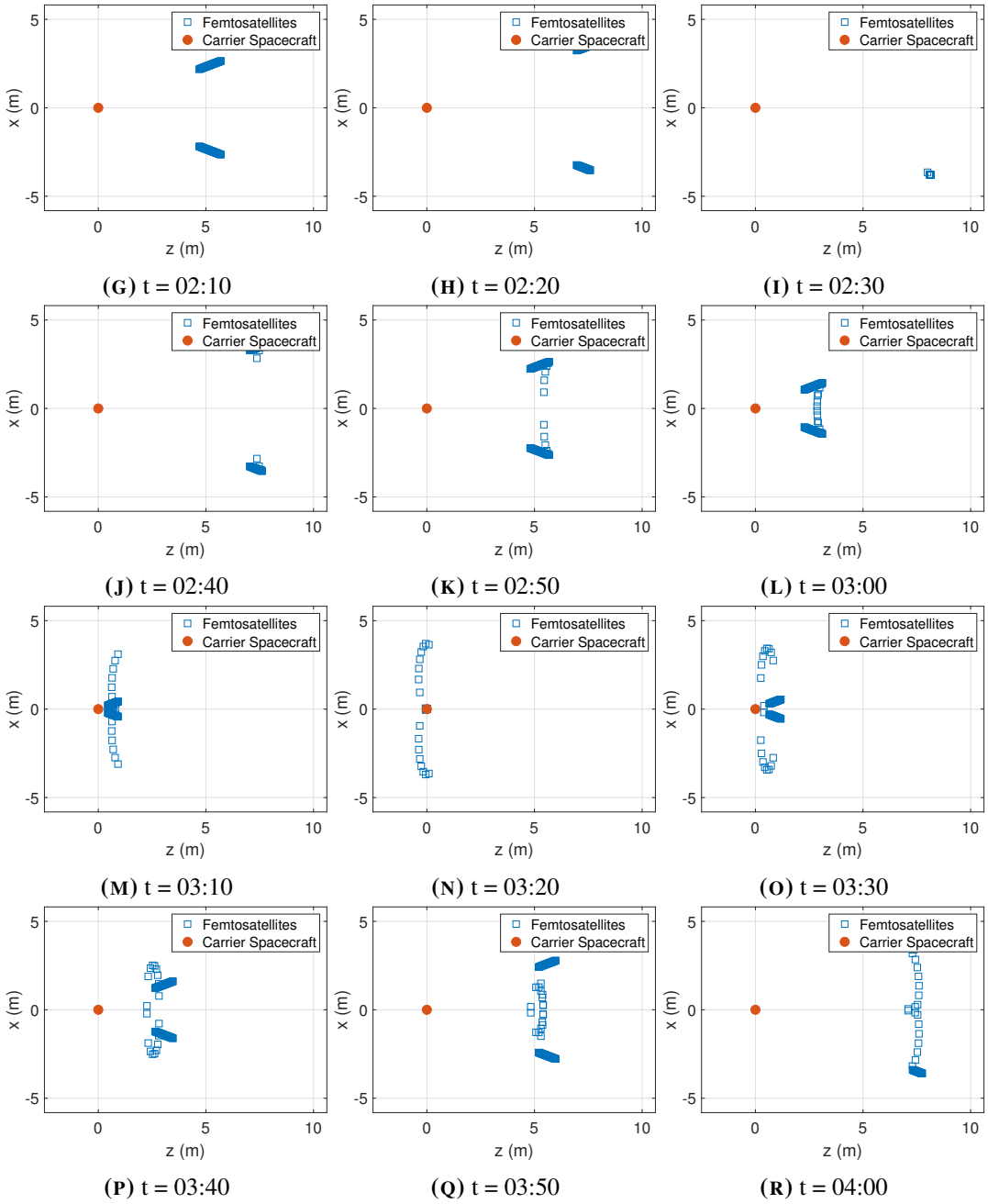

(G) t = 02:10 **(H)** t = 02:20 **(I)** t = 02:30

(J) t = 02:40 **(K)** t = 02:50 **(L)** t = 03:00

(M) t = 03:10 **(N)** t = 03:20 **(O)** t = 03:30

(P) t = 03:40 **(Q)** t = 03:50 **(R)** t = 04:00

FIGURE B.2: Deployed femtosatellites over time, *xz*-plane (hr:min) (continued)

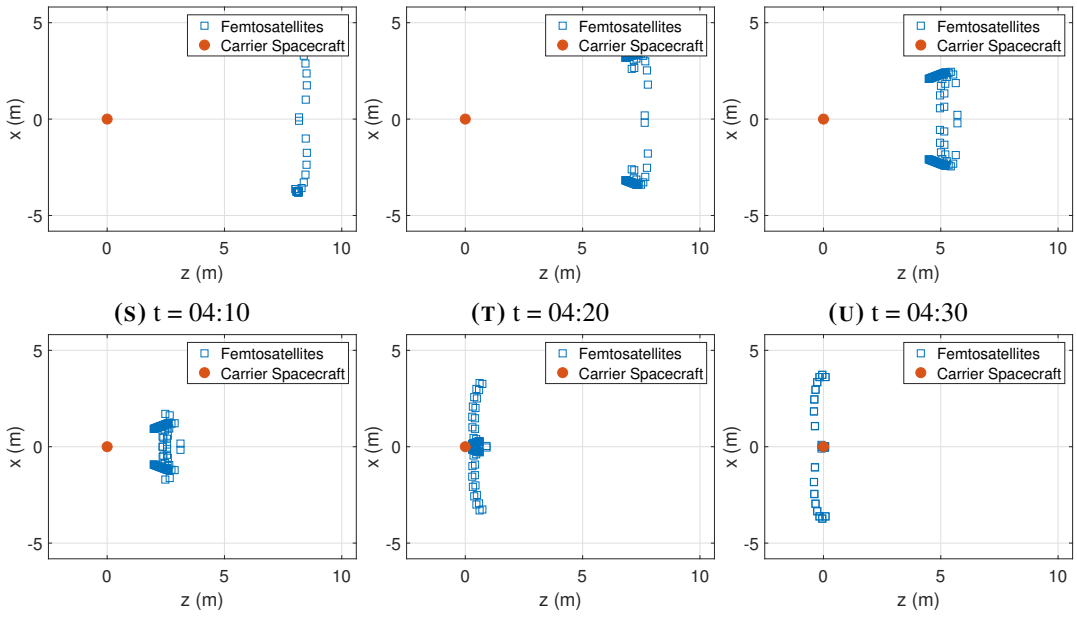

(S) t = 04:10 **(T)** t = 04:20 **(U)** t = 04:30

(V) t = 04:40 **(W)** t = 04:50 **(X)** t = 05:00

FIGURE B.2: Deployed femtosatellites over time, *xz*-plane (hr:min) (continued)

Bibliography

Adams, V. H. and Peck, M. (2019). "R-Selected Spacecraft". In: *Journal of Spacecraft and Rockets* 57.1, pp. 1–9. DOI: 10.2514/1.a34564.

Agrawal, D. P. and Zeng, Q.-a. (2011). *Introduction to Wireless and Mobile Systems*. CL-Engineering. ISBN: 978-1439062074.

Akella, M. R. and Alfriend, K. T. (2000). "Probability of collision between space objects". In: *Journal of Guidance, Control, and Dynamics* 23.5, pp. 769–772.

Albuquerque, M., Prats, P., and Scheiber, R. (2008). "Applications of Time-Domain Back-Projection SAR Processing in the Airborne Case". In: *7th European Conference on Synthetic Aperture Radar*, pp. 1–4.

Alta Devices, ed. (2020). *World's most efficient, thin and flexible solar technology*. URL: https://www.altadevices.com/technology/ (visited on 02/02/2020).

Analog Decice, ed. (2020). *ADP5090*. URL: https://www.analog.com/en/products/adp5090.html (visited on 02/02/2020).

Anger, S., Anglberger, H., Jirousek, M., Dill, S., and Peichl, M. (2019). "ISAR Imaging of Satellites in Space – Simulations and Measurements". In: *2019 20th International Radar Symposium (IRS)*. IEEE. DOI: 10.23919/irs.2019.8768095.

Anz-Meador, P., Ward, M., Manis, A., Nornoo, K., Dolan, B., Claunch, C., and Rivera, J. (2019). "The Space Debris Sensor Experiment". In: *1st International Orbital Debris (IOC) Conference, Houston, TX, United States*.

Atchison, J. and Peck, M. (2007). "A Millimeter-Scale Lorentz-Propelled Spacecraft". In: *AIAA Guidance, Navigation and Control Conference and Exhibit*. American Institute of Aeronautics and Astronautics. DOI: 10.2514/6.2007-6847.

Atchison, J. and Peck, M. (2011). "Length Scaling in Spacecraft Dynamics". In: *Journal of Guidance, Control, and Dynamics* 34.1, pp. 231–246. DOI: 10.2514/1.49383.

Bandyopadhyay, S., Subramanian, G. P., Foust, R., Morgan, D., Chung, S.-J., and Hadaegh, F. (2015). "A Review of Impending Small Satellite Formation Flying Missions". In: *53rd AIAA Aerospace Sciences Meeting*. American Institute of Aeronautics and Astronautics. DOI: 10.2514/6.2015-1623.

Barnhart, D. J., Vladimirova, T., and Sweeting, M. N. (2005). "Satellite-on-a-chip: A Feasibility Study". In: *Procedding 5th Round Table on Micro/Nano Technologies for Space*.

Barnhart, D. J., Vladimirova, T., and Sweeting, M. N. (2007a). "System-on-a-Chip Design of Self-Powered Wireless Sensor Nodes for Hostile Environments". In: *2007 IEEE Aerospace Conference*. IEEE. DOI: 10.1109/aero.2007.352640.

Barnhart, D. J., Vladimirova, T., and Sweeting, M. N. (2007b). "Very-Small-Satellite Design for Distributed Space Missions". In: *Journal of Spacecraft and Rockets* 44.6, pp. 1294–1306. DOI: 10.2514/1.28678.

Barnhart, D. J., Vladimirova, T., Sweeting, M. N., Balthazor, R. L., Enloe, L. C., Krause, L. H., Lawrence, T. J., Mcharg, M. G., Lyke, J. C., White, J. J., and Baker, A. M. (2007). "Enabling Space Sensor Networks with PCBSat". In: *21st Annual Conference on Small Satellites*.

Becena, A., Diaz, M., and Zagal, J. C. (2012). "Feasibility Study of using a Small Satellite Constellation to Forecast, Monitor and Mitigate Natural and Man-made Disasters in Chile and Similar Developing Countries". In: *Proceedings of the AIAA/USU Conference on Small Satellites*. SSC12-IV-8.

Bell, I. (2014). "Miniature Electrodynamic Tethers to Enhance Picosatellite and Femtosatellite". In: *Proceedings of the AIAA/USU Conference on Small Satellites*. SSC14-VIII-2.

Bell, I., Gilchrist, B., McTernan, J., Bilen, S., Voronka, N., Hoyt, R., and Peck, M. (2011). "Enabling Ultra-small Sensor Spacecraft for the Space Environment using Small-Scale Electrodynamic Tethers". In: *AIAA SPACE 2011 Conference & Exposition*. American Institute of Aeronautics and Astronautics. DOI: 10.2514/6.2011-7322.

Bergman, J. E. S., Blott, R. J., Forbes, A. B., Humphreys, D. A., Robinson, D. W., and Stavrinidis, C. (2009). "FIRST Explorer – An innovative low-cost passive formation-flying system". In: *European Air & Space Conference*. arXiv: 0911.0991v1 [astro-ph.IM].

Bianchessi, N. and Righini, G. (2008). "Planning and scheduling algorithms for the COSMO-SkyMed constellation". In: *Aerospace Science and Technology* 12.7, pp. 535–544.

Boyvat, M., Koh, J.-S., and Wood, R. J. (2017). "Addressable wireless actuation for multijoint folding robots and devices". In: *Science Robotics* 2.8, eaan1544. DOI: 10.1126/scirobotics.aan1544.

Cao, J., Clemente, C., Mcinnes, C., Soraghan, J., and Uttamchandani, D. (2015). "A Novel Concept for Earth Remote Sensing Using A Bi-static Femto-satellite Swarm in Sun Synchronous Orbit". In: *66th International Astronautical Congress, Jerusalem, Israel*.

Chan, K. (2009). "International space station collision probability". In: *The Aerospace Corporation, Chantilly, VA, USA*.

Cherniakov, M. (2008). *Bistatic Radar*. Wiley-Blackwell. 406 pp. ISBN: 0470026316. URL: https://www.ebook.de/de/product/6821355/mikhail_cherniakov_bistatic_radar.html.

Clemente, C. (2013). "Advanced High Resolution Methods for Radar Imaging and Micro-Doppler Signature Extraction". PhD Thesis. University of Strathclyde.

Coldewey, D. (2019). *KickSat-2 project launches 105 cracker-sized satellites*. URL: https://techcrunch.com/2019/06/04/kicksat-2-project-launches-105-cracker-sized-satellites/ (visited on 02/02/2020).

Cumming, I. G. and Wong, F. H. (2005). *Digital Processing of Synthetic Aperture Radar Data: Algorithms and Implementation*. Artech House. ISBN: 1580530583.

Displays, R. (2020). *Printed Flexible Electrochromic Displays*. URL: https://rdotdisplays.com/displays (visited on 02/02/2020).

Doorly, J. E. and Oldfield, M. L. G. (1987). "The theory of advanced multi-layer thin film heat transfer gauges". In: *International Journal of Heat and Mass Transfer* 30.6, pp. 1159–1168. DOI: 10.1016/0017-9310(87)90045-7.

Engelen, S., Oever, M. van den, Mahapatra, P., Sundaramoorthy, P., Gill, E., Meijer, R., and Verhoeven, C. (2012). "NanoSAR – Case Study of Synthetic Aperture Radar for Nanosatellites". In: *63rd International Astronautical Congress*.

Farquharson, G., Woods, W., Stringham, C., Sankarambadi, N., and Riggi, L. (2018). "The Capella Synthetic Aperture Radar Constellation". In: *EUSAR 2018; 12th European Conference on Synthetic Aperture Radar*, pp. 1–5.

Fernandez-Murcia, E., Izquierdo, L., and Tristancho, J. (2011). "A synthetic aperture antenna for femto-satellites based on commercial-of-the-shelf". In: *2011 IEEE/AIAA 30th Digital Avionics Systems Conference*. IEEE. DOI: 10.1109/dasc.2011.6096138.

Griffiths, H. and Willis, N. (2010). "Klein Heidelberg - The First Modern Bistatic Radar System". In: *IEEE Transactions on Aerospace and Electronic Systems* 46.4, pp. 1571–1588. DOI: 10.1109/taes.2010.5595580.

Gustafsson, K., Sihver, L., Mancusi, D., Sato, T., and Niita, K. (2009). "Simulations of the radiation environment at ISS altitudes". In: *Acta Astronautica* 65.1-2, pp. 279–288. DOI: 10.1016/j.actaastro.2009.01.040.

Gutierrez-D, E. A., Deen, J., and Claeys, C. (2001). *Low temperature electronics : physics, devices, circuits, and applications*. San Diego: Academic Press. ISBN: 9780080510507.

Ha, J. van der, Mimasu, Y., Tsuda, Y., and Mori, O. (2015). "Solar and Thermal Radiation Models and Flight Evaluation for IKAROS Solar Sail". In: *Journal of Spacecraft and Rockets* 52.3, pp. 958–967. DOI: 10.2514/1.a33158.

Hathaway, D. H. (2010). "The Solar Cycle". In: *Living Reviews in Solar Physics* 7.1. DOI: 10.12942/lrsp-2010-1.

Hu, Z., Timmons, T., Stamat, L., and McInnes, C. (2019). "Development of a 10g Femto-satellite with Active Attitude Control". In: *17th Reinventing Space Conference, Belfast, Northern Ireland*.

InvenSense, ed. (2020). *MPU-9250*. URL: https://www.invensense.com/products/motion-tracking/9-axis/mpu-9250/ (visited on 02/02/2020).

Janson, S. (2003). "Micro/Nanotechnology for Micro/Nano/Picosatellites". In: *AIAA Space 2003 Conference & Exposition*. American Institute of Aeronautics and Astronautics. DOI: 10.2514/6.2003-6269.

Janson, S. W. (1995). "Silicon Satellites: Picosats, Nanosats, and Microsats". In: *Proceedings of the International Conference on Integrated Micro/Nanotechnology for Space Applications, The Aerospace Press, Houston, Texas*.

Janson, S. and Barnhart, D. (2013). "The Next Little Thing: Femtosatellites". In: *Proceedings of the AIAA/USU Conference on Small Satellites*. SSC13-VI-3.

Jayasimha, S. and Jyothendar, P. (2013). "Detection of orbital debris using self-interference cancellation residual signal". In: *2013 IEEE International Conference on Space Science and Communication (IconSpace)*. IEEE. DOI: 10.1109/iconspace.2013.6599447.

Johnson, N. L. (2010). "Orbital debris: the growing threat to space operations". In: *33rd Annual Guidance and Control Conference,American Astronomical Society; Washington, DC, United States*.

Joshi, A. (1994). "Startup to Develop Satellite-On-A-Chip". In: *Military & Aerospace Electronics*. Ed. by J. Keller. URL: https://www.discoverysemi.com/news/pressreleases/press01.php (visited on 02/02/2020).

Jove-Casulleras, R., Tristancho, J., and Vera-Flores, C. (2011). "Technical Constraints for a Low-Cost Femto-Satellite Launcher". In: *49th AIAA Aerospace Sciences Meeting including the New Horizons Forum and Aerospace Exposition*. American Institute of Aeronautics and Astronautics. DOI: 10.2514/6.2011-546.

Kang, S.-J. and Oh, H.-U. (2016). "On-Orbit Thermal Design and Validation of 1 U Standardized CubeSat of STEP Cube Lab". In: *International Journal of Aerospace Engineering* 2016, pp. 1–17. DOI: 10.1155/2016/4213189.

Krieger, G. and Moreira, A. (2006). "Spaceborne bi- and multistatic SAR: potential and challenges". In: *IEE Proceedings - Radar, Sonar and Navigation* 153.3, p. 184. DOI: 10.1049/ip-rsn:20045111.

Krieger, G., Hajnsek, I., Papathanassiou, K. P., Younis, M., and Moreira, A. (2010). "Interferometric Synthetic Aperture Radar (SAR) Missions Employing Formation Flying". In: *Proceedings of the IEEE* 98.5, pp. 816–843. DOI: 10.1109/jproc.2009.2038948.

Larson, W. J. and Wertz, J. R. (1999). *Space Mission Analysis and Design, 3rd edition (Space Technology Library, Vol. 8)*. Microcosm. ISBN: 1-881883-10-8.

Leung, R. W., Little, J. W., and Li, D. C. (2007). "Getting Ready for the A380 Aircraft at Hong Kong International Airport". In: *2007 FAA Worldwide Airport Technology Transfer Conference*. Citeseer.

Lücking, C., Colombo, C., and McInnes, C. R. (2012). "Electrochromic Orbit Control for Smart-Dust Devices". In: *Journal of Guidance, Control, and Dynamics* 35.5, pp. 1548–1558. DOI: 10.2514/1.55488.

Macdonald, M. and Badescu, V. (2014). *The International Handbook of Space Technology*. Springer Berlin Heidelberg. DOI: 10.1007/978-3-642-41101-4.

Macdonald, M., McKay, R., Vasile, M., and Frescheville, F. B. D. (2010). "Extension of the Sun-Synchronous Orbit". In: *Journal of Guidance, Control, and Dynamics* 33.6, pp. 1935–1940. DOI: 10.2514/1.49011.

Manchester, Z., Peck, M., and Filo, A. (2013). "KickSat: A Crowd-Funded Mission To Demonstrate the World's Smallest Spacecraft". In: *Proceedings of the AIAA/USU Conference on Small Satellites*. SSC13-IX-5.

Mandeville, A. and Jackson, R. (2009). "Surface mount end-fire antenna package". In: *Electronics Letters* 45.7, p. 340. DOI: 10.1049/el.2009.3016.

Mariappan, A., Kumar, V. S., Anand, V., Weddell, S., and Jeung, I.-S. (2019). "A Conceptual Method to Recycle Space Debris into Fuels and Artificial Soil in the ISS for Numerous Applications". In: *AIAA Propulsion and Energy 2019 Forum*. American Institute of Aeronautics and Astronautics. DOI: 10.2514/6.2019-4157.

Martin, L., Fisher, N. G., Jones, W. H., Furumo, J. G., and Jr., J. R. A. H. (2011). "Ho'oponopono: A Radar Calibration CubeSat". In: *Proceedings of the AIAA/USU Conference on Small Satellites*. SSC11-VI-7.

Martin, M. and Kilberg, S. (2001). "TechSat 21 and Revolutionizing Space Missions using Microsatellites". In: *Proceedings of the AIAA/USU Conference on Small Satellites*. SSC01-1-3.

Martinelli, M. I. and Peña, R. S. S. (2005). "Passive 3 axis attitude control of MSU-1 picosatellite". In: *Acta Astronautica* 56.5, pp. 507–517. DOI: 10.1016/j.actaastro.2004.10.007.

Marzano, F. S., Mori, S., Chini, M., Pulvirenti, L., Pierdicca, N., Montopoli, M., and Weinman, J. A. (2011). "Potential of high-resolution detection and retrieval of precipitation fields from X-band spaceborne synthetic aperture radar over land". In: *Hydrology and Earth System Sciences* 15.3, pp. 859–875. DOI: 10.5194/hess-15-859-2011.

McInnes, C. R. (2004). *Solar Sailing: Technology, Dynamics and Mission Applications (Springer Praxis Books)*. Springer. ISBN: 3540210628.

McLeod, P. (2003). *A Review of Flexible Circuit Technology and Its Applications*. PRIME Faraday Partnership. ISBN: 184402010X.

McTernan, J., Bilen, S., Bell, I., and Gilchrist, B. (2012). "Current Collection to and Plasma Interaction with Femtosatellite- and CubeSat-Scale Electrodynamic Tether Subsystems". In: *AIAA SPACE 2012 Conference & Exposition*. American Institute of Aeronautics and Astronautics. DOI: 10.2514/6.2012-5295.

Melvin, W. L. and Scheer, J. A. (2011). *Principles Of Modern Radar: Radar Applications*. SciTech Publishing Inc. ISBN: 1891121545.

Melvin, W. L. and Scheer, J. A. (2012). *Principles of Modern Radar*. SciTech Publishing Inc. 816 pp. ISBN: 1891121545. URL: https://www.ebook.de/de/product/19571469/principles_of_modern_radar.html.

Meng, H., Wang, X., Chong, J., Wei, X., and Kong, W. (2017). "Doppler Spectrum-Based NRCS Estimation Method for Low-Scattering Areas in Ocean SAR Images". In: *Remote Sensing* 9.3, p. 219. DOI: 10.3390/rs9030219.

Mingotti, G. and McInnes, C. R. (2014). "High Area-to-MassRatio and Small Length-Scale Spacecraft FormationFlying Applications". In: *24th AAS/AIAA Space FlightMechanics Meeting*.

Morrow, W. and Rogers, T. (1964). "The West Ford experiment: An introduction to this issue". In: *Proceedings of the IEEE* 52.5, pp. 461–468. DOI: 10.1109/proc.1964.2991.

Mueller, J., Ziemer, J., Green, A., and Bame, D. (2003). "Performance Characterization of the Vaporizing Liquid Micro-thruster (VLM)". In: *International Electric Propulsion Conference*.

Mullick, S., Srinivasa, Y., Sahu, A. K., and Sata, J. T. (2019). "A Comprehensive Study on Space Debris, Threats Posed by Space Debris, and Removal Techniques". In: *Threats Posed by Space Debris, and Removal Techniques (May 17, 2019)*.

Muntoni, G., Schirru, L., Pisanu, T., Montisci, G., Valente, G., Gaudiomonte, F., Serra, G., Urru, E., Ortu, P., and Fanti, A. (2017). "Space Debris Detection in Low Earth Orbit with the Sardinia Radio Telescope". In: *Electronics* 6.3, p. 59. DOI: 10.3390/electronics6030059.

Niccolai, L., Bassetto, M., Quarta, A., and Mengali, G. (2019). "A review of Smart Dust architecture, dynamics, and mission applications". In: *Progress in Aerospace Sciences*. DOI: 10.1016/j.paerosci.2019.01.003.

Pang, C. K., Kumar, A., Goh, C. H., and Le, C. V. (2015). "Nano-satellite swarm for SAR applications: design and robust scheduling". In: *IEEE Transactions on Aerospace and Electronic Systems* 51.2, pp. 853–865. DOI: 10.1109/taes.2014.140077.

Peczalski, A., Elgersma, M., Quenon, D., and Jacobs, J. (2001). "Micro-wheels for attitude control and energy storage in small satellites". In: *2001 IEEE Aerospace Conference Proceedings (Cat. No.01TH8542)*. IEEE. DOI: 10.1109/aero.2001.931209.

Persico, A. R., Kirkland, P., Clemente, C., Soraghan, J. J., and Vasile, M. (2019). "CubeSat-Based Passive Bistatic Radar for Space Situational Awareness: A Feasibility Study". In: *IEEE Transactions on Aerospace and Electronic Systems* 55.1, pp. 476–485. DOI: 10.1109/taes.2018.2848340.

Post, M., Bauer, R., Li, J., and Lee, R. (2016). "Study for femto satellites using micro Control Moment Gyroscope". In: *2016 IEEE Aerospace Conference*. IEEE. DOI: 10.1109/aero.2016.7500721.

Qian, Y. and Zhu, D. (2019). "Focusing of Ultrahigh Resolution Spaceborne Spotlight SAR on Curved Orbit". In: *Electronics* 8.6, p. 628. DOI: 10.3390/electronics8060628.

Sandau, R. (2010). "Status and trends of small satellite missions for Earth observation". In: *Acta Astronautica* 66.1-2, pp. 1–12. DOI: 10.1016/j.actaastro.2009.06.008.

Schlutz, M. (2009). "Synthetic Aperture Radar Imaging Simulated in MATLAB". PhD thesis. DOI: 10.15368/theses.2009.106.

Selva, D. and Krejci, D. (2012). "A survey and assessment of the capabilities of Cubesats for Earth observation". In: *Acta Astronautica* 74, pp. 50–68. DOI: 10.1016/j.actaastro.2011.12.014.

Shapiro, I., Jones, H., and Perkins, C. (1964). "Orbital properties of the West Ford dipole belt". In: *Proceedings of the IEEE* 52.5, pp. 469–518. DOI: 10.1109/proc.1964.2992.

Smirnov, N. N. (2001). *Space Debris*. Taylor & Francis Ltd. 248 pp. ISBN: 0415279070. URL: https://www.ebook.de/de/product/6903783/space_debris.html.

Snyder, J. S., Brophy, J. R., Hofer, R. R., Goebel, D. M., and Katz, I. (2014). "Experimental Investigation of a Direct-Drive Hall Thruster and Solar Array System". In: *Journal of Spacecraft and Rockets* 51.1, pp. 360–373. DOI: 10.2514/1.a32479.

Sowter, A. (1989). "Drag coefficients with applications to satellite orbits". PhD Thesis. Aston University.

SpaceX (2018). *Capabilities & Services*. URL: http://www.spacex.com/about/capabilities (visited on 02/02/2020).

Stuurman, B. and Kumar, K. (2010). "RyeFemSat: Ryerson University Femtosatellite Design and Testing". In: *SpaceOps 2010 Conference*. American Institute of Aeronautics and Astronautics. DOI: 10.2514/6.2010-2157.

Takeuchi, H., Horiuchi, S., Phillips, C., Edwards, P., McCallum, J., Ellingsen, S., Dickey, J., Ichikawa, R., Takefuji, K., Yamaguchi, T., Kurihara, S., Ichikawa, B., Yoshikawa, M., Tomiki, A., Sawada, H., and Jinsong, P. (2011). "VLBI tracking of the solar sail mission IKAROS". In: *2011 XXXth URSI General Assembly and Scientific Symposium*. IEEE. DOI: 10.1109/ursigass.2011.6051213.

Texas Instruments, ed. (2020a). *ADS5295*. URL: http://www.ti.com/product/ADS5295 (visited on 02/02/2020).

Texas Instruments, ed. (2020b). *CC2520*. URL: http://www.ti.com/product/CC2520 (visited on 02/02/2020).

Texas Instruments, ed. (2020c). *MSP430F2274*. URL: http://www.ti.com/product/MSP430F2274-EP (visited on 02/02/2020).

Tristancho, J. and Gutierrez-Cabello, J. (2011). "A probe of concept for femto-satellites based on commercial-of-the-shelf". In: *2011 IEEE/AIAA 30th Digital Avionics Systems Conference*. IEEE. DOI: 10.1109/dasc.2011.6096137.

Tsuda, Y., Mori, O., Funase, R., Sawada, H., Yamamoto, T., Saiki, T., Endo, T., and Kawaguchi, J. (2011). "Flight status of IKAROS deep space solar sail demonstrator". In: *Acta Astronautica* 69.9-10, pp. 833–840. DOI: 10.1016/j.actaastro.2011.06.005.

Vallado, D. A. (2013). *Fundamentals of Astrodynamics and Applications, 4th ed. (Space Technology Library)*. Microcosm Press. ISBN: 1881883191.

Villela, T., Costa, C. A., Brandão, A. M., Bueno, F. T., and Leonardi, R. (2019). "Towards the Thousandth CubeSat: A Statistical Overview". In: *International Journal of Aerospace Engineering* 2019, pp. 1–13. DOI: 10.1155/2019/5063145.

Wahl, T., Høye, G. K., Lyngvi, A., and Narheim, B. T. (2005). "New possible roles of small satellites in maritime surveillance". In: *Acta Astronautica* 56.1-2, pp. 273–277. DOI: 10.1016/j.actaastro.2004.09.025.

Wang, R. and Deng, Y. (2018). *Bistatic SAR System and Signal Processing Technology*. Springer Singapore. DOI: 10.1007/978-981-10-3078-9.

Weis, L. and Peck, M. (2014). "Active Solar Sail Design for Chip-Scale Spacecraft". In: *Proceedings of the AIAA/USU Conference on Small Satellites*. SSC14-X-6.

Williams, T. and Wang, Z.-S. (2002). "Uses of solar radiation pressure for satellite formation flight". In: *International Journal of Robust and Nonlinear Control* 12.2-3, pp. 163–183. DOI: 10.1002/rnc.681.

Wong, F., Cumming, I., and Neo, Y. L. (2008). "Focusing Bistatic SAR Data Using the Nonlinear Chirp Scaling Algorithm". In: *IEEE Transactions on Geoscience and Remote Sensing* 46.9, pp. 2493–2505. DOI: 10.1109/tgrs.2008.917599.

Yamaguchi, T., Mimasu, Y., Tsuda, Y., and Yoshikawa, M. (2014). "Hybrid Estimation of Solar Radiation Pressure for a Spinning Solar Sail Spacecraft". In: *Journal of Spacecraft and Rockets* 51.1, pp. 381–384. DOI: 10.2514/1.a32387.

Yegulalp, A. F. (1999). "Fast backprojection algorithm for synthetic aperture radar". In: *Proceedings of the IEEE Radar Conference. Radar into the Next Millennium (Cat. No.99CH36249)*. IEEE. DOI: 10.1109/nrc.1999.767270.